

**COUPLED SPACE-ANGLE ADAPTIVITY AND GOAL-ORIENTED
ERROR CONTROL FOR RADIATION TRANSPORT
CALCULATIONS**

A Thesis
Presented to
The Academic Faculty

by

HyeongKae Park

In Partial Fulfillment
of the Requirements for the Degree
Doctor of Philosophy in
Nuclear and Radiological Engineering

Georgia Institute of Technology
December 2006

**COUPLED SPACE-ANGLE ADAPTIVITY AND GOAL-ORIENTED
ERROR CONTROL FOR RADIATION TRANSPORT
CALCULATIONS**

Approved by:

Dr. Cassiano R. E. de Oliveira, Advisor
Nuclear and Radiological Engineering
Georgia Institute of Technology

Dr. Thomas D. Morley
School of Mathematics
Georgia Institute of Technology

Dr. Farzad Rahnema
Nuclear and Radiological Engineering
Georgia Institute of Technology

Dr. Barry D. Ganapol
Department of Aerospace and Mechanical
Engineering
University of Arizona

Dr. Weston M. Stacey
Nuclear and Radiological Engineering
Georgia Institute of Technology

Date Approved: November 6, 2006

ACKNOWLEDGEMENTS

I would like to thank my advisor, Dr. Cassiano de Oliveira, for his patience and invaluable help during my years at Georgia Institute of Technology. His guidance and broad perspective has always guided me to a right path.

My great appreciation goes to Dr. Farzad Rahnema, Dr. Weston Stacey, Dr. Thomas Morey and Dr. Barry Ganapol for their willingness to serve on my committee. Special appreciation goes to Dr. Ganapol for providing me his semi-analytical method which was used to support my thesis.

I would also like to thank Dr. Richard Martineau for his enthusiasm and insightfulness that gave me motivation to finish this work.

My sincere thankfulness goes to my parents, Seiji and Tomie for their support. Their trust and patience kept me in this academic path to accomplish this task.

I would like to acknowledge my colleagues and staff members at the Neely Nuclear Research Center.

Finally, I cannot thank enough to my wife, Magnolia, her invaluable support. Without her help, I could not have finished.

TABLE OF CONTENTS

	Page
ACKNOWLEDGEMENTS	iii
LIST OF TABLES	viii
LIST OF FIGURES	x
SUMMARY	xiii
<u>CHAPTER</u>	
1. INTRODUCTION	1
1.1 Background	1
1.2 Computational Methodologies in the Radiation Transport Modeling	1
1.3 Trend and Challenges in Radiation Transport Simulations	2
1.4 Literature Review on Adaptivity	4
1.4.1 <i>A Posteriori</i> Error Analysis and Adaptive Mesh Refinement	5
1.4.2 Goal-Oriented Adaptivity	6
1.4.3 Adaptivity in Radiation Transport	7
1.5 Research Objectives	9
1.6 Outline	10
2. FIRST- AND SECOND-ORDER FORM OF THE RADIATION TRANSPORT EQUATION	12
2.1 The Radiation Transport Equation	12
2.1.1 Vacuum Boundary Condition	13
2.1.2 Reflective Boundary Condition	14
2.1.3 Continuity Conditions at Material Interfaces	14
2.2 Multigroup Approximation	15
2.3 Second-Order, Even-Parity Form of the Transport Equation	17

2.3.1 Vacuum Boundary Condition	19
2.3.2 Reflective Boundary Condition	20
2.3.3 Material Interface Conditions	20
2.4 Summary	21
3. THE FINITE ELEMENT SPHERICAL HARMONICS METHOD	22
3.1 Even-Parity Variational Principle	22
3.2 The Finite Element-Spherical Harmonics Discretization	25
3.2.1 The Spherical Harmonics Angular Approximation	25
3.2.2 The Finite Element Approximation	27
3.2.3 Ritz-Galerkin Procedure	28
3.3 General Solution Strategy Applied to the FE-P _N Method	30
3.4 Summary	32
4. <i>A POSTERIORI</i> ERROR ANALYSIS AND ADAPTIVITY FRAMEWORK FOR RADIATION TRANSPORT PROBLEMS	33
4.1 <i>A Priori</i> Error Estimates	33
4.2 Residual-Based <i>a Posteriori</i> Error Analysis	35
4.2.1 A L ₂ Norm <i>A Posteriori</i> Error Estimator	35
4.2.2 An Energy Norm <i>A Posteriori</i> Error Estimator	40
4.3 Separation of the Error Components	43
4.4 Treatment of the Angular Variables	44
4.4.1 Implicit Error Estimator for the Angular Variables	44
4.4.1.1 Reliability of the Implicit Estimator	46
4.4.2 Surface Angular Integrals	48
4.5 Spatial Mesh Refinement Strategy in Two-Dimensional <i>x-y</i> Geometry	51
4.6 Coupled Space-Angle Adaptive Strategy	54
4.6.1 Consideration to the Eigenvalue, Fission Source Problem	55

4.6.2	Consideration to the Multigroup Problem	56
4.7	Summary	56
5.	GOAL-ORIENTED ADAPTIVITY AND ERROR CONTROL	58
5.1	Different Forms of the Extremum Variational Principles	58
5.1.1	The Canonical Form of the Even-Parity Variational Principle	59
5.1.2	The Canonical Variational Principle with Lagrange Multiplier	60
5.1.3	Involutory Form of the Variational Principle	60
5.1.4	Extremum Value of the Variational Principle	61
5.2	Bounds on Functionals	62
5.3	Goal-Oriented Error Bounds	64
5.4	<i>A Posteriori</i> Error Bounds by the Extremum Variational Principles and Goal-Oriented Error Bounds	66
5.5	Summary	67
6.	NUMERICAL RESULTS	69
6.1	The Method of Manufactured Solution	69
6.2	Verification through the Method of Manufactured Solutions	70
6.2.1	Test Case 1—Measure of Zero Error	71
6.2.2	Test Case 2—Measure of Angular Truncation Error	72
6.2.3	Test Case 3—Measure of Spatial Discretization Error	73
6.2.4	Test Case 4—Goal-Oriented Adaptivity	79
6.3	One-dimensional Examples	84
6.3.1	Modified Reed’s Problem	85
6.3.2	Fission in a Slab Problem	88
6.4	Two-dimensional Examples	90
6.4.1	The Azmy Benchmark Problem	90
6.4.1.1	Flux Comparison at $x = 5.84375\text{cm}$	92

6.4.1.2 Flux Comparison at $x = 7.84375\text{cm}$	95
6.4.1.3 Flux Comparison at $x = 9.84375\text{ cm}$	97
6.4.2 Simple 2-Group Eigenvalue Problem	100
6.4.3 Gamma Transport in the Simple Fuel Cask Problem	105
7. CONCLUSIONS	112
7.1. Recommendations for Future Work	112
APPENDIX A: Cross Sections Used in Gamma Transport Problem	115
VITA	132

LIST OF TABLES

	Page
Table 3.1: Spatial and angular integral tables used in the FE-P _N method	29
Table 6.1: Result for Test Case 2	73
Table 6.2: Effective index of the spatial mesh refinement	76
Table 6.3: Effective index of the angular truncation error for Test Case 3	79
Table 6.4: Error bounds for Test Case 4 without K^+ principle	83
Table 6.5: Error bounds for Test Case 4 with K^+ principle	83
Table 6.6: Average error computed by the bounds without the K^+ principle	84
Table 6.7: Average error computed by the bounds with the K^+ principle	84
Table 6.8: Specification of modified Reed's problem	86
Table 6.9: Comparison between adaptive and uniform refinement strategies for the modified Reed problem	87
Table 6.10: Problem parameters for fission in a slab problem	89
Table 6.11: Summary of fission in a slab problem (True Leakage = 0.34509)	89
Table 6.12: Comparison of total degrees of freedom in uniform and adaptive calculations 1	94
Table 6.13: Comparison of total degrees of freedom in uniform and adaptive calculations 2	96
Table 6.14: Comparison of total degrees of freedom in uniform and adaptive calculations 3	99
Table 6.15: Material cross sections of the two group eigenvalue problem (in cm ⁻¹)	101
Table 6.16: Comparison of the peak flux values for group 17	108
Table 6.17: Summary of the gamma transport problem	111
Table A.1: 20 group cross sections of the fuel material	115
Table A.2: 20 group cross sections of the water material	119

LIST OF FIGURES

	Page
Figure 2.1: Schematics of problem definition	15
Figure 3.1: Illustration of the extremum variational principle [37]	24
Figure 3.2: Typical two-dimensional triangular element and its linear basis functions	28
Figure 3.3: The preconditioned conjugate gradient algorithm	30
Figure 4.1: Illustration of relationship between numerical error and mesh size	34
Figure 4.2: Illustration of angular coordinate relative to the element edge in the case of normal vector being parallel to the y -axis	49
Figure 4.3: Illustration of the half-range surface integral in new coordinate system (x',y',z') . New coordinate system is rotated counter clockwise by angle α about z -axis	50
Figure 4.4: Element refinement strategy	52
Figure 4.5: Two different subdivisions for element with two hanging nodes	53
Figure 4.6: Subdivision of element for one hanging node	54
Figure 4.7: A coupled space-angle adaptive strategy	55
Figure 5.1: Illustration of the original and involutory form of the variational principles	61
Figure 6.1: Mesh and flux profile for Test Case 1	71
Figure 6.2: Flux and estimated angular truncation error in Test Case 2	73
Figure 6.3: Flux profile and the estimated (left) and true (right) errors	74
Figure 6.4: Profile of the angular truncation error for Test Case 3 (right=true error, left=estimated error)	78
Figure 6.5: Distribution of the angular order used in Test Case 3 (red= P_5 , green= P_3 and blue= P_1)	78
Figure 6.6: Problem description of Test Case 4	79
Figure 6.7: Forward and adjoint scalar flux for Test Case 4	81

Figure 6.8: Initial and final mesh of Test Case 4	81
Figure 6.9: Scalar flux solution (left y-axis) and angular expansion used (right y-axis) for the Reed's problem	86
Figure 6.10: Total number of DoFs versus maximum error of P ₅ -P ₉ approximations	87
Figure 6.11: Total number of DoFs versus maximum error of P ₁₁ -P ₁₅ approximations	88
Figure 6.12: Problem schematic of Azmy benchmark problem	90
Figure 6.13: Flux profile for Azmy benchmark problem	91
Figure 6.14: Illustration of the adaptively refined mesh based on the global L ₂ norm	91
Figure 6.15: Illustrative final mesh produced by goal-oriented adaptivity (3362 elements, 1705 nodes)	93
Figure 6.16: Scalar flux plot along $x=5.84375$ cm	93
Figure 6.17: Distribution of the angular moments used for the goal-oriented adaptivity applied at $x = 5.84375$ cm	95
Figure 6.18: Scalar flux profiles along $x=7.84375$ cm	96
Figure 6.19: Final Adaptive mesh and the distribution of the angular orders used in the adaptive mesh refinement for the comparison at $x = 7.84375$ cm	97
Figure 6.20: Scalar flux profile along $x = 9.84375$ cm	98
Figure 6.21: Final uniform and adaptive mesh	99
Figure 6.22: Adaptive mesh and distribution of angular moments for the comparison at $x = 9.84375$ cm	100
Figure 6.23: Schematics of the two-group eigenvalue problem	101
Figure 6.24: Flux profile of the two-group eigenvalue problem	102
Figure 6.25: Initial and final mesh for the two-group eigenvalue problem	103
Figure 6.26: The % k_{eff} difference versus number of nodes	104
Figure 6.27: Geometry of the gamma transport problem	105
Figure 6.28: Flux profile for the gamma transport problem	106
Figure 6.29: Group 1 scalar flux profile of the gamma transport problem at $y = 5.0$ cm	107

Figure 6.30: Group 17 scalar flux profile of the gamma transport problem at $y = 5.0\text{cm}$	108
Figure 6.31: Group 20 scalar flux profile of the gamma transport problem at $y = 5.0\text{cm}$	109
Figure 6.32: Angular expansion orders distribution for the gamma transport problem for group 1, 17 and 20	110

SUMMARY

This research is concerned with the self-adaptive numerical solution of the neutral particle radiation transport problem. Radiation transport is an extremely challenging computational problem since the governing equation is seven-dimensional (3 in space, 2 in direction, 1 in energy, and 1 in time) with a high degree of coupling between these variables. If not careful, this relatively large number of independent variables when discretized can potentially lead to sets of linear equations of intractable size. Though parallel computing has allowed the solution of very large problems, available computational resources will always be finite due to the fact that ever more sophisticated multiphysics models are being demanded by industry. There is thus the pressing requirement to optimize the discretizations so as to minimize the effort and maximize the accuracy.

One way to achieve this goal is through adaptive phase-space refinement. Unfortunately, the quality of discretization (and its solution) is, in general, not known *a priori*; accurate error estimates can only be attained via the *a posteriori* error analysis. In particular, in the context of the finite element method, the *a posteriori* error analysis provides a rigorous error bound. The main difficulty in applying a well-established *a posteriori* error analysis and subsequent adaptive refinement in the context of radiation transport is the strong coupling between spatial and angular variables. This research attempts to address this issue within the context of the second-order, even-parity form of the transport equation discretized with the finite-element spherical harmonics method.

The objective of this thesis is to develop *a posteriori* error analysis in a coupled space-angle framework and an efficient adaptive algorithm. Moreover, the mesh refinement strategy which is tuned for minimizing the error in the target engineering output has been developed by employing the dual argument of the problem. This numerical framework has been implemented in the general-purpose neutral particle code EVENT for assessment.

CHAPTER 1

INTRODUCTION

1.1 Background

Particle transport problems arise in many different areas of engineering physics. For example, nuclear reactor physics, radiation therapy applications, and astrophysical phenomena can all be modeled by radiation transport theory. Computational radiation transport has steadily gained acceptance in the last decade as a viable modeling tool due to the rapid advancements in computer software and hardware technologies. However, ever-increasing problem complexity and size easily exceed the capability of the existing hardware. Thus, efficient use of the computational resources is the key to success for radiation modeling and this has been the major thrust of the modern numerical transport methods research.

1.2 Computational Methodologies in the Radiation Transport Modeling

There are two main types of simulation approaches in radiation transport modeling: stochastic (Monte Carlo) and deterministic [1]. The Monte Carlo method simulates directly the physics of the neutral particles. Despite its severe demands on computational effort, in particular with regards to CPU usage, the Monte Carlo method is often considered as the analysis tool of choice, due to its geometrical flexibility and availability of a measure of statistical error. This feature of the Monte Carlo method is particularly valuable when the main quantity of interest in a problem is a specified engineering output (functional), especially at a localized neighborhood, as may be the case in determining the magnitude of the radiation dose to a part of a problem domain. However, recent new advanced reactor designs require detailed coupled multi-physics analysis everywhere within the system and because of this, the Monte Carlo method may not be the best choice.

Deterministic radiation transport has gained popularity in recent years as a consequence of continuous advancements in computer technology and numerical algorithmic development. Nonetheless, the success of deterministic methods is largely dictated by its accuracy and numerical efficiency. The brute-force, trial-and-error analysis is a foolproof procedure to ensure accuracy although at a cost of dedicated human intervention. This iterative procedure of intervention is clearly a wasteful and inefficient method for solving radiation transport problems. Thus, a numerical algorithm, which ensures the quality of numerical solution with minimal user intervention, is necessary requirement for deterministic methods to become practical design tools.

1.3 Trend and Challenges in Radiation Transport Simulations

Clear understanding of the reactor behavior is crucial in developing the next generation reactors. Physical behavior during operational and transient conditions is dictated by strong non-linearly coupled multi-physics phenomena which include radiation transport, fluid dynamics, heat transfer, and structural mechanics. The required spatial and temporal resolution to predict the proper feedback mechanisms can differ significantly among these physical phenomena. Because the accurate prediction of proper feedback is the key to the successful design, the current research trend is to develop high-fidelity numerical methodologies based on the fundamental principles.

Radiation transport already plays a key role in the multiphysics simulation of nuclear reactor systems. However, current reactor analysis calculations apply a series of physical and geometrical approximations in order to ease the computational demand to a manageable size. The uncertainty that originates from these simplifications has been somewhat reduced by extensive operational experiences; however, it is unlikely that the experience acquired from the current LWR technology is applicable to the next generation reactors to the full extent since the next generation reactors are likely to have highly heterogeneous cores, which, if analyzed via the conventional two step (diffusion +

transport) approach will lead to a deterioration in accuracy. Therefore, the current trend in computational radiation transport is to develop high-fidelity computational tools which are solely based on the transport theory.

Another active area of application for radiation transport is in the field of medical physics. Therapeutic use of radiation doses to the patients requires the optimization of dose delivery to tumors while minimizing damage to the healthy neighboring organs. A detailed modeling of the radiation field distribution and interaction with the human body is required to optimize the therapeutic plan of the radiation treatment. A unique feature of medical physics modeling is the mono-directional, narrow beam sources which are often applied to the human body. Consequently, large gradients of the radiation intensity in the transverse direction and highly forward peaked angular profiles are observed. The boundary between target and “radiation-sensitive” organs often lies on these large-gradient regions. Therefore, inaccurate resolution of the radiation profile will result in very conservative and inefficient treatment plans. Due to the large pool of cancer patients that are treated on an everyday basis, and the large number of the beam configurations used for each patient, efficient and accurate dose estimates are crucial components in the success of the radiation treatment planning.

The difficulty in developing high-fidelity radiation transport solutions is caused by the large number of independent variables characterizing the radiation transport equation. Discretization of the six independent variables (three-dimension in space, two-dimension in directional dependence, and one-dimension in the energy) for practical problems inevitably leads to coupled systems of linear equations of intractable size. Parallel computation can alleviate this problem to some extent; however the optimum use of computational resources by means of adaptive refinement is the only way forward to accomplish this difficult task. Moreover, an adaptive algorithm together with *a posteriori* error analysis provides the framework for estimating the discretization error and thus enabling the elimination of excessive iterative cycles.

Adaptive mesh refinement together with *a posteriori* error analysis has gained a great deal of popularity in other fields of engineering over the last 20 years. Yet in radiation transport, the concept of an adaptive method has not become prevalent, mainly due to the difficulty in applying the well-established *a posteriori* error analysis to the strongly coupled space-angle phase-space. However, the development of mathematical and physical adaptivity frameworks and error control algorithms in the context of deterministic radiation transport has recently become a priority so that the developed algorithms can contribute towards realistic nuclear engineering design analyses.

An alternate approach to making error estimation more relevant to engineering applications is to seek the error in a functional (goal) representing a desired output. For example, the multiplication factor (k_{eff}) might be a key quantity for criticality calculations, or the dose rate to a specified organ might be the one for medical physics applications. A key step of a goal-oriented adaptivity is to solve the dual (adjoint) problem to map the importance and estimate the error in the functional output. This method, although at a cost of doubling the computational effort, can provide the (near) optimum discretizations which are particularly tuned to minimize the desired engineering output, and furthermore a reliable error indicator.

1.4 Literature Review on Adaptivity

All numerical methods are susceptible to numerical (discretization) errors. Practitioners have been aware of this fact since the early days of numerical simulations; therefore, experimental judgments and the trial-and-error approach have often been employed to ensure the quality of a numerical solution. In this section, a literature review is conducted which is split into three subsections. Firstly, we review the development of *a posteriori* error analysis based on the global norm. Next, literature on adaptive mesh refinement that is specially tuned to minimize a certain functional is reviewed. We conclude with a review of adaptivity research in the context of radiation transport.

1.4.1 *A Posteriori* Error Analysis and Adaptive Mesh Refinement

A rigorous *a posteriori* error analysis was first introduced in the pioneering work of Babuska and Rheinbolt [2]. The discretization error for elliptic problems was estimated by solving local Dirichlet problems in the patch of elements surrounding each vertex in the finite element mesh. Since then, especially from late 1970's to early 1980's, a large number of papers regarding *a posteriori* error analysis have been published (e.g. [3, 4, 5]).

Demkowicz et al. [6] was the first to introduce *a posteriori* error estimates derived from the local finite element residuals and discontinuity in the normal derivative along the element interfaces. The developed error estimator was exploited to adaptively refine the polynomial order of the hierarchical finite element basis functions (*p*-adaptivity). At the same time, Bank and Weiser [7, 8] derived *a posteriori* error bounds by solving the local Neumann problem in each finite element. This local residual-based error estimation technique has become popular because of its computational efficiency compared to solving the local Dirichlet problems.

Another method of *a posteriori* error estimation is to recover the gradient of the solution. The recovery-based error estimator does not employ any information about the original problem, but only considers the difference in high- and lower-order solutions and/or gradients. This is both an advantage and disadvantage of recovery-based error estimators. Zienkiewicz and Zhu [9, 10] established the “super-convergence patch recovery technique (*ZZ*-estimator)”. Their strategy was to compare the higher order interpolated solution computed by numerical quadrature to the lower order (original) solutions in the local finite elements. Because of the simplicity of the technique and its robustness, the *ZZ*-estimator quickly gained popularity.

A considerable body of literature is available on the subject of *a posteriori* error analysis and adaptive mesh refinement. Ainsworth and Oden [11] published an extensive survey of *a posteriori* error analysis with a large number of references.

1.4.2 Goal-Oriented Adaptivity

One of the main challenges of adaptivity is the development of reliable error indicators. In the previous section, *a posteriori* error analysis, which focused on the global error norm, was discussed; in the case of elliptic problems discretized by finite elements, this provides rigorous error bounds in both global energy and L_2 norm. However, for many realistic engineering applications, the quantity of interest is an integral quantity representing an engineering output. Thus, the error measured in the energy norm provides little relevant information about accuracy. Therefore, it is natural to seek the specific error measure in predicting the accuracy of some desired engineering outputs [12, 13, 14, 15].

An adjoint error correction method [16, 17] has been proposed, which yields super convergence in the target functional by utilizing the finite element residuals computed by higher-order interpolation. In their approach, accuracy of the method is dictated by the efficiency of the interpolation scheme. Despite the great success of the adjoint error correction scheme for simple problems, its use is discouraged due to the computational effort sometimes becoming prohibitively large for multi-dimensional problems.

Goal-oriented adaptivity generally employs the dual argument of the problem. The computational effort thus increases by a factor of two. However, the primary benefit of invoking the dual problem, in the context of error estimation, is that the error in a chosen functional can be directly related to local residual errors of the primal solution through the adjoint variables. More precisely, the error can be expressed as an inner product of the local residual errors and the adjoint variables. This property elucidates the potential for devising optimal grid adaptive strategies designed to produce specially-tuned grids for maximizing the accuracy of a particular functional.

1.4.3 Adaptivity in Radiation Transport

Establishing a bound for the solution has been of interest to numerical practitioners for a long time. In the field of radiation transport, the variational method has long been studied to produce the higher-order estimates for the solution [18]. Since the appearance of the Vladimirov's even-parity variational principle [19], a large research effort has been spent to obtain a functional bound via the transformation of the variational principles [20]. The upper and lower bounds of region-wise absorption rates for transport problem was established by Davis [21], where the even- and odd parity P_N approximation was used to find the error bounds. Buslik investigated the same problem with a slightly different approach [22], which was to employ the adjoint equation and variational principle to establish the solution bounds. Later Ackroyd and Splawski [23] derived the bounds for any finite element solution for neutron transport. Their method seeks the upper and lower bounds of local characteristics (functionals) by using bi-linear functional which utilizes both the forward and adjoint trial functions, and the method does not rely on either the variational method or spherical harmonics angular expansions. However, no activity has taken place to combine the bounds of solution with adaptive mesh refinement.

As mentioned earlier, the adaptivity trend in the field of radiation transport has not become as widespread as in other areas of engineering. Nevertheless, several publications are available in this subject. One popular approach is to utilize *a posteriori* error analysis in the context of neutron diffusion problems [24, 25, 26, 27]. Zhang and Lewis have applied the hierarchical p -refinement strategy to the variational nodal method. In their approach, the interface scalar flux error was estimated by the higher order interpolated solution, which was computed by the ZZ-estimator, with the current lower order approximation. Later, Zhang and Lewis [24] generalized the concept and applied it to the variational nodal P_N method. Ragusa [26] developed the three dimensional, non-conforming finite elements code with an h -adaptive mesh refinement.

Recent work by Wang and Ragusa [27] has demonstrated the use of the *hp*-adaptive refinement strategy for the one-dimensional, one-group diffusion problem.

Another approach was to employ the spatial adaptivity to the context of the discrete ordinates (S_N) methods. Fuhrer and Rannacher [28] analyzed *a posteriori* error estimation for radiative transfer. The Fredholm integral form of transport equation with the finite element discretization was used. Rigorous *a priori* and *a posteriori* error estimates for the global scalar flux error and local angular flux error based on the residual were derived. Warsa and Prinja [29] investigated the use of the *p*-adaptivity in the first-order form of transport equation, which was discretized by the linear and bi-linear discontinuous S_N finite element method. In their work, the difference in outgoing flux of the solution and higher-order interpolated solution was used to judge the quality of polynomial orders. Automatic mesh refinement (AMR) has been used in the context of S_N methods with some success [30]. The mean-free path rule was used as an automatic guidance of refinement criterion. Aussourd has developed the tree-based AMR applied to the finite volume discretization (diamond differencing). All of above methods use a fixed angular discretization and concentrated on the spatial adaptivity.

In case of the angular variable refinement, there are only a few publications available. The method of composite solution was employed to vary the orders of the spherical harmonic expansions from region to region [31, 32]. Transition from low- to high-order expansions is overcome by using the discontinuous finite element formulation with penalty functions. However, the region-dependent angular expansion orders were chosen by intuition, and not by physical principles. In recent work by Stone and Adams [33], a novel approach which employs the local angular quadrature refinement for the S_N method was developed. This new approach splits the spatial domain into “quadrature regions”, where each region uses different angular quadrature sets. The convergence in the angular flux is checked by comparing the flux evaluated at a set of ‘test-directions’ against the angular flux obtained by interpolation from neighboring directions. The

numerical results have demonstrated the elimination of ray-effects and angular discretization error. Park and de Oliveira [34] presented the adaptive angular refinement strategy for the finite element spherical harmonics (FE- P_N) method. In this work, an angular truncation error was estimated by inverting the point-wise block P_N matrices.

It is well known that both the spatial and angular resolution are strongly coupled to the accuracy of the numerical radiation transport problem e.g. for a given angular resolution therefore becomes a point where increased spatial resolution has little impact on solution accuracy. Thus, it is crucial that a self-adaptive methodology also adapt in the direction of radiation travel. It is only when this happens that the true potential of self-adaptive techniques in radiation transport can be realized. Yet, there is no existing literature that presents the methodology for the space-angle adaptivity; therefore developing an integrated space-angle adaptivity strategy lies at the core of this research.

1.5 Research Objectives

The objective of this work is to perform a comprehensive study of coupled space-angle adaptive mesh refinement and error control strategies in the context of deterministic radiation transport. The first goal is to derive *a posteriori* error estimates for the (even-parity) angular flux, the solution of second-order, even-parity form of transport equation, in the form of the global L_2 and/or energy norm. The main task here is to extend the well-established *a posteriori* error analysis to space-angle variables and to develop an adaptive refinement algorithm for both spatial and angular discretizations.

The second goal is to extend the adaptive methodology to a goal-oriented adaptivity, which measures and controls the error of a desired output using the dual (adjoint) solutions. The numerical schemes developed will be implemented in the general multigroup radiation transport code EVENT [35] in order to assess the numerical efficiency and accuracy.

1.6 Outline

We have briefly discussed the importance and difficulty in developing accurate and reliable numerical schemes for the radiation transport calculations. The adaptive finite element framework offers one of the most promising routes for achieving this goal. This thesis will thus focus on the development of a coupled space-angle adaptive algorithm for radiation transport calculations based on this framework.

In Chapter 2 we introduce the second-order, even-parity form of transport equations. The first-order linear Boltzmann transport equation is first introduced. The second-order, even-parity form of the transport equation is derived via the canonical transformation. The multigroup approximation in energy is briefly discussed.

The finite element-spherical harmonics discretization of the even-parity transport equation is discussed in Chapter 3. The discretization results in nested block-structured sparse linear systems. We discuss the global structure of the whole discretized system and solution and preconditioning techniques for this particular system of algebraic equations.

A posteriori error analysis and development of the error estimator based on the global norms is presented in Chapter 4. We closely follow the residual-based *a posteriori* error analysis introduced by Babuska and Rheinbolt [2] and extend the concept to the coupled space-angle formulation. A strategy to separate the error components between spatial and angular variables, and use of the explicit, and implicit error estimators will be given. Then, the general adaptive mesh refinement algorithm is formulated.

In Chapter 5, we extend the developed adaptive strategy to the goal-oriented adaptivity. The variants of the extremum variational principle are introduced in order to obtain the functional bound. Incorporation of *a posteriori* error analysis and the variational estimates provides the error estimates of the arbitrary functional output.

The validity of the developed algorithms is assessed through the solution of representative numerical examples. The developed algorithms have been implemented in

one- and two-dimensional finite element codes. To verify the behavior of adaptive algorithms, the Method of Manufactured Solution (MMS) is introduced. Selected one-dimensional calculation results are compared to the (semi-) analytical result so that the effectiveness of the developed error indicator can be validated. The adaptive algorithm is also implemented in the general purpose radiation transport code EVENT [35] to test the validity of the realistic two-dimensional problems.

CHAPTER 2

FIRST- AND SECOND-ORDER FORM OF THE RADIATION TRANSPORT EQUATION

In this chapter, the governing integro-differential equation for the radiation transport problem is introduced. The radiation transport equation characterizes a simple balance of the particles within a differential volume of phase space. Simplification of transport problems by means of a steady state, multigroup approximations is introduced in the section 2. In section 3, the alternative (second-order, even-parity) form of the transport equation is derived via the canonical transformation. The numerical and mathematical analyses in this thesis rely deeply on the elliptic property of the even-parity equation.

The second-order form of the transport equation has nice mathematical and numerical properties. First of all, the even-parity transport equation separates the angular flux into even- and odd parity components. Together with the orthogonal relations of the spherical harmonics, the resulting discretized form of the transport equation only requires half of the angular unknowns. Moreover, the collision operators, expanded in Legendre polynomials, allow an implicit treatment of the scattering kernel; i.e. no scattering source iteration is needed. Finally, the finite element discretization of the even-parity equation through the Ritz-Galerkin procedure results in block-symmetric positive definite matrix equations, which are amenable to solution by the well-known preconditioned conjugate-gradient solution algorithm [36].

2.1 The Radiation Transport Equation

We are interested here to identify the mean or expected behavior of a particle migrating through participating media using radiation transport theory. The state of particle is characterized by its position (\mathbf{r}), direction of travel ($\mathbf{\Omega}$) and energy (E) at given

time (t). This six-dimensional space is commonly referred to as the “phase-space.” The dynamics of the neutral particle distribution can be represented by the linear Boltzmann transport equation [1] which describes the rate of change in the particle number distribution, $n(\mathbf{r}, \boldsymbol{\Omega}, E, t)$ in the differential phase-space $dVd\boldsymbol{\Omega}dE$ about a phase-point $(\mathbf{r}, \boldsymbol{\Omega}, E)$:

$$\begin{aligned} \frac{\partial n(\mathbf{r}, \boldsymbol{\Omega}, E, t)}{\partial t} = & -\boldsymbol{\Omega} \cdot \nabla \psi(\mathbf{r}, \boldsymbol{\Omega}, E, t) - \sigma_t \psi(\mathbf{r}, \boldsymbol{\Omega}, E, t) \\ & + \int_0^\infty dE' \int_{4\pi} d\boldsymbol{\Omega}' \sigma_s(\mathbf{r}, \boldsymbol{\Omega}' \rightarrow \boldsymbol{\Omega}, E' \rightarrow E) \psi(\mathbf{r}, \boldsymbol{\Omega}', E', t) + S(\mathbf{r}, \boldsymbol{\Omega}, E, t) \end{aligned} \quad (2.1)$$

where, $\psi(\mathbf{r}, \boldsymbol{\Omega}, E, t) = vn(\mathbf{r}, \boldsymbol{\Omega}, E, t)$ is the angular flux,

v is the velocity of the particle,

$\sigma_t(\mathbf{r}, E)$ is the total cross section,

$\sigma_s(\mathbf{r}, \boldsymbol{\Omega}' \rightarrow \boldsymbol{\Omega}, E' \rightarrow E)$ is the scattering cross-sections, and

$S(\mathbf{r}, \boldsymbol{\Omega}, E, t)$ is the extraneous source term.

The first two terms of the RHS of Eq. (2.1) represent the losses mechanisms due to leakage and interaction with the host medium, and last two terms are the source terms due to the inward scattering rate to the phase space element $d\boldsymbol{\Omega}dE$ from the all elements $d\boldsymbol{\Omega}'dE'$ and the extraneous source. We denote the non-reentrant convex region, where the transport equation is solved, as V and its surface as Γ .

Proper initial and boundary conditions must be prescribed for the problem to be well-posed. The angular flux at time $t=0$ (i.e. $\psi(\mathbf{r}, \boldsymbol{\Omega}, E, 0)$) must be defined everywhere in V . An inward flux on Γ also needs to be defined. In the next four subsections, we describe the two boundary conditions and material interface condition that are used.

2.1.1 Vacuum Boundary Condition

The most commonly applied boundary condition in the transport problem is the vacuum boundary condition. We denote the boundary corresponding to the vacuum

boundary as Γ_b . The vacuum boundary condition is prescribed at locations where the system interfaces with a non-participating media represented by following:

$$\psi(\mathbf{r}_{\Gamma_b}, \boldsymbol{\Omega}, E, t) = 0 \text{ for } \mathbf{n} \cdot \boldsymbol{\Omega} < 0 \quad (2.2a)$$

where, \mathbf{n} denotes the outward normal vector on Γ .

This boundary condition can be generalized to an incoming flux

$$\psi(\mathbf{r}_{\Gamma_b}, \boldsymbol{\Omega}, E, t) = \psi_0(\mathbf{r}_{\Gamma_b}, \boldsymbol{\Omega}, E, t) \text{ for } \mathbf{n} \cdot \boldsymbol{\Omega} < 0 \quad (2.2b)$$

where, Γ_b denotes the surface with the vacuum boundary condition.

2.1.2 Reflective Boundary Condition

The second common boundary condition is the (specular) reflective boundary condition which is applied to surface Γ_r . The reflective boundary condition is often employed when the geometry of the problem has a plane of symmetry. It enables a reduction of problem size. The perfect reflector boundary condition can be imposed by the following equation:

$$\psi(\mathbf{r}_{\Gamma_r}, \boldsymbol{\Omega}, E, t) = \psi(\mathbf{r}_{\Gamma_r}, \boldsymbol{\Omega}^*, E, t), \text{ where } \boldsymbol{\Omega}^* = \boldsymbol{\Omega} - 2(\mathbf{n} \cdot \boldsymbol{\Omega})\mathbf{n} \quad (2.3)$$

2.1.3 Continuity Conditions at Material Interfaces

Material discontinuities often arise in the transport problems. In the transport equation, a continuity condition holds along the direction of the particle travel. At a material interface γ with no sources, the angular flux and current continuity conditions are satisfied by:

(i) angular flux continuity:

$$\lim_{\varepsilon \rightarrow 0} [\psi(\mathbf{r}_\gamma + \varepsilon \boldsymbol{\Omega}, \boldsymbol{\Omega}, E, t) - \psi(\mathbf{r}_\gamma - \varepsilon \boldsymbol{\Omega}, \boldsymbol{\Omega}, E, t)] = 0 \quad (2.4)$$

which implies

(ii) current continuity:

$$\lim_{\varepsilon \rightarrow 0} (\boldsymbol{\Omega} \cdot \mathbf{n}_\gamma) [\psi(\mathbf{r}_\gamma + \varepsilon \boldsymbol{\Omega}, \boldsymbol{\Omega}, E, t) - \psi(\mathbf{r}_\gamma - \varepsilon \boldsymbol{\Omega}, \boldsymbol{\Omega}, E, t)] = 0 \text{ for } \boldsymbol{\Omega} \cdot \mathbf{n}_\gamma \neq 0 \quad (2.5)$$

where, \mathbf{n}_γ denotes the normal vector on the interface γ .

The schematic of the system is illustrated in Figure 2.1. The term $T(\mathbf{r}_\gamma, \boldsymbol{\Omega}, E, t)$ represents the surface source term in Figure 2.1.

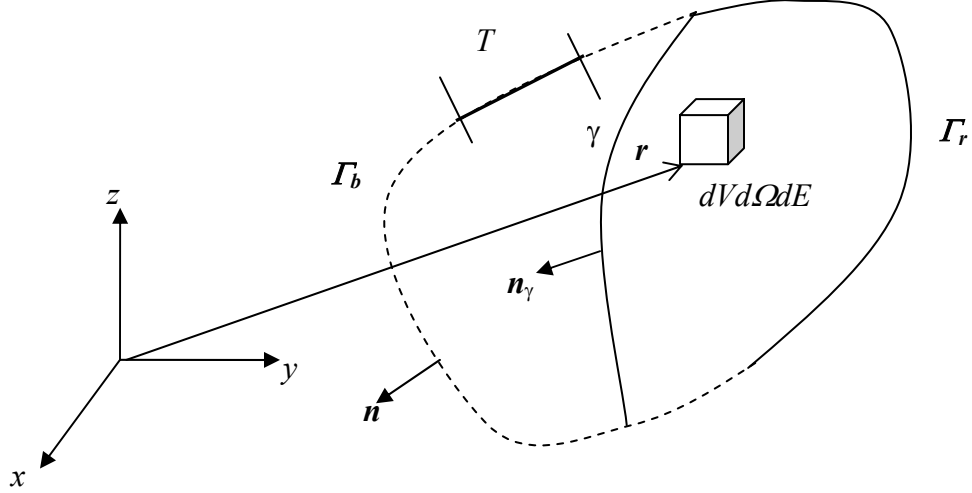


Figure 2.1: Schematics of problem definition

In this thesis, we are mainly concerned with the computational methodology based on steady-state (time-independent) systems. The steady-state transport equation is obtained by simply setting the LHS of Eq. (2.1) to be zero:

$$\begin{aligned} \boldsymbol{\Omega} \cdot \nabla \psi(\mathbf{r}, \boldsymbol{\Omega}, E) + \sigma_t(\mathbf{r}, E) \psi(\mathbf{r}, \boldsymbol{\Omega}, E) = \\ \int_0^\infty dE' \int_{4\pi} d\boldsymbol{\Omega}' \sigma_s(\mathbf{r}, \boldsymbol{\Omega}' \rightarrow \boldsymbol{\Omega}, E' \rightarrow E) \psi(\mathbf{r}, \boldsymbol{\Omega}', E') + S(\mathbf{r}, \boldsymbol{\Omega}, E) \end{aligned} \quad (2.6)$$

2.2 Multigroup Approximation

Analytical or closed form solutions are rarely possible for transport problems. Hence, numerical approximations through the discretization of the independent variables or Monte Carlo are the only practical means for obtaining the neutral particle distributions in the system. In this fashion, the continuous energy variable is often

discretized by the multigroup approximation. The multigroup approximation partitions the energy domain into the G number of bins with intervals of $[E_{g+1}, E_g]$, for $g=1, G$. Integrating energy variable over the predefined bins, results in the energy discretized transport equation:

$$\begin{aligned} \boldsymbol{\Omega} \cdot \nabla \psi_g(\mathbf{r}, \boldsymbol{\Omega}) + \sigma_{tg} \psi_g(\mathbf{r}, \boldsymbol{\Omega}) = \\ \int_{4\pi} d\Omega' \sigma_{sg \rightarrow g}(\mathbf{r}, \boldsymbol{\Omega}' \rightarrow \boldsymbol{\Omega}) \psi_g(\mathbf{r}, \boldsymbol{\Omega}') + S_{g,eff}(\mathbf{r}, \boldsymbol{\Omega}, E) \text{ for } g=1, G \end{aligned} \quad (2.7)$$

where variables with the subscript g denote the integrated values in energy group g . For example, the energy-integrated angular flux $\psi_g(\mathbf{r}, \boldsymbol{\Omega})$ is defined as:

$$\psi_g(\mathbf{r}, \boldsymbol{\Omega}) = \int_{E_{g+1}}^{E_g} dE \psi(\mathbf{r}, \boldsymbol{\Omega}, E) \quad (2.8)$$

The group-dependent cross section is the integrated cross section value weighted by the angular flux:

$$\sigma_g(\mathbf{r}) = \frac{\int_{E_{g+1}}^{E_g} \sigma(\mathbf{r}, E) \psi(\mathbf{r}, \boldsymbol{\Omega}, E) dE}{\int_{E_{g+1}}^{E_g} \psi(\mathbf{r}, \boldsymbol{\Omega}, E) dE} \quad (2.9)$$

Eq. (2.9) preserves the reaction rates in the system. Since in many engineering applications the main quantities of interest are the measured by reaction rates (i.e. power distribution in the reactor core, dose rate in the target organ). This definition of the multigroup cross-section is exact. The last term of the Eq. (2.7) is the effective group source term which is the contribution to group g due to the up- and down-scattering and the extraneous source:

$$S_{g,eff}(\mathbf{r}, \boldsymbol{\Omega}) = S_g(\mathbf{r}, \boldsymbol{\Omega}) + \sum_{\substack{g'=1 \\ g' \neq g}}^G \int d\Omega' \sigma_{sg' \rightarrow g}(\mathbf{r}, \boldsymbol{\Omega}' \rightarrow \boldsymbol{\Omega}) \psi_{g'}(\mathbf{r}, \boldsymbol{\Omega}') \quad (2.10)$$

Since the energy dependence of the exact angular flux is, in general, not known *a priori*, we must introduce an approximated angular flux to obtain the group dependent

cross-sections—hence the multigroup approximation. In this thesis, we assume that the multigroup cross-section data are given for the problems of interest. If we assume the effective source term to be a known quantity, the multigroup transport equation can be treated as a series of energy-independent, mono-energetic transport problems. The mathematical analysis presented in the following chapters is based on the one-speed or one-group transport equation. The subscript g will be thus omitted unless it needs to be expressed explicitly.

2.3 Second-Order, Even-Parity Form of the Transport Equation

In this section, we derive the second-order, even-parity form of the transport equation for a given energy group by the canonical transformation of Eq. (2.7). First, a set of Eq. (2.7) is written for the $+\boldsymbol{\Omega}$ and $-\boldsymbol{\Omega}$ directions:

$$\boldsymbol{\Omega} \cdot \nabla \psi(\mathbf{r}, \boldsymbol{\Omega}) + \sigma_t(\mathbf{r})\psi(\mathbf{r}, \boldsymbol{\Omega}) = \int_{4\pi} d\Omega' \sigma_s(\mathbf{r}, \boldsymbol{\Omega}' \rightarrow \boldsymbol{\Omega})\psi(\mathbf{r}, \boldsymbol{\Omega}') + S(\mathbf{r}, \boldsymbol{\Omega}, E) \quad (2.11)$$

$$-\boldsymbol{\Omega} \cdot \nabla \psi(\mathbf{r}, -\boldsymbol{\Omega}) + \sigma_t(\mathbf{r})\psi(\mathbf{r}, -\boldsymbol{\Omega}) = \int_{4\pi} d\Omega' \sigma_s(\mathbf{r}, \boldsymbol{\Omega}' \rightarrow -\boldsymbol{\Omega})\psi(\mathbf{r}, \boldsymbol{\Omega}') + S(\mathbf{r}, -\boldsymbol{\Omega}, E) \quad (2.12)$$

The canonical form of the transport equation is obtained by adding Eq. (2.11) and Eq.

(2.12):

$$\boldsymbol{\Omega} \cdot \nabla \phi^-(\mathbf{r}, \boldsymbol{\Omega}) + \sigma_t \phi^+(\mathbf{r}, \boldsymbol{\Omega}) = \int_{4\pi} d\Omega' \sigma_s^+(\mathbf{r}, \boldsymbol{\Omega}' \rightarrow \boldsymbol{\Omega})\psi(\mathbf{r}, \boldsymbol{\Omega}') + S^+(\mathbf{r}, \boldsymbol{\Omega}, E) \quad (2.13)$$

and, by subtracting Eq. (2.11) from Eq. (2.12)

$$\boldsymbol{\Omega} \cdot \nabla \phi^+(\mathbf{r}, \boldsymbol{\Omega}) + \sigma_t \phi^-(\mathbf{r}, \boldsymbol{\Omega}) = \int_{4\pi} d\Omega' \sigma_s^-(\mathbf{r}, \boldsymbol{\Omega}' \rightarrow \boldsymbol{\Omega})\psi(\mathbf{r}, \boldsymbol{\Omega}') + S^-(\mathbf{r}, \boldsymbol{\Omega}, E) \quad (2.14)$$

where, $\phi^\pm(\mathbf{r}, \boldsymbol{\Omega}) = \frac{1}{2}[\psi(\mathbf{r}, \boldsymbol{\Omega}) \pm \psi(\mathbf{r}, -\boldsymbol{\Omega})]$ are the even- and odd-parity components of

the angular flux, or $\psi(\mathbf{r}, \boldsymbol{\Omega}) = \phi^+(\mathbf{r}, \boldsymbol{\Omega}) + \phi^-(\mathbf{r}, \boldsymbol{\Omega})$,

$S^\pm(\mathbf{r}, \boldsymbol{\Omega}) = \frac{1}{2}[S(\mathbf{r}, \boldsymbol{\Omega}) \pm S(\mathbf{r}, -\boldsymbol{\Omega})]$ are the even- and odd-parity components of the

source term, and

$\sigma_s^\pm(\mathbf{r}, \boldsymbol{\Omega}' \rightarrow \boldsymbol{\Omega}) = \sigma_s(\mathbf{r}, \boldsymbol{\Omega}' \rightarrow \boldsymbol{\Omega}) \pm \sigma_s(\mathbf{r}, \boldsymbol{\Omega}' \rightarrow -\boldsymbol{\Omega})$ are the even- and odd-parity components of the scattering phase function.

The angular flux term still remains in the scattering integral; however, if we assume that the scattering kernel is invariant under the rotation, (i.e. the scattering does not depend on the incoming angle, but only depends on the angle between $\boldsymbol{\Omega}$ and $\boldsymbol{\Omega}'$) the term can be simplified by recognizing the odd function vanishes with integration over all directions

4π , (i.e. $\int_{4\pi} d\Omega' \sigma_s^\pm(\mathbf{r}, \boldsymbol{\Omega}' \cdot \boldsymbol{\Omega}) \phi^\mp(\mathbf{r}, \boldsymbol{\Omega}') = 0$). Thus Eq. (2.13) can be written as:

$$\boldsymbol{\Omega} \cdot \nabla \phi^-(\mathbf{r}, \boldsymbol{\Omega}) + \sigma_t \phi^+(\mathbf{r}, \boldsymbol{\Omega}) = \int_{4\pi} d\Omega' \sigma_s^+(\mathbf{r}, \boldsymbol{\Omega}' \cdot \boldsymbol{\Omega}) \phi^+(\mathbf{r}, \boldsymbol{\Omega}') + S^+(\mathbf{r}, \boldsymbol{\Omega}, E) \quad (2.15)$$

Let us define the two collision operator G and C as:

$$G^{-1} f^-(\boldsymbol{\Omega}) = \sigma_t f^-(\boldsymbol{\Omega}) - \int_{4\pi} d\Omega' \sigma_s^-(\boldsymbol{\Omega} \cdot \boldsymbol{\Omega}') f^-(\boldsymbol{\Omega}') \quad (2.16)$$

$$C f^+(\boldsymbol{\Omega}) = \sigma_t f^+(\boldsymbol{\Omega}) - \int_{4\pi} d\Omega' \sigma_s^+(\boldsymbol{\Omega} \cdot \boldsymbol{\Omega}') f^+(\boldsymbol{\Omega}') \quad (2.17)$$

Due to the assumption of rotational invariance, the scattering kernel can be expanded in terms of Legendre polynomials:

$$\sigma_s^+(\mathbf{r}, \boldsymbol{\Omega} \cdot \boldsymbol{\Omega}') = \sum_{\substack{l=0 \\ (even)}}^{\infty} \frac{2l+1}{4\pi} P_l(\mu_0) \sigma_{sl}(\mathbf{r}) \quad (2.18)$$

$$\sigma_s^-(\mathbf{r}, \boldsymbol{\Omega} \cdot \boldsymbol{\Omega}') = \sum_{\substack{l=1 \\ (odd)}}^{\infty} \frac{2l+1}{4\pi} P_l(\mu_0) \sigma_{sl}(\mathbf{r}) \quad (2.19)$$

where, μ_0 is the cosine of the angle between $\boldsymbol{\Omega}$ and $\boldsymbol{\Omega}'$.

In order to simplify the collision operators, first we recognize that the delta function can formally be represented by the infinite sum of Legendre polynomials:

$$\delta(\boldsymbol{\Omega} - \boldsymbol{\Omega}') = \sum_{l=0}^{\infty} \frac{2l+1}{4\pi} P_l(\mu_0) . \quad (2.20)$$

Utilizing the delta function property, the total interaction term becomes:

$$\sigma_t f(\boldsymbol{\Omega}) = \int_{4\pi} d\Omega' \sum_{l=0}^{\infty} \frac{2l+1}{4\pi} P_l(\mu_0) \sigma_t f(\boldsymbol{\Omega}') \quad (2.21)$$

Therefore, the collision operators can be expressed as:

$$G^{-1} f^+(\boldsymbol{\Omega}) = \sum_{\substack{l=1 \\ (odd)}}^{\infty} \int_{4\pi} d\Omega' [\sigma_t - \sigma_s^-(\mu_0)] f^+(\boldsymbol{\Omega}') \quad (2.22)$$

$$C f^+(\boldsymbol{\Omega}) = \sum_{\substack{l=0 \\ (even)}}^{\infty} \int_{4\pi} d\Omega' [\sigma_t - \sigma_s^+(\mu_0)] f^+(\boldsymbol{\Omega}') \quad (2.23)$$

Eq. (2.13) and (2.14) are then expressed in terms of G and C :

$$\boldsymbol{\Omega} \cdot \nabla \phi^+(\mathbf{r}, \boldsymbol{\Omega}) + G^{-1} \phi^-(\mathbf{r}, \boldsymbol{\Omega}) = S^-(\mathbf{r}, \boldsymbol{\Omega}) \quad (2.24)$$

$$\boldsymbol{\Omega} \cdot \nabla \phi^-(\mathbf{r}, \boldsymbol{\Omega}) + C \phi^+(\mathbf{r}, \boldsymbol{\Omega}) = S^+(\mathbf{r}, \boldsymbol{\Omega}) \quad (2.25)$$

The inverse of the operator G exists [37, 20]. As a result, Eq. (2.24) is rearranged in terms of the odd-parity flux:

$$\phi^-(\mathbf{r}, \boldsymbol{\Omega}) = G \left[S^-(\mathbf{r}, \boldsymbol{\Omega}) - \boldsymbol{\Omega} \cdot \nabla \phi^+(\mathbf{r}, \boldsymbol{\Omega}) \right] \quad (2.26)$$

Substituting Eq. (2.26) into Eq. (2.25) finally yields desired even-parity transport equation:

$$-\boldsymbol{\Omega} \cdot \nabla G \boldsymbol{\Omega} \cdot \nabla \phi^+ + C \phi^+ = S^+ - \boldsymbol{\Omega} \cdot \nabla G S^- \quad (2.27)$$

The boundary and interface conditions can be prescribed by the linear combination of even- and odd-parity fluxes.

2.3.1 Vacuum Boundary Condition

The vacuum boundary condition for the even-parity transport equation is an exact analogue to the first-order form of the transport equation. Since the angular flux is represented by the sum of the even and odd-parity fluxes, the vacuum boundary condition can be written as:

$$\phi^+(\mathbf{r}_{\Gamma_b}, \boldsymbol{\Omega}) + \phi^-(\mathbf{r}_{\Gamma_b}, \boldsymbol{\Omega}) = 0 \text{ for } \mathbf{n} \cdot \boldsymbol{\Omega} < 0 \quad (2.28)$$

or utilizing Eq. (2.26) with disregarding for the moment the odd-parity source:

$$\begin{aligned}\phi^+(\mathbf{r}_{\Gamma_b}, \boldsymbol{\Omega}) &= -\phi^-(\mathbf{r}_{\Gamma_b}, \boldsymbol{\Omega}) \\ &= G\boldsymbol{\Omega} \cdot \nabla \phi^+(\mathbf{r}, \boldsymbol{\Omega}) \text{ for } \mathbf{n} \cdot \boldsymbol{\Omega} < 0\end{aligned}\tag{2.29}$$

Since the vacuum boundary condition employs both the even-parity flux and its derivative, it is commonly referred to as a Robin boundary condition.

2.3.2 Reflective Boundary Condition

The reflective boundary condition can be easily introduced by recognizing the characteristics of the parity flux:

$$\begin{aligned}\phi^+(\mathbf{r}_{\Gamma_r}, \boldsymbol{\Omega}) &= \phi^+(\mathbf{r}_{\Gamma_r}, \boldsymbol{\Omega}^*), \\ \phi^-(\mathbf{r}_{\Gamma_r}, \boldsymbol{\Omega}) &= -\phi^-(\mathbf{r}_{\Gamma_r}, \boldsymbol{\Omega}^*), \text{ where } \boldsymbol{\Omega}^* = \boldsymbol{\Omega} - 2(\mathbf{n} \cdot \boldsymbol{\Omega})\mathbf{n}\end{aligned}\tag{2.30}$$

As we shall see in the next chapter, the reflective boundary condition is also called essential boundary condition.

2.3.3 Material Interface Conditions

At a material interface, both even- and odd-parity flux are continuous along the direction of particle travel. Therefore, the interface conditions can be represented as:

(i) flux continuity:

$$\lim_{\varepsilon \rightarrow 0} [\phi^+(\mathbf{r}_\gamma + \varepsilon \boldsymbol{\Omega}, \boldsymbol{\Omega}) - \phi^+(\mathbf{r}_\gamma - \varepsilon \boldsymbol{\Omega}, \boldsymbol{\Omega})] = 0\tag{2.31}$$

(ii) current continuity:

$$\lim_{\varepsilon \rightarrow 0} [\phi^-(\mathbf{r}_\gamma + \varepsilon \boldsymbol{\Omega}, \boldsymbol{\Omega}) - \phi^-(\mathbf{r}_\gamma - \varepsilon \boldsymbol{\Omega}, \boldsymbol{\Omega})] = 0\tag{2.32}$$

Eq. (2.27) has several advantages over the first-order form of the transport equation. First of all, the solution of Eq. (2.27) requires only half of the angular unknowns compared to the first-order formulation. This is particularly useful when spherical harmonics functions are employed as the angular basis functions; the odd angular basis functions identically vanish due to the orthogonal property of the spherical harmonics. Moreover, since the operators G and C are positive definite operators [37]; the well-

established mathematical framework can be adapted to the problem, and the finite element-spherical harmonics (FE- P_N) formulation gives rise to symmetric positive definite (SPD) matrices.

A main drawback in the even-parity formulation is the dependence on the reciprocal of the cross section that appears in the operator G . This dependence leads to ill-posedness for the problem when the region becomes highly transparent. In particular, the even-parity equation is not valid for vacuum regions ($\sigma = 0$). Systems with very small cross sections often have very large condition number for the resulting matrix formulation, which makes the iterative scheme difficult to converge. One way of overcoming this difficulty of treating the vacuum or nearly vacuum regions is adopting a “ray-tracing” method [38] for those regions. In the ray-tracing method, the (nearly) vacuum regions are treated separately from the rest of the system, and artificial surfaces are created to connect the two systems. The radiation transport problem in the vacuum region is then solved by connecting the surfaces through discrete rays. The coupling between the vacuum and rest of the system is done by exchanging surface sources, and an iterative procedure is performed until the surface sources have converged.

2.4 Summary

In this chapter, we have introduced the governing integro-differential equation for the radiation transport problem. Simplification of transport problems by means of a steady state, multigroup approximations was presented. The second-order, even-parity form of the transport equation, which is the basis of our numerical method, was derived via the canonical transformation. We have also shown the collision operators, expanded in Legendre polynomials, allow an implicit treatment of the scattering kernel. The elliptic property of the even-parity transport equation allows us to use strong mathematical theory developed over the years, and mathematical formulations that will be presented in the later chapters deeply rely on this elliptic property of the governing equation.

CHAPTER 3

THE FINITE ELEMENT SPHERICAL HARMONICS METHOD

In this thesis discretization of the spatial and angular variables is achieved via the finite element-spherical harmonics (FE-P_N) method. Finite element analysis has become popular tool for the engineering analysis due to its flexibility in representing arbitrary geometries. Spherical harmonics expansions of the angular variables provide a natural treatment for the scattering operators. In this chapter, we discuss the FE-P_N discretization of the even-parity transport equation through the well-known Ritz-Galerkin procedure.

3.1 Even-Parity Variational Principle

A large number of variational principles have been proposed in the context of the transport theory. In this chapter, we employ the extremum variational principle of the even-parity transport equation which was first introduced by Vladimirov [19]. This variational principle has the even-parity transport equation as its Euler equation, and can be derived by the systematic methodology suggested by Pomraning [39], Lewins [40], and Stacey [18].

First, we introduce the adjoint problem corresponding to Eq. (2.26):

$$-\boldsymbol{\Omega} \cdot \nabla G \boldsymbol{\Omega} \cdot \nabla \phi^{+*} + C \phi^{+*} = S^{+*} - \boldsymbol{\Omega} \cdot \nabla G S^{-*} \quad (3.1)$$

where, ϕ^{+*} is the even-parity angular flux of the adjoint problem, and

$S^{\pm*}$ are the parity components of the adjoint source terms.

Since the adjoint source term is arbitrary, it is, in general, possible to express the quantity of interest by the inner product between the even-parity flux and the adjoint source term.

Suppose that we are interested in identifying the quantity of interest defined by the following functional:

$$F_s^*[\phi^+] = \langle \phi^+, T^* \rangle + (\phi^+, S^{+*}) - (\phi^+, \boldsymbol{\Omega} \cdot \nabla G S^{-*}) \quad (3.2)$$

where, $(.,.) \equiv \int_{4\pi} d\Omega \int_V dV$,

$$\langle ., . \rangle \equiv \int_{4\pi} d\Omega \int_{\partial V} d\Gamma |\boldsymbol{\Omega} \cdot \mathbf{n}|, \text{ and}$$

T^* is the adjoint surface source.

In practice, Eq. (3.2) can represent the various reaction rates in the system when the adjoint source term is set to a cross section of interest ($S^* = \sigma$), or the leakage rate through the particular surface if the adjoint surface source term is the unit surface source.

The variational principle corresponding to the functional (3.2) is then obtained by adding the inner product between the adjoint solution and the original governing equation (2.26). As a result, we obtain the following variational principle:

$$\begin{aligned} K^+[\phi^*, \phi^+] &= F_s^*[\phi^+] + (\phi^*, S^+ - \boldsymbol{\Omega} \cdot \nabla G S^- + \boldsymbol{\Omega} \cdot \nabla G \boldsymbol{\Omega} \cdot \nabla \phi^+ - C\phi^+) \\ &= F_s^*[\phi^+] - (\boldsymbol{\Omega} \cdot \nabla \phi^*, G \boldsymbol{\Omega} \cdot \nabla \phi^+) - (\phi^*, C\phi^+) \\ &\quad - \langle \phi^*, \phi^+ \rangle + \langle \phi^*, T \rangle + (\phi^*, S^+) - (\phi^*, \boldsymbol{\Omega} \cdot \nabla G S^-) \end{aligned} \quad (3.3)$$

The last equality is obtained from the divergence theorem. Vladimirov's variational principle can be easily constructed from Eq (3.3) by equating the adjoint problem to the original problem. Eq. (3.3) can then be rewritten as the following quadratic variational functional:

$$\begin{aligned} K^+[\psi] &= (\boldsymbol{\Omega} \cdot \nabla \psi, G \boldsymbol{\Omega} \cdot \nabla \psi) + (\psi, C\psi) + \langle \psi, \psi \rangle \\ &\quad - 2(\psi, S^+) - 2\langle \psi, T \rangle - 2(\boldsymbol{\Omega} \cdot \nabla \psi, G S^-) \end{aligned} \quad (3.4)$$

In order to show the Eq. (3.4) has the original equation as its Euler equation, we take the first variation with respect to ψ .

$$\begin{aligned} \delta K^+[\psi] &= 2(\boldsymbol{\Omega} \cdot \nabla \delta\psi, G \boldsymbol{\Omega} \cdot \nabla \psi) + 2(\delta\psi, C\psi) + 2\langle \delta\psi, \psi \rangle \\ &\quad - 2(\delta\psi, S^+) - 2\langle \delta\psi, T \rangle - 2(\boldsymbol{\Omega} \cdot \nabla \delta\psi, G S^-) \\ &= 2(\delta\psi, -\boldsymbol{\Omega} \cdot \nabla G \boldsymbol{\Omega} \cdot \nabla \psi + C\psi - S^+ + \boldsymbol{\Omega} \cdot \nabla G S^-) \\ &\quad + 2\langle \delta\psi, \psi + G[S^- - \boldsymbol{\Omega} \cdot \nabla \psi] - T \rangle \end{aligned} \quad (3.5)$$

For the first variation $\delta K[\psi]$ to vanish under arbitrary variations of $\delta\psi$, the following two equations have to be satisfied:

$$-\mathbf{\Omega} \cdot \nabla G \mathbf{\Omega} \cdot \nabla \psi + C\psi = S^+ - \mathbf{\Omega} \cdot \nabla G S^- \text{ on } V \quad (3.6)$$

$$\psi + G[S^- - \mathbf{\Omega} \cdot \nabla \psi] = T \text{ on } \Gamma \quad (3.7)$$

Therefore, the function at which Eq. (3.4) gives the extremum value satisfies the even-parity transport equation. The second variation of the Eq. (3.4) is a positive quantity; therefore, the quadratic variational functional (3.4) has a characteristic such that the function, which minimizes the functional (3.4) within a given set of functions, is the best possible solution in least-square sense. Figure 3.1 illustrates that the geometrical interpretation of the variational principle [37].

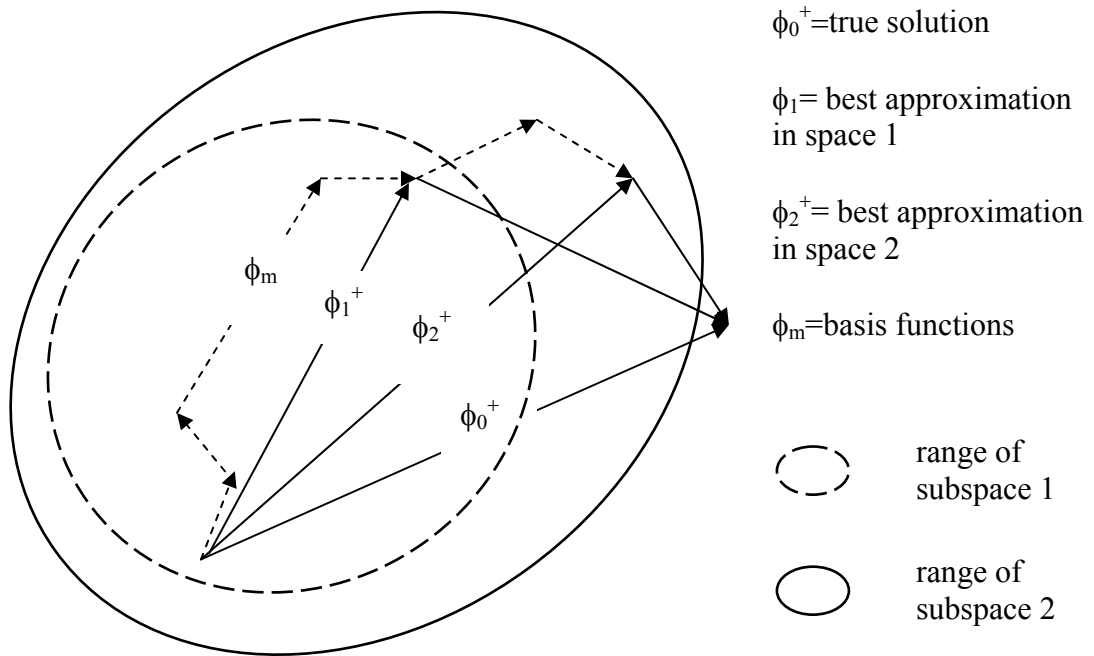


Figure 3.1: Illustration of the extremum variational principle [37]

3.2 The Finite Element-Spherical Harmonics Discretization

The finite element method is a powerful analysis tool for obtaining the numerical approximations of partial differential equations. The basic philosophy behind the finite element method is to discretize the problem domain into number of sub-regions, and approximate the solution by a collection of the simple piecewise functions which minimize the corresponding functional. The finite element method is thus closely related to the variational methodology. In particular, rigorous mathematical analysis is available to prove its convergence and uniqueness of the numerical solutions [41] for the case of elliptic-type problems. In addition to the strong mathematical framework, the main advantage of the finite element method is its geometrical flexibility; complex domains can be handled readily and the boundary conditions can be treated in a systematic way.

In deterministic radiation transport modeling, angular variables are often discretized via (a) discrete ordinates (S_N) or (b) the classical spherical harmonics (P_N) method. This gives a set of coupled PDE's which can be solved by conventional numerical schemes. There are several advantages using the P_N method over the S_N method; (1) the spherical harmonics allows the natural treatment of the scattering kernel [42], and (2) no ray effect is observed [1]. In the next section, we briefly introduce the spherical harmonics angular approximation.

3.2.1 The Spherical Harmonics Angular Approximation

The angular flux can be expanded by:

$$\psi(\mathbf{r}, \boldsymbol{\Omega}) = \sum_{l=0}^{\infty} \sum_{m=-l}^l Y_{lm}(\boldsymbol{\Omega}) \psi_{lm}(\mathbf{r}) \quad (3.8)$$

where, Y_{lm} is the l - and m -th moment of the spherical harmonics function, which is defined as [1]:

$$Y_{lm}(\boldsymbol{\Omega}) = C_{lm}^{1/2} P_l^m(\mu) e^{im\phi} \quad (3.9)$$

where, $C_{lm} = \frac{(2l+1)(l-m)!}{(l+m)!}$ is the normalization constant,

$P_l(\mu) = \frac{1}{2^l l!} \frac{d^l}{d\mu^l} (\mu^2 - 1)$ is the l -th moment of the Legendre polynomials, and

$P_l^m(\mu) = (-1)^m (1 - \mu^2)^{m/2} \frac{d^m}{d\mu^m} P_l(\mu)$ is the l - and m -th moment of the associated

Legendre functions.

The spherical harmonics functions obey the following orthogonality relations:

$$\int d\Omega Y_{lm}(\boldsymbol{\Omega}) Y_{l'm'}^*(\boldsymbol{\Omega}) = \delta_{ll'} \delta_{mm'} \quad (3.10)$$

where $Y_{lm}^*(\boldsymbol{\Omega}) = (-1)^m Y_{lm}(\boldsymbol{\Omega})$ is the complex conjugate function.

The spherical harmonics (3.9) can be split into even and odd components with respect to the azimuthal components ω :

$$Y_{lm}(\boldsymbol{\Omega}) = Y_{lm}^e(\boldsymbol{\Omega}) + i Y_{lm}^o(\boldsymbol{\Omega}), \quad (3.11)$$

where, $Y_{lm}^e(\boldsymbol{\Omega}) = C_{lm}^{1/2} P_l^m(\mu) \cos(m\omega)$, and

$$Y_{lm}^o(\boldsymbol{\Omega}) = C_{lm}^{1/2} P_l^m(\mu) \sin(m\omega).$$

The parity components of the spherical harmonics in turn obey the following orthogonality relations:

$$\int d\Omega Y_{lm}^e(\boldsymbol{\Omega}) Y_{l'm'}^e(\boldsymbol{\Omega}) = \frac{1}{2} (1 + \delta_{m0}) \delta_{ll'} \delta_{mm'} \quad (3.12)$$

$$\int d\Omega Y_{lm}^o(\boldsymbol{\Omega}) Y_{l'm'}^o(\boldsymbol{\Omega}) = \frac{1}{2} (1 - \delta_{m0}) \delta_{ll'} \delta_{mm'} \quad (3.13)$$

Representation of the angular dependence by the even and odd spherical harmonics functions turns out to be a convenient choice [42]. For example, the addition theorem can be represented as:

$$P_l(\boldsymbol{\Omega} \cdot \boldsymbol{\Omega}') = \frac{4\pi}{2l+1} \sum_{m=0}^l Y_{lm}^e(\boldsymbol{\Omega}) Y_{lm}^e(\boldsymbol{\Omega}') + Y_{lm}^o(\boldsymbol{\Omega}) Y_{lm}^o(\boldsymbol{\Omega}') \quad (3.14)$$

Then, the collision operator G and C can be written as:

$$\begin{aligned}
Gf(\boldsymbol{\Omega}) &= \int_{4\pi} d\boldsymbol{\Omega}' \sum_{l=0}^{L, \text{odd}} \sum_{m=0}^l \frac{1}{\sigma_l^-} \{Y_{lm}^e(\boldsymbol{\Omega})Y_{lm}^e(\boldsymbol{\Omega}') + Y_{lm}^o(\boldsymbol{\Omega})Y_{lm}^o(\boldsymbol{\Omega}')\} f(\boldsymbol{\Omega}') \\
&= \sum_{l=0}^{L, \text{odd}} \sum_{m=0}^l \frac{1}{\sigma_l^-} \{Y_{lm}^e(\boldsymbol{\Omega})f_{lm}^e + Y_{lm}^o(\boldsymbol{\Omega})f_{lm}^o\}
\end{aligned} \tag{3.15}$$

$$\begin{aligned}
Cf(\boldsymbol{\Omega}) &= \int_{4\pi} d\boldsymbol{\Omega}' \sum_{l=0}^{L, \text{even}} \sum_{m=0}^l \sigma_l^+ \{Y_{lm}^e(\boldsymbol{\Omega})Y_{lm}^e(\boldsymbol{\Omega}') + Y_{lm}^o(\boldsymbol{\Omega})Y_{lm}^o(\boldsymbol{\Omega}')\} f(\boldsymbol{\Omega}') \\
&= \sum_{l=0}^{L, \text{even}} \sum_{m=0}^l \sigma_l^+ \{Y_{lm}^e(\boldsymbol{\Omega})f_{lm}^e + Y_{lm}^o(\boldsymbol{\Omega})f_{lm}^o\}
\end{aligned} \tag{3.16}$$

Therefore, the integral collision operators are reduced to the summation over the spherical harmonics moments.

3.2.2 The Finite Element Approximation

The spatial dependence of the even-parity flux can be approximated by the piecewise continuous functions;

$$\psi(\mathbf{r}, \boldsymbol{\Omega}) = \sum_{e=1}^E \sum_{j=1}^{N_e} \sum_{k=1}^M B_j^e(\mathbf{r}) Q_k(\boldsymbol{\Omega}) \psi_{jk}^e \tag{3.17}$$

where, E is the number of non-overlapping elements connected together at N nodal points.

N_e is the number of spatial basis function for the element e ,

M is the number of moments in the angular expansion,

B_j^e is the j -th spatial basis function for the element e , and

Q_k is the k -th angular basis function.

This expansion can be expressed in a more compact tensor notation:

$$\psi(\mathbf{r}, \boldsymbol{\Omega}) = \sum_{e=1}^E B^{eT} \otimes Q^T \psi^e \tag{3.18}$$

where, ψ^e is a $(MN_e \times I)$ column vector of unknown nodal fluxes,

B^{eT} is a $(N_e \times I)$ column vector of finite element shape functions, and

$Q(\boldsymbol{\Omega})$ is a $(M \times I)$ column vector of normalized spherical harmonics functions.

The spatial basis functions used in the finite element method are characterized by their locality. In other words, they are defined such that they only span the interior of an element and vanish on the outside. Figure 3.2 illustrates the typical linear basis function in two dimensional problems.

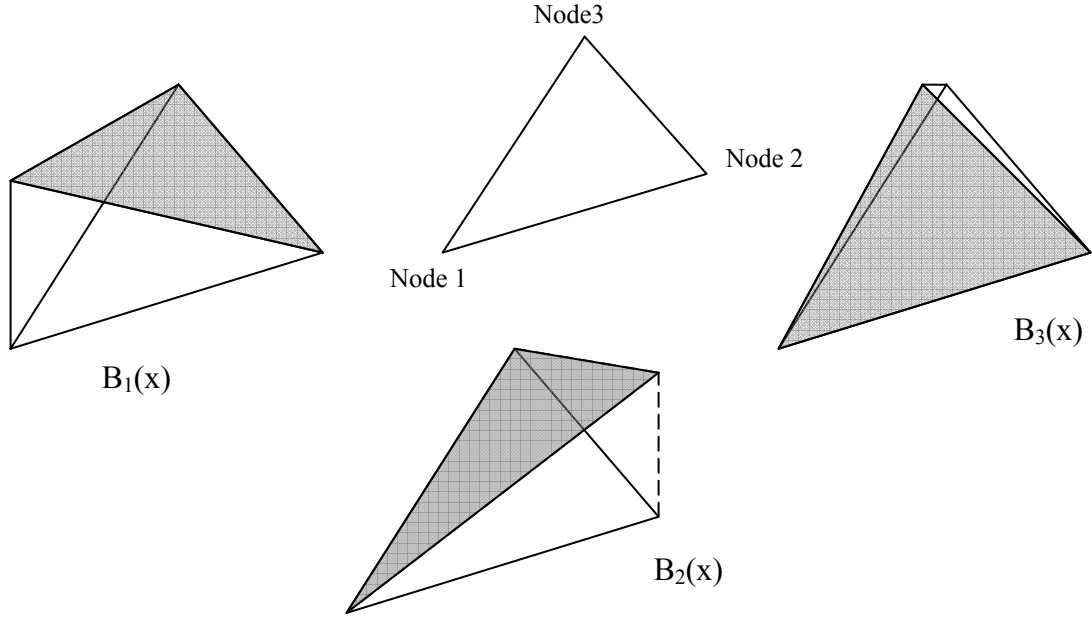


Figure 3.2: Typical two-dimensional triangular element and its linear basis functions

3.2.3 Ritz-Galerkin Procedure

Numerical solutions for the variational principle (3.4) are possible via the well-known Ritz-Galerkin procedure. Substituting Eq. (3.18) into (3.4), we obtain the reduced (or discretized) variational functional:

$$K^+[\psi] = \sum_{e=1}^E \psi^{eT} A^e \psi^e - 2\psi^T b \quad (3.19)$$

where,

$$A^e \equiv \left(\boldsymbol{\Omega} \cdot \nabla B^{eT} \otimes Q^T, G \boldsymbol{\Omega} \cdot \nabla B^{eT} \otimes Q^T \right) + \left(B^{eT} \otimes Q^T, C B^{eT} \otimes Q^T \right) + \left\langle B^{eT} \otimes Q^T, B^{eT} \otimes Q^T \right\rangle \quad (3.20)$$

and

$$b^e \equiv (B^{eT} \otimes Q^T, S^+) + \langle B^{eT} \otimes Q^T, T \rangle + (\boldsymbol{\Omega} \cdot \nabla B^{eT} \otimes Q^T, G \boldsymbol{\Omega} \cdot \nabla S^-) \quad (3.21)$$

are the elements of the stiffness matrix and load or force vector, respectively. These require the evaluation of several spatial angular integrals. Table 3.1 summarizes these spatial and angular integral tables.

Table 3.1: Spatial and angular integral tables used in the FE-P_N method

Physics	Spatial Integral	Angular Integral
Leakage	$\int_{V_e} dV \frac{dB_n(\mathbf{r})}{dx_i} \frac{dB_m(\mathbf{r})}{dx_j}$	$\int_{4\pi} d\Omega \Omega_i Q_l(\boldsymbol{\Omega}) Q_{l'}(\boldsymbol{\Omega})$
Absorption	$\int_{V_e} dV B_n(\mathbf{r}) B_m(\mathbf{r})$	$\int_{4\pi} d\Omega Q_l(\boldsymbol{\Omega}) Q_{l'}(\boldsymbol{\Omega})$
Parity Source	$\int_{V_e} dV B_n(\mathbf{r})$ $\int_{V_e} dV \frac{dB_n(\mathbf{r})}{dx_i}$	$\int_{4\pi} d\Omega Q_l(\boldsymbol{\Omega}) Q_{l'}(\boldsymbol{\Omega})$ $\int_{4\pi} d\Omega \Omega_i Q_l(\boldsymbol{\Omega}) Q_{l'}(\boldsymbol{\Omega})$
Surface Source	$\int_{\partial V_e} d\Gamma B_n(\mathbf{r}) B_m(\mathbf{r})$	$\int_{2\pi} d\Omega \boldsymbol{\Omega} \cdot \mathbf{n} Q_l(\boldsymbol{\Omega}) Q_{l'}(\boldsymbol{\Omega})$

In Table 3.1, n and m denote the index of the basis function related to the local node number, i and j denote the orthogonal components of the spatial coordinates, and l and l' denote the moment of spherical harmonics. The angular basis functions with prime (Q') are the odd-moments of the spherical harmonics functions.

Making use of nodal compatibility, and requiring the first variation of Eq. (3.19) to vanish, we obtain the linear system of equations of the form [43]:

$$A\psi = \mathbf{b} \quad (3.22)$$

where, ψ is a $(MN \times 1)$ unknown column vector, $A = \sum_{e=1}^E A^e$ is a $(MN \times MN)$ symmetric positive definite (SPD) matrix, and $\mathbf{b} = \sum_{e=1}^E \mathbf{b}^e$ is a $(MN \times 1)$ source vector.

3.3 General Solution Strategy Applied to the FE-P_N Method

Thus far, we have reviewed the discretization scheme used in the FE-P_N formulation. The resulting matrix A is sparse due to the locality of the finite element basis function. However, for large problems, the explicit assembly of the matrix A soon becomes prohibitive since the matrix size increases as $O(M^2)$, not taking into account the energy dependence in the problem. To overcome this problem a special sparse iterative solution strategy needs to be considered. This strategy is based on the preconditioned conjugate gradient (PCG) method [44] which is popular iterative scheme to solve the SPD system. The algorithm of the PCG is shown in Figure 3.3.

```

Given  $A$ ,  $b$  and  $x^{(0)}$ , compute  $r^{(0)} = b - Ax^{(0)}$ 
DO  $i=1, 2 \dots$  until converges
  Solve  $Mz^{(i-1)} = r^{(i-1)}$ 
   $\rho_{i-1} = z^{(i-1)T} r^{(i-1)}$ 
  if  $i=1$ 
     $p^{(i)} = z^{(i-1)}$ 
  else
     $\beta_{i-1} = \rho_{i-1} / \rho_{i-2}$ 
     $p^{(i)} = z^{(i-1)} + \beta_{i-1} p^{(i-1)}$ 
  endif

   $q^{(i)} = Ap^{(i)}$ 
   $\alpha_i = \rho_{i-1} / (p^{(i)T} q^{(i)})$ 
   $x^{(i)} = x^{(i-1)} + \alpha_i p^{(i)}$ 
   $r^{(i)} = r^{(i-1)} - \alpha_i q^{(i)}$ 

```

Figure 3.3: The preconditioned conjugate gradient algorithm

In the PCG algorithm, the only matrix operation which involves matrix \mathbf{A} is the matrix vector product. Therefore, the explicit assembly of the matrix \mathbf{A} is not necessary so long as the matrix vector multiplication can be performed efficiently. The crucial step to the success in the PCG method is a choice of the preconditioner \mathbf{M} . This has to be as close as possible approximation to the matrix \mathbf{A} but easier to invert. The condition number of the PCG is dictated by the condition number of $\mathbf{M}^{-1}\mathbf{A}$. The closer preconditioning matrix being \mathbf{A} , the higher the convergence rate becomes. Naturally, if the preconditioner is the exact matrix \mathbf{A} , the PCG iteration converges at the first step. Taking into consideration above mentioned two issues (storage requirements and convergence rate of the PCG), a Moment-by-Moment (MBM) SSOR preconditioner [36] is a strong candidate of the solution of the FE-P_N equations. In the MBM method the matrix \mathbf{A} is partitioned into $M \times M$ sub-matrices of dimension $N \times N$:

$$\mathbf{A} = \begin{pmatrix} \mathbf{A}_{11} & \mathbf{A}_{12} & \dots & \mathbf{A}_{1M} \\ \mathbf{A}_{12}^T & \mathbf{A}_{22} & \dots & \dots \\ \dots & \dots & \dots & \mathbf{A}_{M-1M} \\ \mathbf{A}_{1M}^T & \dots & \mathbf{A}_{M-1M}^T & \mathbf{A}_{MM} \end{pmatrix} \quad (3.23)$$

where each block matrix $\mathbf{A}_{ll'}$ contains the spatial finite elements connections of angular moment l and l' . Then, the MBM preconditioner can be written as the following form:

$$\mathbf{M} = (\mathbf{D} + \mathbf{L})\mathbf{D}^{-1}(\mathbf{D} + \mathbf{L}^T) \quad (3.24)$$

where,

$$\mathbf{L}_{ij} = \begin{cases} \mathbf{A}_{ij} & \text{if moment } i > j \\ 0 & \text{otherwise} \end{cases} \quad \mathbf{D}_{ij} = \begin{cases} \mathbf{A}_{ij} & \text{if moment } i=j \\ 0 & \text{otherwise} \end{cases}$$

The MBM preconditioning stage is solved by the block forward-backward sweep. The advantage of this preconditioner is the storage cost: only the block diagonal sub-matrices need to be explicitly assembled. Matrix-vector multiplications regarding the off-diagonal matrices are carried out via the tensorial operations of the space-moment matrix stencil. The tensorial nature of the FE-P_N formulation allows storing the angular integrals and

spatial element integrals separately, and this allows a considerable reduction in the storage cost with little expense in the computational cost at the preconditioning stage.

3.4 Summary

In this chapter, we have derived the even-parity variational principles by utilizing the adjoint problem. The finite element-spherical harmonics discretization is then introduced through the Ritz-Galerkin procedure. The resulting discretized system is symmetric positive definite, which naturally suits to use of the well-known preconditioned conjugate gradient. A Moment-by-Moment SSOR preconditioner for the coupled space-angle matrices and a general solution strategy were briefly discussed.

CHAPTER 4

A POSTERIORI ERROR ANALYSIS AND ADAPTIVITY

FRAMEWORK FOR RADIATION TRANSPORT PROBLEMS

In the previous chapter, the development of the finite element-spherical harmonics discretization method was discussed. The FE- P_N method based on the Ritz-Galerkin procedure yields the best approximate solution (in a global least-square sense) within the approximation space. However, the numerical solution is always susceptible to the discretization error, whose quantity is not known *a priori*. Identification and minimization of the discretization errors are of utmost importance for simulations to become reliable analysis tools. Although a discretization resulting from an experienced engineering judgment sometimes gives an acceptable result, minimization of the discretization error within a framework of the available computational resources requires a strong mathematical framework. *A posteriori* error analysis is potentially capable of providing a powerful framework estimating the discretization errors. In this chapter, we derive *a posteriori* error estimates and develop an adaptivity framework for the radiation transport problems.

4.1 *A Priori* Error Estimates

An important feature of any numerical algorithm for approximating PDEs is the convergence property. Suitable numerical schemes should have a property such that the numerical solution converges towards the exact solution as the spatial mesh size h and angular expansion orders N tend to 0 and ∞ , respectively. The convergence property of the finite element method has been studied extensively. Especially, for the elliptic problems with linear basis trial functions, the following *a priori* error estimates holds [45, 41],:

$$\|u - u_h\|_{L_2} \leq c_1 h^2 \quad (4.1)$$

$$\|u - u_h\| \leq c_2 h \quad (4.2)$$

where, c_1 and c_2 are the constants depending only on the size of the problem, $\|u\|_{L_2}$ and $\|u\| = (\boldsymbol{\Omega} \cdot \nabla u, G\boldsymbol{\Omega} \cdot \nabla u) + (u, Cu)$ denote the L_2 and energy norm, respectively. Figure 4.1 illustrates the general trend between the numerical error and the mesh size.

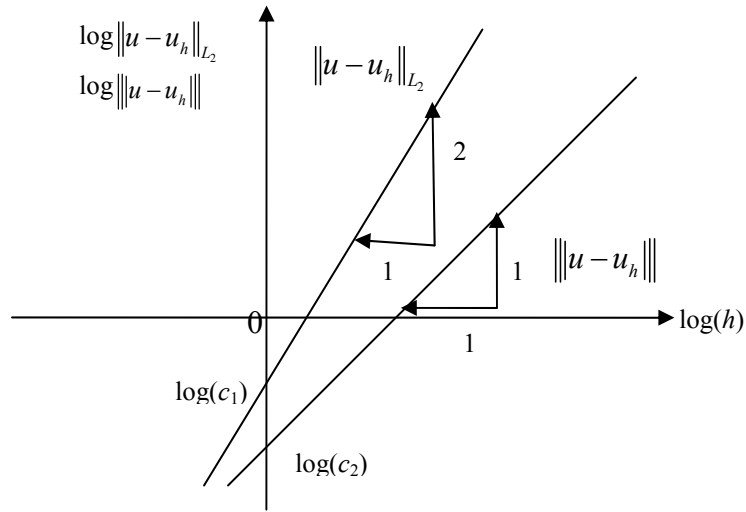


Figure 4.1: Illustration of relationship between numerical error and mesh size

A priori error estimates are difficult to use in practice due to the presence of the unknown constant. Desirable error indicators should be able to estimate error bounds only from known quantities, where *a posteriori* error estimates come into play. There are two main types of *a posteriori* error estimates: (gradient) recovery-based and residual-based. The philosophy behind the (gradient) recovery-based *a posteriori* error analysis is to project the gradient of the solution onto the higher order finite element space, and identify the error by comparing two gradients. On the other hand, the residual-based *a posteriori* error estimate uses the finite element residual of the problem to identify the

discretization error. The next section discusses the residual-based *a posteriori* error analysis applied to the FE- P_N methodology, and derives error bounds based on the L_2 norm and the energy norm.

4.2 Residual-Based *a Posteriori* Error Analysis

Our *a posteriori* error analysis is based on the weak formulation of the problem. The weak form of the even-parity transport equation is equivalent to the quadratic variational principle (3.4). The even-parity variational principle developed in the previous chapter can be split into two functionals:

$$K[\psi] = F[\psi, \psi] - 2F_s[\psi] \quad (4.3)$$

where,

$$F[\phi, \psi] = (\boldsymbol{\Omega} \cdot \nabla \phi, G \boldsymbol{\Omega} \cdot \nabla \psi) + (\phi, C\psi) + \langle \phi, \psi \rangle \quad (4.4)$$

$$F_s[\phi] = (\phi, S^+) + \langle \phi, T \rangle + (\boldsymbol{\Omega} \cdot \nabla \phi, GS^-) \quad (4.5)$$

The FE- P_N method then seeks the solution $\psi_{h,N} \in V_h x P_N$ such that:

$$F(\phi_{h,N}, \psi_{h,N}) = F_s(\phi_{h,N}) \text{ for all } \phi_{h,N} \in V_h x P_N \quad (4.6)$$

where, $\psi_{h,N}$ and $\phi_{h,N}$ are the trial and basis functions. V_h and P_N denote the spatial finite element space and the angular expansion spaces, respectively. Eq. (4.6) minimizes the even-parity extremum variational principle (3.4) for given set of basis functions. Hence, this finite element formulation results in the same discretized equations as the Ritz-Galerkin procedure.

4.2.1 A L_2 Norm *A Posteriori* Error Estimator

In order to characterize the discretization error in L_2 norm, we employ the dual problem. The dual problem of Eq. (4.6) can be expressed as:

$$F^*(z, w) = L(w) \quad (4.7)$$

where, z and w are the solution and basis functions of the dual problem, respectively. Since Eq. (4.4) is self-adjoint, $F^*(. , .) = F(. , .)$. It is a common practice to exploit the adjoint source term to characterize the desired quantity. Suppose we are interested in characterizing the discretization error in the L_2 norm. If we choose an arbitrary adjoint source term $L(w)$ to be the even-parity angular flux discretization error in the forward problem $e_{h,N} = \psi - \psi_{h,N}$, then the adjoint source term can be expressed as:

$$L(w) = \int_{4\pi} d\Omega \int_V dV e_{h,N} w \quad (4.8)$$

The L_2 error norm can then be expressed by substituting the discretization error into the adjoint basis function:

$$\|\psi - \psi_{h,N}\|_{L_2(V \times \Omega)}^2 = L(\psi - \psi_{h,N}) \quad (4.9)$$

Utilizing the Galerkin orthogonality,

$$F(\phi_{h,N}, \psi - \psi_{h,N}) = 0 \text{ for all } \phi_{h,N} \in V_h \chi P_N \quad (4.10)$$

and self-adjointness of Eq. (4.4), the error in the FE- P_N approximation can be written as the following form:

$$\begin{aligned} \|\psi - \psi_{h,N}\|_{L_2(V \times \Omega)}^2 &= L(\psi - \psi_{h,N}) \\ &= F^*(z, \psi - \psi_{h,N}) \\ &= F^*(z, \psi - \psi_{h,N}) - F^*(z_{h,N}, \psi - \psi_{h,N}) \\ &= F(\psi, z - z_{h,N}) - F(\psi_{h,N}, z - z_{h,N}) \\ &= F_s(z - z_{h,N}) - F(\psi_{h,N}, z - z_{h,N}) \end{aligned} \quad (4.11)$$

Note that the error in the even-parity flux of the FE- P_N approximation is expressed only in terms of the discretization error of the adjoint problem ($\varepsilon_{h,N} = z - z_{h,N}$) and the FE- P_N solution. Clearly, it is impractical to use Eq. (4.11) directly since obtaining the solution and error of the adjoint problem requires the same computational effort as obtaining the forward solution. The philosophy behind *a posteriori* error estimation is to restate the LHS of Eq. (4.11) by only using the known quantities such as the finite

element approximation and the mesh size. To eliminate the unknown adjoint solution terms from the expression, first Eq. (4.11) is rewritten as a sum of integrals over elements:

$$\begin{aligned}
\|\psi - \psi_{h,N}\|_{L_2(V;\chi\Omega)}^2 &= F_s(z - z_{h,N}) - F(\psi_{h,N}, z - z_{h,N}) \\
&= \sum_E \int_{V_E} dV \int_{4\pi} d\Omega \left[S^+(z - z_{h,N}) + \boldsymbol{\Omega} \cdot \nabla(z - z_{h,N}) G S^- \right. \\
&\quad \left. - \boldsymbol{\Omega} \cdot \nabla \psi_{h,N} G \boldsymbol{\Omega} \cdot \nabla(z - z_{h,N}) - \psi_h C(z - z_{h,N}) \right] \\
&\quad + \int_{\Gamma} d\Gamma \int_{4\pi} d\Omega |\boldsymbol{\Omega} \cdot \mathbf{n}| (T - \psi_{h,N})(z - z_{h,N})
\end{aligned} \tag{4.12}$$

Applying the chain rule,

$$\begin{aligned}
\boldsymbol{\Omega} \cdot \nabla G(fg) &= \boldsymbol{\Omega} \cdot \nabla [fGg + gGf] \\
&= f \boldsymbol{\Omega} \cdot \nabla Gg + (\boldsymbol{\Omega} \cdot \nabla f)(Gg) + \boldsymbol{\Omega} \cdot \nabla [gGf]
\end{aligned} \tag{4.13}$$

$$\begin{aligned}
(\boldsymbol{\Omega} \cdot \nabla f)(Gg) &= -f \boldsymbol{\Omega} \cdot \nabla Gg + \boldsymbol{\Omega} \cdot \nabla G(fg) - \boldsymbol{\Omega} \cdot \nabla [gGf] \\
&= -f \boldsymbol{\Omega} \cdot \nabla Gg + \boldsymbol{\Omega} \cdot \nabla [fGg]
\end{aligned} \tag{4.13'}$$

and Green's theorem,

$$\int_V dV \int_{4\pi} d\Omega \boldsymbol{\Omega} \cdot \nabla [fGg] = \int_{\partial V} d\Gamma \int_{4\pi} d\Omega (\boldsymbol{\Omega} \cdot \mathbf{n}) fGg \tag{4.14}$$

to Eq. (4.12) gives:

$$\begin{aligned}
\|\psi - \psi_{h,N}\|_{L_2(V;\chi\Omega)}^2 &= F_s(z - z_{h,N}) - F(\psi_{h,N}, z - z_{h,N}) \\
&= \sum_E \int_{V_E} dV \int_{4\pi} d\Omega (S^+ - \boldsymbol{\Omega} \cdot \nabla G S^- + \boldsymbol{\Omega} \cdot \nabla G \boldsymbol{\Omega} \cdot \nabla \psi_{h,N} - C \psi_{h,N})(z - z_{h,N}) \\
&\quad + \sum_E \int_{\partial V_E \setminus \Gamma} d\Gamma \int_{4\pi} d\Omega (\boldsymbol{\Omega} \cdot \mathbf{n})(z - z_{h,N})(G \boldsymbol{\Omega} \cdot \nabla \psi_{h,N}) \\
&\quad + \int_{\Gamma} d\Gamma \int_{4\pi} d\Omega |\boldsymbol{\Omega} \cdot \mathbf{n}| (z - z_{h,N})(T - \psi_{h,N} + G \boldsymbol{\Omega} \cdot \nabla \psi_{h,N}) \\
&= \sum_E \int_{V_E} dV \int_{4\pi} d\Omega R(\psi_{h,N})(z - z_{h,N}) \\
&\quad + \sum_{\gamma \in \partial V_E \setminus \Gamma} \int_{\gamma} d\Gamma \int_{4\pi} d\Omega (z - z_{h,N}) [G \boldsymbol{\Omega} \cdot \nabla \psi_{h,N}]_{\gamma} \\
&\quad + \int_{\Gamma} d\Gamma \int_{4\pi} d\Omega |\boldsymbol{\Omega} \cdot \mathbf{n}| (z - z_{h,N})(T - \psi_{h,N} + G \boldsymbol{\Omega} \cdot \nabla \psi_{h,N})
\end{aligned} \tag{4.15}$$

where, $R(\psi_{h,N}) = S^+ - \boldsymbol{\Omega} \cdot \nabla G S^- + \boldsymbol{\Omega} \cdot \nabla G \boldsymbol{\Omega} \cdot \nabla \psi_{h,N} - C \psi_{h,N}$ is the finite element residual,

and

$$\left[G \boldsymbol{\Omega} \cdot \nabla \psi_{h,N} \right]_{\gamma} = (\mathbf{n}_I \cdot \boldsymbol{\Omega}) G \boldsymbol{\Omega} \cdot \nabla \psi_{h,N} \Big|_I + (\mathbf{n}_J \cdot \boldsymbol{\Omega}) G \boldsymbol{\Omega} \cdot \nabla \psi_{h,N} \Big|_J$$

is the discontinuity in the odd-parity flux along the element edge γ which separates the elements I and J .

Note that the interior surface integral is calculated twice during the sweeping the elements. If the surface residual term is defined as:

$$R_{\gamma}(\psi_{h,N}) = -\frac{1}{2} \left[G \boldsymbol{\Omega} \cdot \nabla \psi_{h,N} \right]_{\gamma} \text{ on } \gamma \in \partial V_E \setminus \Gamma \quad (4.16)$$

$$R_{\gamma}(\psi_{h,N}) = (\boldsymbol{\Omega} \cdot \mathbf{n}) (T - \psi_{h,N} + G \boldsymbol{\Omega} \cdot \nabla \psi_{h,N}) \text{ on } \gamma \in \Gamma \quad (4.17)$$

Eq. (4.15) may then be simplified to:

$$\begin{aligned} \|\psi - \psi_{h,N}\|_{L_2(V_{\mathbb{X}\Omega})}^2 &= \sum_E \int_{V_E} dV \int_{4\pi} d\Omega (z - z_{h,N}) R(\psi_{h,N}) \\ &\quad + \sum_{\gamma \in \partial V_E} \int_{\gamma} d\Gamma \int_{4\pi} d\Omega (z - z_{h,N}) R_{\gamma}(\psi_{h,N}) \end{aligned} \quad (4.18)$$

Clear physical meaning can be observed in Eq. (4.18). $R(\psi_{h,N})$ measures the local particle conservation property within the volume element, whereas $R_{\gamma}(\psi_{h,N})$ can be thought as the discontinuity in the current along the element edges. The transport problem, in theory, conserves the particle balance and interface continuity. The (continuous) FE-P_N method conserves the particle conservation globally, but not locally. In order to conserve the global particle balance, the FE-P_N discretization introduces an artificial surface source and sink. Clearly, this artifact is the source of the discretization errors. Applying the Cauchy-Schwarz inequality in Eq. (4.18) gives:

$$\begin{aligned} \|\psi - \psi_{h,N}\|_{L_2(V_{\mathbb{X}\Omega})}^2 &\leq \sum_E \left\| h_E^2 R(\psi_{h,N}) \right\|_{L_2(E_{\mathbb{X}\Omega})} \left\| h_E^{-2} (z - z_{h,N}) \right\|_{L_2(E_{\mathbb{X}\Omega})} \\ &\quad + \sum_E \left\| h_E^{3/2} R_{\gamma}(\psi_{h,N}) \right\|_{L_2(\partial E_{\mathbb{X}\Omega})} \left\| h_E^{-3/2} (z - z_{h,N}) \right\|_{L_2(\partial E_{\mathbb{X}\Omega})} \end{aligned} \quad (4.19)$$

where, h_E is the mesh size for the element E . The parameter h_E is introduced in Eq. (4.19) for the later derivation which bounds the interpolation error by the semi-norm. To eliminate the norm in the adjoint error term, we make a few assumptions. The first assumption is that the solution of the adjoint problem is a square integrable function and equipped with the following semi-norm:

$$|z|_{H^2(E\Omega)} = \left[\int_{4\pi} d\Omega \int_E dV |(\boldsymbol{\Omega} \cdot \nabla)^2 z|^2 \right]^{1/2} < \infty \quad (4.20)$$

Subscript H^2 indicates that the function in this space is twice differentiable in the direction of the particle travel. Then, the L_2 norm error of the adjoint problem is bounded by [46]:

$$\|z - \pi_h z\|_{L_2(E\Omega)} \leq ch_E^2 |z|_{H^2(E\Omega)} \quad (4.21)$$

and

$$\|z - \pi_h z\|_{L_2(\partial E\Omega)} \leq ch_E^{3/2} |z|_{H^2(E\Omega)} \quad (4.22)$$

where π_h is the interpolation operator and c is the constant independent of element size h_E . The interpolation operator π_h is the Lagrange interpolation, which can be defined as:

$$\pi_h z(x_i) = z(x_i) \quad (4.23)$$

where x_i is the Lagrange interpolation node. Then the error in the finite element approximation is bounded from above by the Lagrange interpolation because of the minimization property of the finite element:

$$\|z - z_{h,N}\|_{L_2(E\Omega)} \leq \|z - \pi_h z\|_{L_2(E\Omega)} \quad (4.24)$$

Inequalities (4.21) and (4.22) may be formulated by applying the Cauchy-Schwartz inequality and recognizing the fact that the second derivative of the finite element solution identically vanishes in the linear case. Secondly, the following inequality is assumed to hold:

$$|z|_{H^2(E\Omega)} \leq c \|\psi - \psi_h\|_{L_2(E\Omega)} \quad (4.25)$$

Eq. (4.25) states the regularity and smoothness of the problem. Using equation (4.19)-(4.25), the error in the L_2 norm of the angular flux of P_N approximation can be expressed as:

$$\|\psi - \psi_{h,N}\|_{L_2(Ex\Omega)} \leq c \sum_E \left(\|h_E^2 R(\psi_{h,N})\|_{L_2(Ex\Omega)} + \frac{1}{2} \|h_K^{3/2} R_\gamma(\psi_{h,N})\|_{L_2(\partial Ex\Omega)} \right) \quad (4.26)$$

Thus, we can define the local error indicator (η_E) and global error indicator as follows:

$$\eta_E^2 = h_E^4 \|R(\psi_{h,N})\|_{L_2(Ex\Omega)}^2 + \frac{h_E^3}{2} \|R_\gamma(\psi_{h,N})\|_{L_2(\partial Ex\Omega)}^2 \quad (4.27)$$

$$\eta^2 = \sum_E \eta_E^2 \quad (4.28)$$

4.2.2 An Energy Norm *A Posteriori* Error Estimator

A similar, but simpler, argument can be applied to derive *a posteriori* error estimator based on the energy norm. The discretization error can be described by using the following weak formulation:

$$F(\phi, e_{h,N}) = F_s(\phi) - F(\phi, \psi_{h,N}) \quad (4.29)$$

Explicitly writing out the RHS of Eq. (4.29) gives:

$$\begin{aligned} F_s(\phi) - F(\phi, \psi_{h,N}) &= \int_V dV \int_{4\pi} d\Omega \left[S^+ \phi + \boldsymbol{\Omega} \cdot \nabla \phi G S^- - \boldsymbol{\Omega} \cdot \nabla \psi_{h,N} G \boldsymbol{\Omega} \cdot \nabla \phi - \psi_{h,N} C \phi \right] \\ &\quad + \int_\Gamma d\Gamma \int_{4\pi} d\Omega |\boldsymbol{\Omega} \cdot \mathbf{n}| (T - \psi_{h,N}) \phi \end{aligned} \quad (4.30)$$

Applying the chain rule (4.13) and the Green's theorem (4.14) to obtain the expression:

$$\begin{aligned}
F_s(\phi) - F(\phi, \psi_{h,N}) &= \sum_E \int_{V_E} dV \int_{4\pi} d\Omega \left(S^+ - \boldsymbol{\Omega} \cdot \nabla G S^- + \boldsymbol{\Omega} \cdot \nabla G \boldsymbol{\Omega} \cdot \nabla \psi_{h,N} - C \psi_{h,N} \right) \phi \\
&\quad + \sum_E \int_{\partial V_E \setminus \Gamma} d\Gamma \int_{4\pi} d\Omega |\boldsymbol{\Omega} \cdot \mathbf{n}| \phi \left(G \boldsymbol{\Omega} \cdot \nabla \psi_{h,N} \right) \\
&\quad + \int_{\Gamma} d\Gamma \int_{4\pi} d\Omega |\boldsymbol{\Omega} \cdot \mathbf{n}| \phi \left(T - \psi_{h,N} + G \boldsymbol{\Omega} \cdot \nabla \psi_{h,N} \right) \\
&= \sum_E \int_{V_E} dV \int_{4\pi} d\Omega \phi R(\psi_{h,N}) \\
&\quad + \sum_{\gamma \in \partial V_E} \int_{\gamma} d\Gamma \int_{4\pi} d\Omega \phi R_\gamma(\psi_{h,N})
\end{aligned} \tag{4.31}$$

Utilizing the Galerkin orthogonality:

$$F(\phi_{h,N}, \psi - \psi_{h,N}) = 0 \tag{4.32}$$

and applying the Cauchy-Schwarz inequality gives:

$$\begin{aligned}
F(\phi, e_{h,N}) &= \sum_E \int_{V_E} dV \int_{4\pi} d\Omega (\phi - \phi_{h,N}) R(\psi_{h,N}) + \sum_{\gamma \in \partial V_E} \int_{\gamma} d\Gamma \int_{4\pi} d\Omega (\phi - \phi_{h,N}) R_\gamma(\psi_{h,N}) \\
&\leq \sum_E \left\| (\phi - \phi_{h,N}) \right\|_{L_2(E \times \Omega)} \left\| R(\psi_{h,N}) \right\|_{L_2(E \times \Omega)} \\
&\quad + \sum_{\gamma \in \partial V_E} \left\| (\phi - \phi_{h,N}) \right\|_{L_2(\partial E \times \Omega)} \left\| R_\gamma(\psi_{h,N}) \right\|_{L_2(\partial E \times \Omega)}
\end{aligned} \tag{4.33}$$

assuming that the following Clement type interpolation [46]

$$\left\| \phi - \pi_h \phi \right\|_{L_2(E \times \Omega)} \leq C h_E |\phi|_{H^1(E \times \Omega)} \tag{4.34}$$

and

$$\left\| \phi - \pi_h \phi \right\|_{L_2(\partial E \times \Omega)} \leq C h_E^{1/2} |\phi|_{H^1(E \times \Omega)} \tag{4.35}$$

applies to the problem. The semi-norm $|\phi|_{H^1(E \times \Omega)}$ is now defined as

$$|\phi|_{H^1(E \times \Omega)} = \left[\int_{4\pi} d\Omega \int_E dV |(\boldsymbol{\Omega} \cdot \nabla) \phi|^2 \right]^{1/2} \tag{4.36}$$

The explicit expression of the energy norm is:

$$\|\phi\| = \sqrt{(\boldsymbol{\Omega} \cdot \nabla \phi, G \boldsymbol{\Omega} \cdot \nabla \phi) + (\phi, C \phi)} \tag{4.37}$$

Due to positive definiteness of the operators G and C , we immediately see:

$$(\boldsymbol{\Omega} \cdot \nabla \phi, G \boldsymbol{\Omega} \cdot \nabla \phi) \leq \|\phi\|^2 \quad (4.38)$$

Writing the operator G explicitly, we get:

$$(\boldsymbol{\Omega} \cdot \nabla \phi, G \boldsymbol{\Omega} \cdot \nabla \phi) = \int dV \int d\boldsymbol{\Omega} \boldsymbol{\Omega} \cdot \nabla \phi \sum_{l=1}^{odd} \frac{2l+1}{4\pi} \frac{1}{\sigma_l} \int d\boldsymbol{\Omega}' P_l(\mu_0) \boldsymbol{\Omega}' \cdot \nabla \phi \quad (4.39)$$

Similarly, we can write the semi-norm (4.36) as:

$$(\boldsymbol{\Omega} \cdot \nabla \phi, \boldsymbol{\Omega} \cdot \nabla \phi) = \int dV \int d\boldsymbol{\Omega} \boldsymbol{\Omega} \cdot \nabla \phi \sum_{l=0}^{\infty} \frac{2l+1}{4\pi} \int d\boldsymbol{\Omega}' P_l(\mu_0) \boldsymbol{\Omega}' \cdot \nabla \phi \quad (4.40)$$

Now let us denote the maximum cross section as σ_{max}

$$\sigma_{max} = \max(\sigma_l), \quad l=1, L, \text{ odd} \quad (4.41)$$

where, L is the number of moments in scattering cross section. In the case of isotropic scattering, $\sigma_{max} = \sigma_l$. Then we can obtain the lower bound of (4.39) as:

$$\frac{1}{\sigma_{max}} (\boldsymbol{\Omega} \cdot \nabla \phi, \boldsymbol{\Omega} \cdot \nabla \phi) \leq (\boldsymbol{\Omega} \cdot \nabla \phi, G \boldsymbol{\Omega} \cdot \nabla \phi) \quad (4.42)$$

Finally, we can bound the semi-norm in terms of the energy norm as follows:

and we recognize the fact that the energy norm is greater than the semi-norm (4.36):

$$\|\phi\|_{H^1(Ex\Omega)} \leq \sqrt{\sigma_{max}} \|\phi\| \quad (4.43)$$

Finally substituting the discretization error $e_{h,N}$ into the basis function ϕ , we obtain the

energy norm expression:

$$F(e_{h,N}, e_{h,N}) = \|e_{h,N}\|^2 \leq \sqrt{\sigma_{max}} \|e_{h,N}\| \left\{ \sum_E h_E^2 \|R(\psi_{h,N})\|_{L_2(Ex\Omega)}^2 + \sum_{\gamma \in \partial V_E} h_E \|R_\gamma(\psi_{h,N})\|_{L_2(\partial Ex\Omega)}^2 \right\}^{1/2} \quad (4.44)$$

Thus, we can define *a posteriori* error estimator based on the energy norm to be:

$$\eta_E^2 = \sigma_{max} \left(h_E^2 \|R(\psi_{h,N})\|_{L_2(Ex\Omega)}^2 + h_E \|R_\gamma(\psi_{h,N})\|_{L_2(\partial Ex\Omega)}^2 \right) \quad (4.45)$$

4.3 Separation of the Error Components

In the previous section, we have derived *a posteriori* error estimators based on the global L_2 and energy norms that are dependent on both spatial and angular discretizations. In order to apply *a posteriori* error estimates in the context of adaptivity, the error indicator must distinguish the error components of each independent variable. First, we expand the L_2 error norm in terms of spherical harmonics:

$$\begin{aligned} \|\psi - \psi_{h,N}\|_{L_2(V;\Omega)} &= \left\| \sum_{l,m}^N Y_{l,m}(\Omega) [\psi^{l,m}(\mathbf{r}) - \psi_{h,N}^{l,m}(\mathbf{r})] + \sum_{l,m=N+2}^{\infty} Y_{l,m}(\Omega) \psi^{l,m}(\mathbf{r}) \right\|_{L_2(V;\Omega)} \\ &= \left\{ \int_V dV \sum_{l,m=0}^{N,\text{even}} \frac{1}{2} (1 + \delta_{m,0}) [e^{l,m}(\mathbf{r})]^2 + \sum_{l,m=N+2}^{\infty,\text{even}} \frac{1}{2} (1 + \delta_{m,0}) (\psi^{l,m}(\mathbf{r}))^2 \right\}^{1/2} \end{aligned} \quad (4.46)$$

where $e^{lm}(\mathbf{r})$ is the error in l -th and m -th spherical harmonic moment at position \mathbf{r} . The second term represents the angular truncation error. The last line of Eq. (4.46) is obtained by utilizing the orthogonality relationship of the spherical harmonics. The term $e^{lm}(\mathbf{r})$ includes both spatial and angular discretization errors up to P_N ; therefore, it does not provide useful information whether the element requires spatial or angular refinement. In order to obtain a more useful expression for the adaptivity, we compare the FE- P_N solution with the spatially continuous P_N solution:

$$\begin{aligned} \|\psi_N - \psi_{h,N}\|_{L_2(V;\Omega)} &= \left\| \sum_{l,m}^N Y_{l,m}(\Omega) [\psi^{l,m}(\mathbf{r}) - \psi_{h,N}^{l,m}(\mathbf{r})] \right\|_{L_2(V;\Omega)} \\ &= \left\{ \int_V dV \sum_{l,m=0}^{N,\text{even}} \frac{1}{2} (1 + \delta_{m,0}) [\tilde{e}^{l,m}(\mathbf{r})]^2 \right\}^{1/2} \end{aligned} \quad (4.47)$$

where $\tilde{e}^{l,m}(\mathbf{r})$ is the l,m -th spherical harmonics moment spatial discretization error of the P_N approximation. Note that the Eq. (4.47) contains only the spatial discretization error of FE- P_N approximation. The spatial discretization error in P_N approximation can be approximated by substituting Eq. (4.47) into the RHS of Eq. (4.26). In this case, the finite element residual term $R_N(\psi_{h,N})$ is computed by the following:

$$R_N(\psi_{h,N}) = \int_{4\pi} d\Omega' \sum_{l=0}^{N, \text{even}} \frac{2l+1}{4\pi} P_l(\mu_0) (S^+ + \boldsymbol{\Omega}' \cdot \nabla G \boldsymbol{\Omega}' \cdot \nabla \psi_{h,N}^+ - C\psi_{h,N}^+) \quad (4.48)$$

Eq. (4.48) is substituted to estimate the spatial discretization error of P_N approximation.

The angular truncation error of the P_N approximation is then found by projecting the spatially converged solution onto the higher order angular space (i.e. P_{N+2} space). In theory, if the finite element residual term in Eq. (4.26) is replaced by $R_{N+2}(\psi_{h,N})$, we can estimate the angular truncation error. However, because the explicit error estimator heavily depends on the mesh size, it is not suitable for estimating the angular truncation error. In the next section we shall discuss the specific strategy to estimate the angular truncation error by an implicit error estimator.

4.4 Treatment of the Angular Variables

4.4.1 Implicit Error Estimator for the Angular Variables

Once spatial convergence is achieved, the angular truncation error can be estimated using $R_{N+2}(\psi_h)$ as the FE residual term in Eq. (4.26). Higher-order spherical harmonic moments are then added to the angularly non-converged elements. In theory, this approach gives the strategy to refine the angular variable. There is a difficulty, however, using Eq. (4.26) as the error indicator for the angular variable. Since the required angular order is dependent solely on the physical problem, not on the spatial discretization, the desirable angular error indicator should be independent of the mesh size. Eq. (4.26) strongly depends on the mesh size and, therefore, it is not the best error indicator. In this sub-section, we introduce an alternate approach in which the error indicator does not depend on the mesh size. The approach is called an implicit error estimator, as opposed to an explicit estimator derived in the previous section, due to its use of solution of the element-wise matrix equation.

To formulate an efficient implicit error estimator, we make use of the hierarchical property of the spherical harmonics functions. Taking into account the smoothness of the finite element approximation on the element interior, the error in even-parity flux may be written as:

$$-\mathbf{\Omega} \cdot \nabla G \mathbf{\Omega} \cdot \nabla e_{h,N} + C e_{h,N} = S^+ + \mathbf{\Omega} \cdot \nabla G \mathbf{\Omega} \cdot \nabla \psi_{h,N} - C \psi_{h,N} \quad (4.49)$$

The corresponding natural boundary condition may be written as:

$$(\mathbf{n} \cdot \mathbf{\Omega}) G (\mathbf{\Omega} \cdot \nabla e_{h,N}) = (\mathbf{n} \cdot \mathbf{\Omega}) (G \mathbf{\Omega} \cdot \nabla \psi - G \mathbf{\Omega} \cdot \nabla \psi_{h,N}) \quad (4.50)$$

Clearly, imposing an appropriate boundary condition Eq. (4.50) is not possible due to the unknown term ψ . However, it is possible to approximate the gradient term by the finite element approximation:

$$\begin{aligned} (\mathbf{n} \cdot \mathbf{\Omega}) G (\mathbf{\Omega} \cdot \nabla e_{h,N}) &\approx \frac{1}{2} (\mathbf{n} \cdot \mathbf{\Omega}) (G \mathbf{\Omega} \cdot \nabla \psi_{h,N} \Big|_R + G \mathbf{\Omega} \cdot \nabla \psi_{h,N} \Big|_L) \\ &= (\mathbf{n} \cdot \mathbf{\Omega}) \langle G \mathbf{\Omega} \cdot \nabla \psi_{h,N} \rangle \end{aligned} \quad (4.51)$$

Now the weak formulation of the local element residual problem can be written as the following boundary value problem:

$$\begin{aligned} F(\phi, e_{h,N}) &= F(\phi, \psi) - F(\phi, \psi_{h,N}) \\ &= F_s(\phi) - F(\phi, \psi_{h,N}) \\ &= \int_{4\pi} d\Omega \int_V dV \phi R(\psi_{h,N}) + \int_{4\pi} d\Omega \int_{\partial V} d\Gamma (\mathbf{n} \cdot \mathbf{\Omega}) \phi \langle G (\mathbf{\Omega} \cdot \nabla \psi_{h,N} - S^-) \rangle \end{aligned} \quad (4.52)$$

Eq. (4.52) is valid for any basis function ϕ . The error term can be estimated by solving the local finite element matrix with the Neumann boundary condition developed by Bank and Weiser [47]. To obtain the angular truncation error of P_N approximation, we simply place the $N+2^{\text{th}}$ order spherical harmonics functions as the basis function of Eq. (4.52) and solve the problem. Notice that the solution of Eq. (4.52) is independent of discretization and only depends on the angular expansion orders if the gradient term is well recovered by the averaging Eq. (4.51).

4.4.1.1 Reliability of the Implicit Estimator

In order for the residual equation (4.29) to produce the exact error, an infinite dimensional space is required. Clearly, it is impossible to use such a space; hence we must approximate the error in the smaller discretized space, and hope that the estimated error mimics the true error sufficiently close. In order to estimate the angular truncation errors in the P_N approximation, we have decided to use the P_{N+2} th order of spherical harmonics basis function. Since we implicitly assume that the solution changes only slightly with the addition of the higher order angular basis, we hope that the minor change can be approximated by the localized subspace. The following discusses the validity of the developed implicit estimators. The hierarchical property of the spherical harmonics basis function allows us to analyze the implicit error estimator using the methodology introduced by Bank and Smith [47].

First, we recognize that any function ψ_{N+2} that lies on the space $P_{N+2} = P_N \oplus \tilde{P}_{N+2}$ can be decomposed with two components:

$$\psi_{N+2} = \psi_N + \varphi_{N+2} \quad (4.53)$$

where, $\psi_N \in P_N$, and $\varphi_{N+2} \in \tilde{P}_{N+2}$. We then make an assumption that the following “saturation assumption” holds:

$$\|\psi - \psi_{h,N+2}\| \leq \beta \|\psi - \psi_{h,N}\| \quad (4.54)$$

where $\beta < 1$. Eq. (4.54) simply states that the higher-order angular approximation converges to the exact solution more rapidly than the lower-order approximations. Then we apply the Galerkin orthogonality to form following equality:

$$\|\psi - \psi_{h,N}\|^2 = \|\psi - \psi_{h,N+2}\|^2 + \|\psi_{h,N+2} - \psi_{h,N}\|^2 \quad (4.55)$$

Due to the Galerkin orthogonality, the error components are orthogonal with respect to the energy norm. Incorporating with (4.54), Eq. (4.55) can be modified as:

$$(1 - \beta^2) \|\psi - \psi_{h,N}\|^2 \leq \|\psi_{h,N+2} - \psi_{h,N}\|^2 \leq \|\psi - \psi_{h,N}\|^2 \quad (4.56)$$

Therefore, the reliability of the error indicator calculated from the P_{N+2} space depends on the difference in the convergence rates between the P_N and P_{N+2} approximations.

Because the lower bound behaves quadratically in β , we expect that it is relatively close to the true solution. Our error estimator uses further simplified angular basis functions.

In order to derive the bound, we assume a strengthened Cauchy-Schwarz inequality [47]:

$$|F[\varphi_N, \varphi_{N+2}]| \leq \gamma \|\varphi_N\| \|\varphi_{N+2}\| \quad (4.57)$$

The term is $\gamma < 1$ and it can be seen as the generalized cosine angle between the P_N and \tilde{P}_{N+2} with respect to the energy norm. By utilizing Eq. (4.57), one can write the following error bounds:

$$(1 - \beta^2)(1 - \gamma^2) \|\psi - \psi_{h,N}\|^2 \leq \|e_{h,N+2}\|^2 \leq \|\psi - \psi_{h,N}\|^2 \quad (4.58)$$

where, $e_{h,N+2}$ is the solution of the residual equation (4.52) with the basis function being $\varphi_{N+2} \in \tilde{P}_{N+2}$. The lower bound of Eq. (4.58) can be obtained by combining Eq. (4.57) and the following Young's inequality:

$$ab \leq \frac{a^p}{p} + \frac{b^q}{q} \quad (4.59)$$

$$\frac{1}{p} + \frac{1}{q} = 1$$

Eq. (4.58) shows that the error estimates is smaller than the true error. On the other hand, the error estimate using local residual problem with a proper boundary condition is shown to overestimate the true error [11, 48]:

$$(1 - \beta^2)(1 - \gamma^2) \|\psi - \psi_{h,N}\|^2 \leq \|\tilde{\psi}_{h,N+2} - \psi_{h,N}\|^2 \leq \sum_E \|\tilde{e}_{h,N}\|_E^2 \quad (4.60)$$

where, $\tilde{e}_{h,N}$ is the solution of the local residual problem (4.52). We hope then that our error estimate is closer to the true error.

4.4.2 Surface Angular Integrals

Both the explicit and implicit error estimators involve the computation of volume and surface integrals over the element. The volume integrals are also used in the FE-P_N formulation; therefore, there is no need for the extra integral evaluations. Conversely, the surface integrals in Eq. (4.27), (4.45), and (4.52) involve the half-range angular integrals along all element edges, which do not appear in the FE-P_N formulations. The error estimators require the evaluation of the following integral:

$$\int_{4\pi} d\Omega (\boldsymbol{\Omega} \cdot \mathbf{n}) \phi(G \boldsymbol{\Omega} \cdot \nabla \psi_{h,N}) = 2 \int_{\boldsymbol{\Omega} \cdot \mathbf{n} < 0} d\Omega |\boldsymbol{\Omega} \cdot \mathbf{n}| \phi(G \boldsymbol{\Omega} \cdot \nabla \psi_{h,N}) \quad (4.61)$$

The surface integrals must be evaluated on each element edge, and the integrand contains the inner product between the direction $\boldsymbol{\Omega}$ and the normal vector to the surface \mathbf{n} . Thus, the surface integral depends on the orientations relative to the reference coordinate system. Moreover, the angular integral does not generally have an analytical expression since the integration limits of one variable are a function of the other angular variable [42]. The evaluation of the surface angular integral is, therefore, cumbersome and may become expensive.

This extra computational effort, however, can be greatly reduced if the surface normal is aligned along one of the reference coordinate system. In particular, the analytical expression of the angular integral exists when the surface normal vector is perpendicular to the x -axis (Figure 4.2). The integration limits then become independent of one another and have the following expression:

$$\int_{\boldsymbol{\Omega} \cdot \mathbf{n} < 0} d\Omega |\boldsymbol{\Omega} \cdot \mathbf{n}| \phi(G \boldsymbol{\Omega} \cdot \nabla \psi_{h,N}) = \int_0^\pi d\omega \int_{-1}^1 d\mu \sqrt{1-\mu^2} \phi(G \boldsymbol{\Omega} \cdot \nabla \psi_{h,N}) \quad (4.62)$$

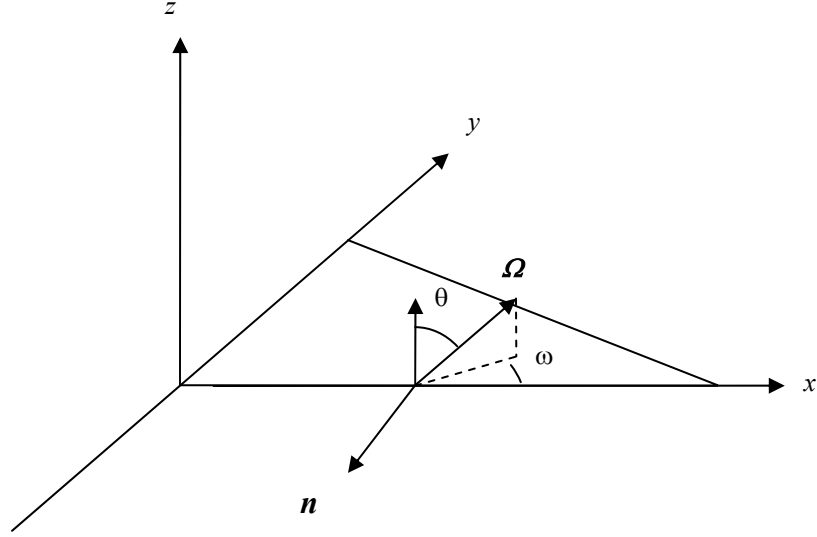


Figure 4.2: Illustration of angular coordinate relative to the element edge in the case of normal vector being parallel to the y-axis

In this case, the integral with respect to the variable μ can be evaluated by the following expression [42]:

$$\begin{aligned}
 \int_{-1}^1 d\mu \sqrt{1-\mu^2} P_l^m(\mu) P_l^{m'}(\mu) &= \frac{2(l+m+2)!}{(2l+1)(2l+3)(l-m)!} \delta_{l',l+1} \delta_{m',m+1} \\
 &= -\frac{2(l+m)!}{(2l+1)(2l-1)(l-m-2)!} \delta_{l',l-1} \delta_{m',m+1} \\
 &= \frac{2(l+m-1)!}{(2l+1)(2l-3)(l-m)!} \delta_{l',l-1} \delta_{m',m-1} \\
 &= -\frac{2(l+m)!}{(2l+1)(2l+3)(l-m)!} \delta_{l',l+1} \delta_{m',m-1}
 \end{aligned} \tag{4.63}$$

and the integral with the azimuthal angle ω becomes:

$$\int_0^\pi d\omega \sin \omega \begin{pmatrix} \sin m' \omega \\ \cos m' \omega \end{pmatrix} \begin{pmatrix} \sin m \omega & \cos m \omega \end{pmatrix} = \frac{\pi}{4-2\delta_{m,0}} \begin{pmatrix} 0 & \delta_{m',m+1} - \delta_{m',m-1} \\ \delta_{m',m-1} - \delta_{m',m+1} & 0 \end{pmatrix} \tag{4.64}$$

The angular integral of an arbitrarily oriented surface can be evaluated by the rotation of the coordinate system. For two-dimensional x - y geometry, there is no need for

the rotation of polar angle. The rotation of the azimuthal angle is defined such that the new x -axis is aligned to the element edge (Figure 4.3).

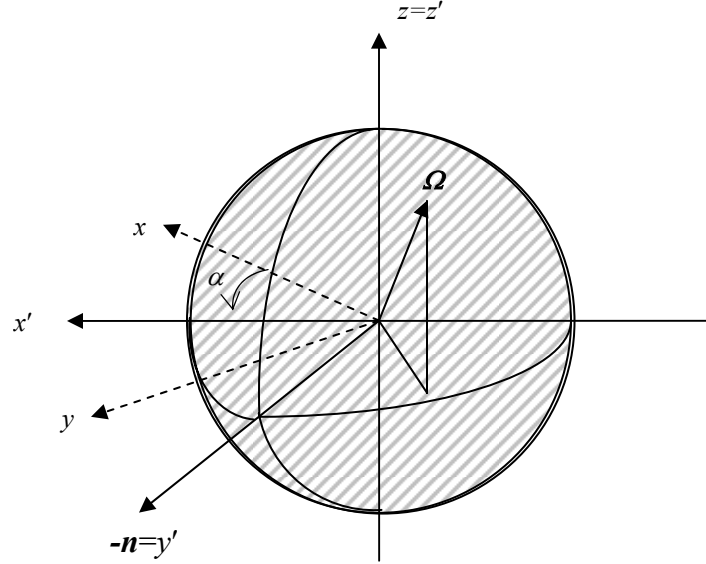


Figure 4.3: Illustration of the half-range surface integral in new coordinate system (x',y',z') . New coordinate system is rotated counter clockwise by angle α about z -axis

The following addition formulas of the sine and cosine functions are then utilized to evaluate the integral with respect to the original reference coordinate system:

$$\begin{aligned} \begin{bmatrix} \sin \omega' \\ \cos \omega' \end{bmatrix} &= \begin{bmatrix} \cos \alpha & \sin \alpha \\ -\sin \alpha & \cos \alpha \end{bmatrix} \begin{bmatrix} \sin \omega \\ \cos \omega \end{bmatrix} \\ &= \mathbf{R}(\alpha) \begin{bmatrix} \sin \omega \\ \cos \omega \end{bmatrix} \end{aligned} \quad (4.65)$$

and

$$\begin{aligned} \begin{bmatrix} \sin \omega \\ \cos \omega \end{bmatrix} &= \begin{bmatrix} \cos \alpha & -\sin \alpha \\ \sin \alpha & \cos \alpha \end{bmatrix} \begin{bmatrix} \sin \omega' \\ \cos \omega' \end{bmatrix} \\ &= \mathbf{R}^T(\alpha) \begin{bmatrix} \sin \omega' \\ \cos \omega' \end{bmatrix} \end{aligned} \quad (4.66)$$

where $\omega' = \omega + \alpha$ are the azimuthal angle in the new rotated system and $\mathbf{R}(\alpha)$ denotes the rotation matrix. Then, the surface integral with respect to the original coordinate system can be evaluated as:

$$\begin{aligned}
& \int_{\alpha}^{\alpha+\pi} d\omega \sin(\alpha + \omega) \begin{pmatrix} \sin m'\omega \\ \cos m'\omega \end{pmatrix} \begin{pmatrix} \sin m\omega & \cos m\omega \end{pmatrix} \\
&= \int_0^{\pi} d\omega' \sin\omega' \begin{bmatrix} \cos m'\alpha & -\sin m'\alpha \\ \sin m'\alpha & \cos m'\alpha \end{bmatrix} \begin{bmatrix} \sin m'\omega' \\ \cos m'\omega' \end{bmatrix} \begin{bmatrix} \sin m\omega' & \cos m\omega' \end{bmatrix} \begin{bmatrix} \cos m\alpha & \sin m\alpha \\ -\sin m\alpha & \cos m\alpha \end{bmatrix} \\
&= \mathbf{R}^T(m'\alpha) \left\{ \int_0^{\pi} d\omega' \sin\omega' \begin{bmatrix} \sin m'\omega' \\ \cos m'\omega' \end{bmatrix} \begin{bmatrix} \sin m\omega' & \cos m\omega' \end{bmatrix} \right\} \mathbf{R}(m\alpha)
\end{aligned} \tag{4.67}$$

Therefore, in order to evaluate the surface angular integrals, it suffices to calculate the rotation matrix, Eq. (4.63) and (4.64). Then, the original integral can be calculated by performing a double matrix product shown in Eq. (4.67).

4.5 Spatial Mesh Refinement Strategy in Two-Dimensional x - y Geometry

For each stage of the finite element calculation, the convergence of the spatial discretization is tested via the explicit error estimator. In this section, we discuss a local spatial mesh refinement strategy used on this thesis. We assume that the problem consists of the two-dimensional x - y geometry, and it is meshed with the triangular elements.

Let us denote the tolerance of the problem by TOL . Then, the adaptive refinement should terminate when *a posteriori* error estimate fulfills the following condition:

$$\eta \leq TOL \tag{4.68}$$

where η is the estimated global error defined by Eq. (4.28). Let us denote the number of elements in the current FE- P_N calculation by $NELM$. Further refinement for the element E is not required when the following condition is satisfied:

$$\eta_E^2 \leq \frac{TOL^2}{NELM} \tag{4.69}$$

It is easy to see that Eq. (4.68) is automatically fulfilled if Eq. (4.69) is satisfied for all the elements. When the local error is large, the element is subdivided into smaller elements. Two simple subdivision schemes can be: (a) cell-based subdivision, and (b) edge-based subdivision. Figure 4.4 illustrates both subdivision schemes.

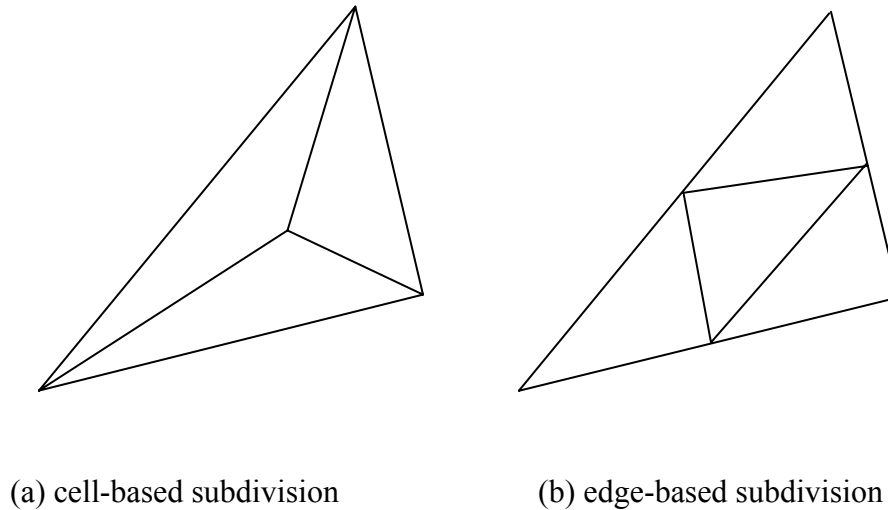


Figure 4.4: Element refinement strategy

It is clear that the cell-based subdivision is simpler refinement strategy than the edge-based subdivision. Main advantages of the cell-based methods are:

- (i) only one new nodal point is required for refined elements, and
- (ii) no hanging nodes are created.

However, the cell-based methods are difficult to keep the aspect ratio close to a unity. Therefore, the accuracy of the adaptive refinement may deteriorate due to the heavily skewed elements.

On the other hand, the edge-based refinement strategy produces the three additional nodal points on the element edges. Thus, the strategy produces the hanging nodes, which do not have proper finite element connections, when the adjacent element

does not require a further refinement. However, one of the advantages using the edge-based refinement is that the each local refinement creates the four similar triangles to the original element if the edges are bisected; therefore, the computations of the integrals, which are the main process of the finite element setup, can be greatly simplified, and storage requirement reduced. For this reason, we employ the edge-based refinement strategy for the spatial mesh refinement.

Unrefined elements possibly have one or two hanging nodes when the adjacent elements are selected for the refinement. There are two refinement possibilities for the elements with two hanging nodes. Let us assume that edges 1 and 2 are marked for the bisection in the element E . Then, the element E can generate three elements shown in Figure 4.5.

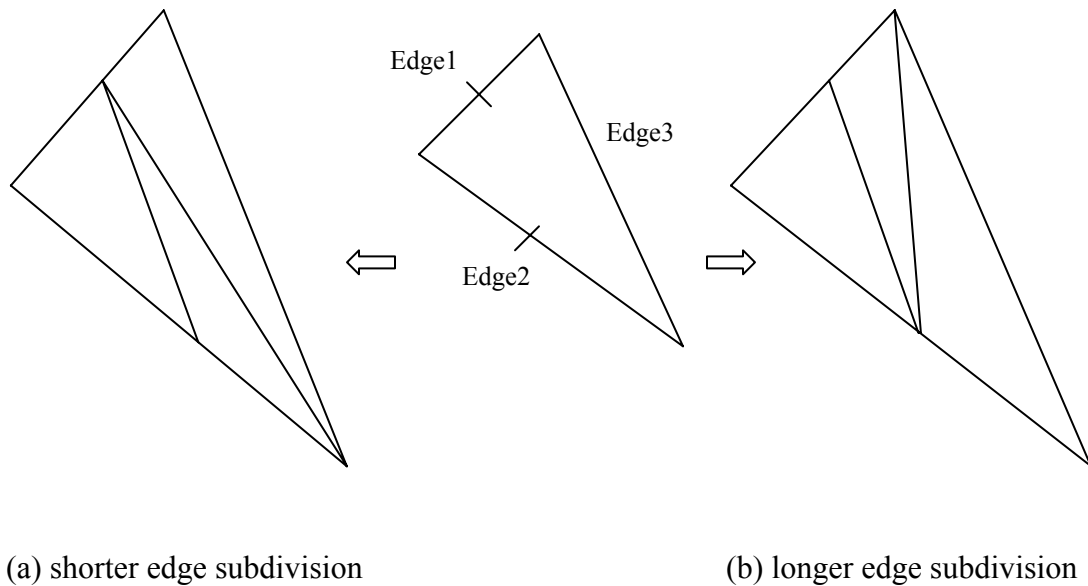


Figure 4.5: Two different subdivisions for element with two hanging nodes

It is clear that the resulting elements with the longer edge subdivision (Figure 4.5(b)) have better element qualities. Therefore, we employ the longer edge subdivision scheme

for the element with the two hanging nodes. For the element with the one hanging node, we can simply connect the new nodes to the one on the opposite side (Figure 4.6).

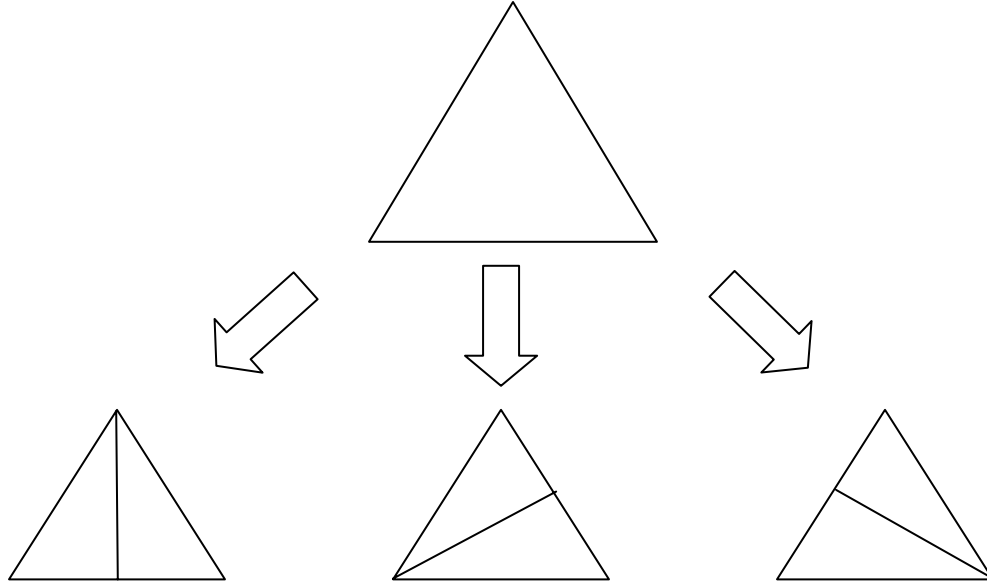


Figure 4.6: Subdivision of element for one hanging node

Finally, the total number of new elements and nodes can be calculated as follows:

$$\left(\begin{array}{l} \text{Total number of nodes} \\ \text{in the next calculation} \end{array} \right) = \left(\begin{array}{l} \text{Total number of nodes} \\ \text{in current calculation} \end{array} \right) + \left(\begin{array}{l} \text{Number of} \\ \text{edges bisected} \end{array} \right) \quad (4.70)$$

$$\left(\begin{array}{l} \text{Total number of elements} \\ \text{in the next calculation} \end{array} \right) = \sum_{E=1}^{NELM} \left(\begin{array}{l} \text{Number of edges bisected} \\ \text{in the element } E \end{array} \right) + 1 \quad (4.71)$$

4.6 Coupled Space-Angle Adaptive Strategy

Thus far, we have developed the residual-based error estimators and mesh refinement strategy. The developed coupled space-angle adaptivity algorithm is summarized in Figure 4.7. The basic strategy is to march through from the lower order angular approximation to the higher order approximations. At each P_N approximation, the spatial convergence is first sought. Then, the spatially converged solution is projected onto the higher order angular spaces to estimate angular truncation errors.

0. Set the angular order to be P_1 ($N=1$)
1. Calculate the FE- P_N solution ψ_h .
2. Compute the FE residual and estimate the spatial discretization errors (η_E).
3. Refine the spatial element where the error indicator is greater than the specified tolerance, and take care of the hanging nodes produced.
4. If all the spatial elements satisfy the convergence criteria, go to Step 5, else go to Step 1.
5. Project the spatially converged P_N solution to the P_{N+2} angular space and solve local residual problem to estimate angular truncation errors.
6. Increase the angular expansion order to $N+2$ where the angular convergence is not satisfied.
7. If all the elements are angularly converged, or the angular order reaches the specified maximum angular order, stop, else go to Step 1.

Figure 4.7: A coupled space-angle adaptive strategy

4.6.1 Consideration to the Eigenvalue, Fission Source Problem

The adaptivity algorithm was developed under the basic assumption that the source term is known. When fissions are present in the system, an iterative procedure must be employed to determine the fission source. The even-parity source term with fissions can be written as:

$$S^+(\mathbf{r}, \boldsymbol{\Omega}) = s^+(\mathbf{r}, \boldsymbol{\Omega}) + \frac{1}{4\pi} \int_{4\pi} d\Omega' \nu \sigma_f \phi^+(\mathbf{r}, \boldsymbol{\Omega}') \quad (4.72)$$

Strictly speaking, the fission source term is also prone to the discretization error due to the dependence on the even-parity flux term; however, in this thesis, we assume that the error in the fission source is negligible such that the same adaptivity framework can be applied as for a fixed source problem. The spatial discretization errors are then estimated when the fission source is converged for a given mesh.

4.6.2 Consideration to the Multigroup Problem

Most of the real-life applications are the multigroup problem. The even-parity transport equation in the matrix multigroup form is not self-adjoint; therefore, *a posteriori* error analysis of this chapter is not exactly valid. However, if we consider the problem as a series of one group problems, then within each group, the problem is self-adjoint. In this case, we can perform a similar treatment to the multigroup problem as we treated fission—ignore the discretization error caused by the group-to-group scattering source and estimate the error.

There are two main possible mesh refinement strategies for the multigroup problems. One possible strategy is to apply the adaptive refinement separately on each group. An alternative strategy is to treat a whole group as the one problem and apply adaptive refinement. It seems that the first method is more efficient since the refinement is tuned to a specific group as it is well known that the physics of the fast and thermal groups have different characteristics. The drawbacks of this methodology are the complicated interpolation scheme for the group-to-group scattering and cumbersome data management system. Since a number of groups can easily exceed one hundred, having different meshes for each group may not be feasible. Therefore, we choose to use the unified mesh. The total errors are computed by the sum of the group-wise errors.

4.7 Summary

In this chapter, we have derived *a posteriori* error expression for the even-parity transport equation in terms of the global L_2 and energy norms. In order to use the error indicators in the context of the adaptivity, the spatial and angular error components were separated by first seeking spatial convergence in given angular expansion order. Then, the angular truncation error was estimated by projection of the spatially converged solution onto the higher order angular space. The difficulty obtaining the surface angular

integral was overcome by the rotation of the coordinates system. General spatial mesh refinement method through edge bisection was also discussed.

CHAPTER 5

GOAL-ORIENTED ADAPTIVITY AND ERROR CONTROL

In the previous chapter, we have derived the global error indicators based on *a posteriori* error estimates for the L_2 and energy norms. The adaptive strategy together with the error estimates can optimize the computational effort whilst minimizing the error in the global even-parity flux. On the other hand, it is often the case that the physical parameters of interest in engineering practice are described by local (or global) integral quantities (functionals). For example, the power distribution, leakage rate or the effective multiplication constant are often sought for the design of nuclear reactors, while the dose rate to a particular organ may be the most important quantity for the medical physics applications. Therefore, an error indicator with respect to some prescribed engineering or physical output may be more relevant to real-life applications. Recent development of a “goal-oriented” adaptive strategy [14, 12] provides the methodology to estimate the error in functional outputs due to discretizations. The basic philosophy of goal-oriented adaptivity is to characterize arbitrary target functionals by utilizing the dual problem.

Bounds for linear functionals can be computed through variational methods. Maximum and minimum variational principles have long been used to determine upper and lower bounds for local characteristics of solutions [20]. More recently, adjoint error correction schemes have been proposed which yield super convergence in the target functional by utilizing the finite element residuals computed by higher-order interpolation [16, 17]. The objective of this chapter is to develop reliable error bounds for functional outputs of interest by combining variational principles and *a posteriori* error analysis.

5.1 Different Forms of the Extremum Variational Principles

Variational methods have long been used in the field of nuclear engineering, and they can be used to estimate many desired engineering outputs with high-order accuracy

[18]. In this section, we review the extremum variational principles that are equivalent to the second-order form of the transport equation. The derivation presented here closely follows the methodology of Kaplan and Davis [37].

We start with the quadratic variational principle derived in the Chapter 3 [Eq.

(3.4)]:

$$K^+[\psi] = (\boldsymbol{\Omega} \cdot \nabla \psi, G \boldsymbol{\Omega} \cdot \nabla \psi) + (\psi, C\psi) + \langle \psi, \psi \rangle - 2(\psi, S^+) - 2\langle \psi, T \rangle - 2(\boldsymbol{\Omega} \cdot \nabla \psi, GS^-) \quad (3.4)$$

The function that minimizes the functional (3.4) is the best approximated solution in a least-squares sense. The canonical and involutory transformations of Eq. (3.4) yield different forms of the variational principle. The following subsections discuss main results of the canonical and involutory transformation of the even-parity extremum principle.

5.1.1 The Canonical Form of the Even-Parity Variational Principle

The first variant of the even-parity variational principle is of the canonical form. In order to obtain it, let us denote the streaming term to be $\xi = \boldsymbol{\Omega} \cdot \nabla \psi$. Then, Eq. (3.4) may be rewritten as:

$$K_2^+[\psi, \xi] = (\xi, G\xi) + (\psi, C\psi) + \langle \psi, \psi \rangle - 2(\psi, S^+) - 2\langle \psi, T \rangle - 2(\xi, GS^-) \quad (5.1)$$

The variational problem corresponding to Eq. (5.1) is seen as seeking a set of trial functions ψ and ξ , which minimize Eq. (5.1). The functional (5.1) has the same minimum value as Eq. (3.4) when $\xi = \boldsymbol{\Omega} \cdot \nabla \psi$. This canonical form of the variational principle is employed to form the mixed finite element formulation [41].

5.1.2 The Canonical Variational Principle with Lagrange Multiplier

The canonical variational principle can be extended to the Lagrange multiplier form of the equivalent variational principle. Denoting χ as Lagrange multiplier we can write the following variational principle:

$$K_3^+(\chi)[\psi, \xi] = (\xi, G\xi) + (\psi, C\psi) + \langle \psi, \psi \rangle - 2(\psi, S^+) - 2\langle \psi, T \rangle - 2(\xi, GS^-) + 2(\chi, \xi - \boldsymbol{\Omega} \cdot \nabla \psi) \quad (5.2)$$

This Lagrange multiplier form of the variational principle can be used to derive the mixed finite element formulation employed in the VARIANT code [49]. By taking the first variation of Eq. (5.2), we obtain the following Euler-Lagrange equations:

$$G\xi - GS^{-1} + \chi = 0 \quad (5.3)$$

$$C\psi - S^+ + \boldsymbol{\Omega} \cdot \nabla \chi = 0 \quad (5.4)$$

$$\psi + \chi = T \text{ on } \Gamma \quad (5.5)$$

Eq. (5.3), (5.4) and (5.5) comparing with Eq. (2.24) and (2.25) reveals that the parameter χ is, in fact, the odd-parity flux. The Lagrange multiplier can be used to form the Mortar finite element method, which is a popular non-conforming finite element methodology [41].

5.1.3 Involutory Form of the Variational Principle

The fourth form of the variational principle is obtained by the involutory transformation of Eq. (3.4). It uses the relationship between the even- and odd parity flux given by Eq. (5.4):

$$\psi = C^{-1} [S^+ - \boldsymbol{\Omega} \cdot \nabla \chi] \quad (5.6)$$

By substituting Eq. (5.6) into the Lagrange multiplier form of the variational principle (5.2) and rearranging we get:

$$\begin{aligned}
K^-[\chi] = & -(\boldsymbol{\Omega} \cdot \nabla \chi, C^{-1} \boldsymbol{\Omega} \cdot \nabla \chi) - (\chi, G^{-1} \chi) - \langle \chi, \chi \rangle \\
& + 2(\chi, S^-) + 2\langle \chi, T \rangle + 2(\boldsymbol{\Omega} \cdot \nabla \chi, C^{-1} S^+) \\
& + (S, GS) + (S, CS) + 2\langle T, T \rangle
\end{aligned} \tag{5.7}$$

5.1.4 Extremum Value of the Variational Principle

The functionals (3.4), (5.1), (5.2), and (5.7) are all equivalent; therefore, they all have the same extremum value. Due to the self-adjointness of the operators G and C , and the second variation being positive, the extremum value of the functional (3.4), (5.1), and (5.2) represents a minimum. On the other hand, the extremum value of the variational principle (5.7) represents a maximum. Let the extremum value of the functional (3.4), (5.1), (5.2), and (5.7) be γ . Then, γ is bounded by:

$$K^-[\chi] \leq \gamma \leq K^+[\psi] \tag{5.8}$$

The equality holds only when the ψ and χ are the exact even- and odd-parity solutions of the system. Figure 5.1 illustrates the relationship among $K^+[\psi]$, $K^-[\chi]$ and γ .

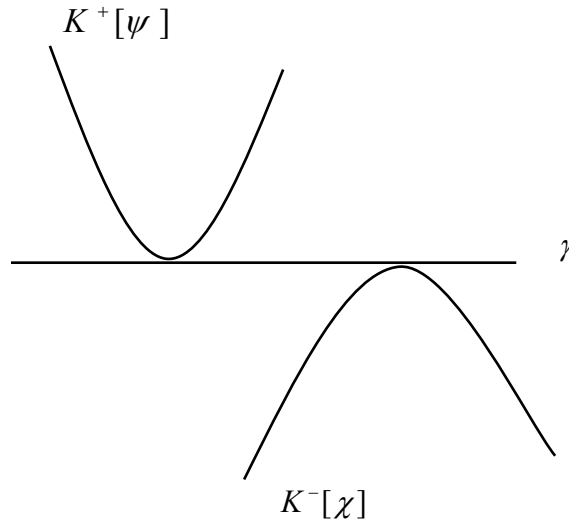


Figure 5.1: Illustration of the original and involutory form of the variational principles

5.2 Bounds on Functionals

In the previous section, we derived different forms of the extremum variational principles by the canonical and involutory transformations. Furthermore, we have shown that the extremum value can be bounded between the original (3.4) and the involutory form (5.7) of the variational principle. Although the functional K^+ represents the physical quantity [37] for special cases, the K^+ variational principle generally lacks a physical meaning. Thus, a methodology which offers the bounds for an arbitrary functional is desired. We start by rewriting Eq. (3.4) in terms of a linear combination of the bilinear functionals introduced in the previous chapter:

$$K^+[\psi] = F[\psi, \psi] - 2F_s[\psi] \quad (4.3)$$

When the trial function ψ is the true solution ϕ^+ of the even-parity transport equation (Eq. (2.27)), then the RHS of Eq. (4.3) may be simplified as:

$$\begin{aligned} K^+[\phi^+] &= F[\phi^+, \phi^+] - 2F_s[\phi^+] \\ &= F[\phi^+, \phi^+] - 2F[\phi^+, \phi^+] \\ &= -F[\phi^+, \phi^+] \end{aligned} \quad (5.9)$$

Since the $K^+[\psi]$ principle takes the minimum value at the true solution, the $K^+[\psi]$ principle bounds the bilinear functional $F[. , .]$ from above:

$$-F[\phi^+, \phi^+] \leq K^+[\psi] \quad (5.10)$$

Similarly, the lower bound of $F[. , .]$ is found by applying the $K_4^+[\chi]$ principle.

$$K^-[\chi] \leq -F[\phi^+, \phi^+] \quad (5.11)$$

Now, let us consider the dual problem corresponding to Eq. (3.4). Due to the self-adjointness of the one-group, even-parity transport equation, the variational principle corresponding to the dual problem of Eq. (3.4) can be written as:

$$\begin{aligned}
K^{+*}[\psi^*] &= (\boldsymbol{\Omega} \cdot \nabla \psi^*, G \boldsymbol{\Omega} \cdot \nabla \psi^*) + (\psi^*, C \psi^*) + \langle \psi^*, \psi^* \rangle \\
&\quad - 2(\psi^*, S^{+*}) - 2\langle \psi^*, T^* \rangle - 2(\boldsymbol{\Omega} \cdot \nabla \psi^*, G S^{-*}) \\
&= F[\psi^*, \psi^*] - 2F_s^*[\psi^*]
\end{aligned} \tag{5.12}$$

where ψ^* is the trial function in the dual problem,

$S^{\pm*}$ are the even- and odd components of the prescribed source in the dual problem, and

T^* is the surface source in the dual problem.

Since the adjoint source is arbitrary, the target functional quantity of interest can be represented by the product between the even-parity flux and the adjoint source term $F_s^*[\psi]$. For example, a reaction rate for a particular region can be expressed by setting $S^{+*} = \sigma$, $S^{-*} = 0$ and $T^* = 0$:

$$\begin{aligned}
F_s^*[\psi] &= (\psi, S^{+*}) \\
&= \int_{V_a} dV \int_{4\pi} d\Omega \sigma \psi
\end{aligned} \tag{5.13}$$

The leakage rate through a vacuum surface can be expressed as:

$$\begin{aligned}
F_s^*[\psi] &= \langle \psi, T^{+*} \rangle \\
&= \int_{\Gamma_b} d\Gamma \int_{\boldsymbol{\Omega} \cdot \mathbf{n} > 0} d\Omega |\boldsymbol{\Omega} \cdot \mathbf{n}| \psi \\
&= \int_{\Gamma_b} d\Gamma \int_{\boldsymbol{\Omega} \cdot \mathbf{n} > 0} d\Omega |\boldsymbol{\Omega} \cdot \mathbf{n}| G \boldsymbol{\Omega} \cdot \nabla \psi
\end{aligned} \tag{5.14}$$

The exact value of the target functional quantity is, then, expressed by the product of the forward and adjoint solutions:

$$F_s^*[\phi^+] = F[\phi^+, \phi^*] \tag{5.15}$$

Making use of the bilinearity of the functional $F[.,.]$

$$F[\phi^+ \pm \phi^*, \phi^+ \pm \phi^*] = F[\phi^+, \phi^+] \pm 2F[\phi^+, \phi^*] + F[\phi^*, \phi^*] \tag{5.16}$$

$$F[\phi^+, \phi^*] = \frac{1}{4} (F[\phi^+ + \phi^*, \phi^+ + \phi^*] - F[\phi^+ - \phi^*, \phi^+ - \phi^*]) \tag{5.17}$$

Then the RHS of the Eq. (5.15) may be rewritten as the following linear combination of the quadratic functional:

$$\begin{aligned} F_s^*[\phi^+] &= F[\phi^+, \phi^*] \\ &= \frac{1}{4} \left(F[\phi^+ + \phi^*, \phi^+ + \phi^*] - F[\phi^+ - \phi^*, \phi^+ - \phi^*] \right) \end{aligned} \quad (5.18)$$

Finally, by utilizing Eq. (5.10) and Eq. (5.11), the target functional value can be bounded by the linear combination of the extremum principles:

$$-K_a^+[\psi + \psi^*] \leq F[\phi^+ + \phi^{+*}, \phi^+ + \phi^{+*}] \leq -K_a^-[\chi + \chi^*] \quad (5.19)$$

$$-K_b^+[\psi - \psi^*] \leq F[\phi^+ - \phi^{+*}, \phi^+ - \phi^{+*}] \leq -K_b^-[\chi - \chi^*] \quad (5.20)$$

$$\frac{1}{4} \left(-K_a^+[\psi + \psi^*] + K_b^-[\chi - \chi^*] \right) \leq F_s^*[\phi^+] \leq \frac{1}{4} \left(K_b^+[\psi - \psi^*] - K_a^-[\chi + \chi^*] \right) \quad (5.21)$$

The subscripts a and b in Eq. (5.21) indicate the difference from the original variational principles. The source functionals in these variational principles are represented by the linear combination of the forward and adjoint source terms. Note that in order to obtain the bound in Eq. (5.21), one must solve four problems (forward and adjoint problem of the even- and odd-parity equations).

5.3 Goal-Oriented Error Bounds

We have derived the bounds of an arbitrary functional using the dual problem. However, the drawback of this methodology originates from the fact that the bound contains four unknown functions. The computational effort to solve the four problems may become prohibitively large, and the method thus may not be practical. In the previous chapter, we have derived *a posteriori* error bounds based on the global L_2 norm, which also utilized the adjoint problem. The methodology can be generalized to express an arbitrary functional quantity. The goal-oriented error bound [14, 12] utilizes the various norm inequalities in the course of the derivation.

The starting point of the derivation of the goal-oriented error bounds is Eq. (5.15):

$$F[\phi^+, \phi^*] = F_s^*[\phi^+] \quad (5.15)$$

We have also characterized the discretization error in terms of the residual equation

(4.29)

$$F[\phi, e_{h,N}] = F_s[\phi] - F[\phi, \psi_{h,N}] \quad (4.26)$$

A residual equation in the adjoint problem can be introduced as:

$$F[w, \varepsilon_{h,N}] = F_s[w] - F[w, \psi_{h,N}^*] \quad (5.22)$$

where $\varepsilon_{h,N}$ is the discretization error in the adjoint problem, and w is the basis function in the adjoint problem.

The error in the (linear) target functional output is represented as:

$$\begin{aligned} F^*[e] &= F^*[\psi] - F^*[\psi_{h,N}] \\ &= F[\psi, \psi^* - \psi_{h,N}^*] - F[\psi_{h,N}, \psi^* - \psi_{h,N}^*] \\ &= F[e_{h,N}, \varepsilon_{h,N}] \end{aligned} \quad (5.23)$$

Utilizing a similar bilinear property to Eq. (5.18), the error in the target functional can be rewritten as:

$$\begin{aligned} F^*[e] &= F[e, \varepsilon] \\ &= F[se, \varepsilon / s] \\ &= \frac{1}{4} F\left[se + \frac{\varepsilon}{s}, se + \frac{\varepsilon}{s}\right] - \frac{1}{4} F\left[se - \frac{\varepsilon}{s} / s, se - \frac{\varepsilon}{s}\right] \end{aligned} \quad (5.24)$$

where $s = \sqrt{\frac{(F[\varepsilon, \varepsilon])^{1/2}}{(F[e, e])^{1/2}}}$. The parameter s is introduced so that the error in forward

(e) and adjoint (ε) problems scale equally. Different *a posteriori* error estimates give the upper and lower bounds of the energy norm. Let us denote the upper and lower bounds of the energy norm be η_{low}^+ , η_{up}^+ , η_{low}^- , and η_{up}^- , which consist of the following bounds:

$$\left(\eta_{low}^+\right)^2 \leq F\left[se + \frac{\varepsilon}{s}, se + \frac{\varepsilon}{s}\right] \leq \left(\eta_{up}^+\right)^2 \quad (5.25)$$

$$\left(\eta_{low}^-\right)^2 \leq F\left[se - \frac{\varepsilon}{s}, se - \frac{\varepsilon}{s}\right] \leq \left(\eta_{up}^-\right)^2 \quad (5.26)$$

By using Eq. (5.25) and (5.26), the bound in the error in the target functional (5.24) can be expressed as:

$$\frac{1}{4}\left(\eta_{low}^+\right)^2 - \frac{1}{4}\left(\eta_{up}^-\right)^2 \leq F_s^*[e] \leq \frac{1}{4}\left(\eta_{up}^+\right)^2 - \frac{1}{4}\left(\eta_{low}^-\right)^2 \quad (5.27)$$

Due to the positivity of the quadratic functional, another wider bound can be developed by taking the maximum values of Eq. (5.25) and (5.26):

$$-\frac{1}{4}\left(\eta_{up}^-\right)^2 \leq F_s^*[e] \leq \frac{1}{4}\left(\eta_{up}^+\right)^2 \quad (5.28)$$

In fact the upper bounds η_{up}^+ and η_{up}^- can be estimated by the developed *a posteriori* error estimators, which is the solution of the local residual problem defined by Eq. (4.52) [14, 12]. The error bound (5.28) therefore requires only the linear combination of the even-parity forward and adjoint solutions.

5.4 *A Posteriori* Error Bounds by the Extremum Variational Principles and Goal-Oriented Error Bounds

In the previous two sections, we have derived the expression which bounds the arbitrary functional quantities by means of the variational principles and *a posteriori* error analysis. In this section, we introduce new functional error bounds by integrating both concepts. The extremum variational principles applied to the residual equation can provide the following functional bounds:

$$-\tilde{K}_a^+[\tilde{e} + \tilde{\varepsilon}] \leq F[e + \varepsilon, e + \varepsilon] \leq -\tilde{K}_a^-[\tilde{e}^- + \tilde{\varepsilon}^-] \quad (5.29)$$

$$-\tilde{K}_b^+[\tilde{e} - \tilde{\varepsilon}] \leq F[e - \varepsilon, e - \varepsilon] \leq -\tilde{K}_b^-[\tilde{e}^- - \tilde{\varepsilon}^-] \quad (5.30)$$

$$\frac{1}{4}\left(-\tilde{K}_a^+[\tilde{e} + \tilde{\varepsilon}] + \tilde{K}_b^-[\tilde{e}^- - \tilde{\varepsilon}^-]\right) \leq F_s^*[e] \leq \frac{1}{4}\left(\tilde{K}_b^+[\tilde{e} - \tilde{\varepsilon}] - \tilde{K}_a^-[\tilde{e}^- + \tilde{\varepsilon}^-]\right) \quad (5.31)$$

The variational principles with symbol “ \sim ” indicate the maximum principle of the even-parity residual equations. For example, the residual form of the K^+ principle is expressed in the following form:

$$\begin{aligned}\tilde{K}^+[e] &= (\boldsymbol{\Omega} \cdot \nabla e, G\boldsymbol{\Omega} \cdot \nabla e) + (e, Ce) + \langle e, e \rangle \\ &\quad - 2\langle e, \tilde{S}^+ \rangle - 2\langle e, \tilde{T} \rangle - 2(\boldsymbol{\Omega} \cdot \nabla e, G\tilde{S}^-)\end{aligned}\quad (5.32)$$

where, $\tilde{S}^+ = S^+ - C\psi_h$

$$\tilde{S}^- = S^- - \boldsymbol{\Omega} \cdot \nabla \psi_h, \text{ and}$$

$$\tilde{T} = T - T_h.$$

Then, $\tilde{K}_a^\pm[.]$ and $\tilde{K}_b^\pm[.]$ are the extremum principles related to the linear combination of the forward and adjoint residual equations. Recognizing that the lower bounds of the functionals $F[e \pm \varepsilon, e \pm \varepsilon]$ consist of the K^+ principle, and implicit error estimator provides the upper bound of the same functional, we are able to form new error bounds from the combination of Eq. (5.25), (5.26), (5.29) and (5.30) as follows:

$$-\tilde{K}_a^+[\tilde{e} + \tilde{\varepsilon}] \leq F[e + \varepsilon, e + \varepsilon] \leq (\eta_{up}^+)^2 \quad (5.33)$$

$$-\tilde{K}_b^+[\tilde{e} - \tilde{\varepsilon}] \leq F[e - \varepsilon, e - \varepsilon] \leq (\eta_{up}^-)^2 \quad (5.34)$$

$$\frac{1}{4} \left(-\tilde{K}_a^+[\tilde{e} + \tilde{\varepsilon}] - (\eta_{up}^-)^2 \right) \leq F_s^*[e] \leq \frac{1}{4} \left((\eta_{up}^+)^2 + \tilde{K}_b^+[\tilde{e} - \tilde{\varepsilon}] \right) \quad (5.35)$$

Therefore, the error in the functional output is bounded only by the error estimates of the forward and adjoint problem. Then, the true error can be estimated by taking the average of (5.35):

$$F_s^*[e] \approx \frac{1}{8} \left((\eta_{up}^+)^2 - (\eta_{up}^-)^2 + \tilde{K}_b^+[\tilde{e} - \tilde{\varepsilon}] - \tilde{K}_a^+[\tilde{e} + \tilde{\varepsilon}] \right) \quad (5.36)$$

5.5 Summary

In this chapter, we have extended the concept of *a posteriori* error analysis to the target functionals. Different forms of the even-parity variational principles were first

derived via the canonical and involutory transformations. The bounds on an arbitrary linear functional was obtained by the combination of the forward and adjoint problems of the even- and odd-parity variational principles. The reliable, yet easily computable, functional error bounds were then derived by integrating the concept of the variational bounds and finite element *a posteriori* error estimates.

CHAPTER 6

NUMERICAL RESULTS

In the last three chapters, we have developed *a posteriori* error estimators and a coupled space-angle adaptivity algorithm based on the second-order, even-parity form of the transport equation. This adaptive algorithm has been implemented in the general purpose neutral particle radiation transport code EVENT [35] and is numerically assessed in this chapter. We begin by employing the Method of Manufactured Solution (MMS) to validate the adaptivity algorithm. This is followed by the solution of several one- and two-dimensional problems by both the adaptive and standard finite element method.

6.1 The Method of Manufactured Solution

The implementation of an adaptive algorithm can enhance the performance of the existing computer code to a great extent. However, without proper verification of the new numerical implementation, the computer code may have its performance deteriorated due to the extra complexity added by the new subroutines. In radiation transport, the verification of a computer code is often carried out by benchmarking solutions against the Monte Carlo method [50]. Due to the nature of the Monte Carlo method, the benchmark result is often in a form of some local integral quantity such as pin power or dose rate, or some global characteristic parameter such as the effective multiplication constant ($k\text{-eff}$). This type of the benchmarking effort is often sufficient to check the capability and accuracy of the code. However, it may experience difficulty in assessing the theoretical properties of the new algorithm in view of the lack of fine solution detail.

The method of manufactured solution (MMS) [51] provides an excellent alternative way to verify the theoretical properties of numerical schemes. The philosophy behind the MMS is to calculate the source term from a pre-manufactured solution. Thus,

large groups of the analytical solutions can be made available for numerical tests. In this section, we introduce the MMS for the even-parity transport equation.

The second-order, even-parity transport equation introduced in the chapter 2 is:

$$-\mathbf{\Omega} \cdot \nabla G \mathbf{\Omega} \cdot \nabla \phi^+ + C\phi^+ = S^+ - \mathbf{\Omega} \cdot \nabla G S^- \quad (2.27)$$

By simply comparing the RHS and LHS of the Eq. (2.27), the parity components of the source terms may be computed from the even-parity flux as:

$$S^+ = C\phi^+ \quad (6.37)$$

$$S^- = \mathbf{\Omega} \cdot \nabla \phi^+ \quad (6.38)$$

We also need to specify the boundary conditions for the problem. Let us denote the even-parity flux at boundary Γ as ϕ_Γ . Then, a proper boundary condition can be provided by setting the surface source term T to the boundary flux ϕ_Γ :

$$T = \phi_\Gamma \quad (6.39)$$

Reflective boundary conditions can be introduced along lines of the symmetry.

6.2 Verification through the Method of Manufactured Solutions

In this section, the developed adaptivity algorithm is verified by the MMS. As mentioned previously, the adaptivity algorithm provides the error indicators for the space-angle discretization. We define the effective index (EI) [8], which indicates how well the estimated error represents the true error, as:

$$(EI) = \frac{(\text{Estimated Error})}{(\text{True Error})} \quad (6.40)$$

It is clear that the closer to unity the effective index is the more effective the error indicator is. Moreover, if the EI is greater than unity, the adaptivity algorithm is considered as a conservative procedure.

6.2.1 Test Case 1—Measure of Zero Error

The first test case is considered in order to demonstrate the accuracy of the finite element calculation when the basis function can characterize the true solution. Test case 1 consists of a 1.0x1.0cm square region. The corresponding cross sections for the problem are 1.0cm^{-1} , 1.0cm^{-1} and 0.0cm^{-1} for the total, absorption and scattering reactions, respectively. In this test problem, the following form of the solution is considered:

$$\phi^+(r, \Omega) = x \quad (6.41)$$

Since the linear basis function can characterize the solution exactly and there is no angular dependence in this test problem, we expect that no spatial mesh refinement is required for and the computation should terminate at the P_1 approximation. The initial mesh and the flux distribution are shown in Figure 6.1.

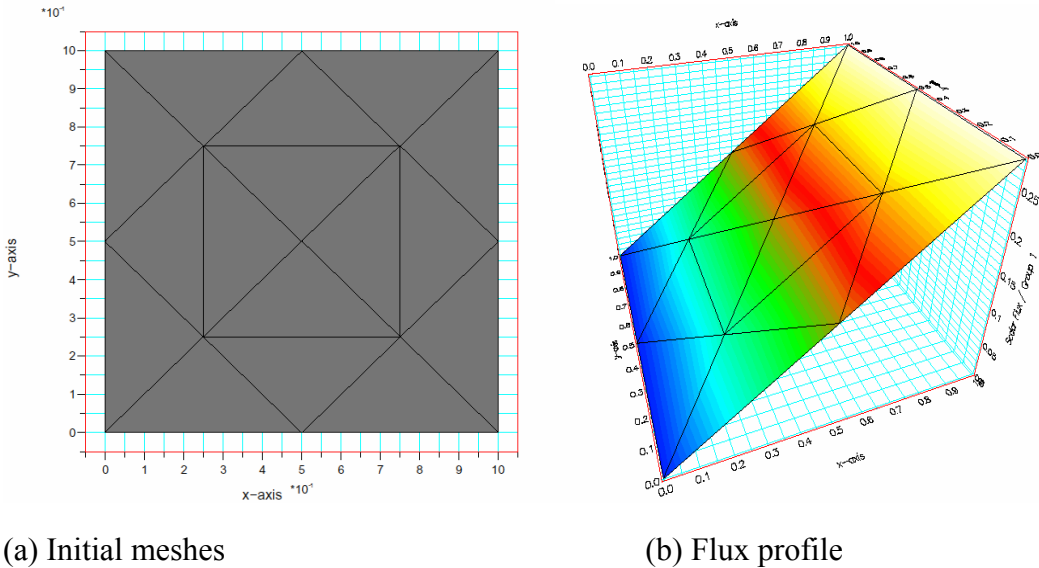


Figure 6.1: Mesh and flux profile for Test Case 1

The spatial and angular global L_2 errors after the first P_1 calculation were calculated to be 2.305×10^{-8} and 1.929×10^{-8} , respectively. As expected, the estimated errors are within the round-off errors; both space and angular error estimators are in fact estimated effectively at zero error for this problem.

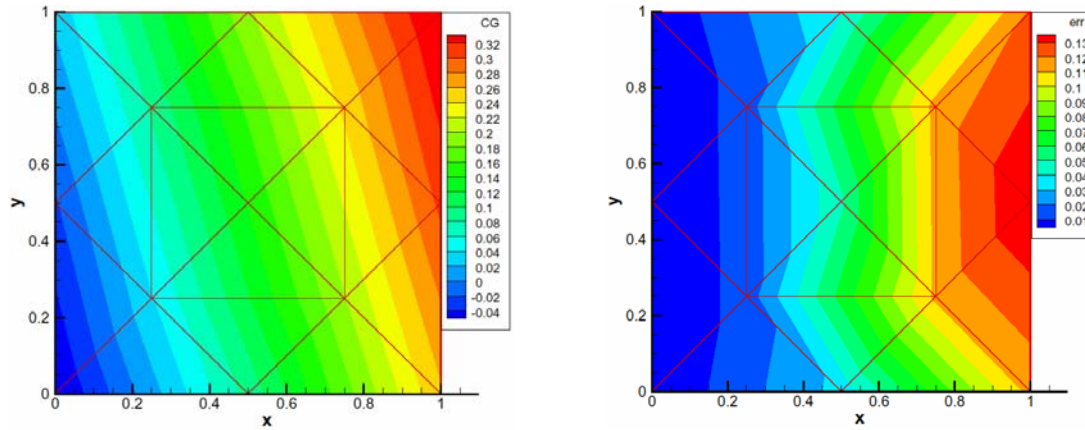
6.2.2 Test Case 2—Measure of Angular Truncation Error

The second test case is manufactured to check the accuracy of the angular truncation errors. The test case 2 has the same configuration as the test case 1, while the solution of this problem is modified to:

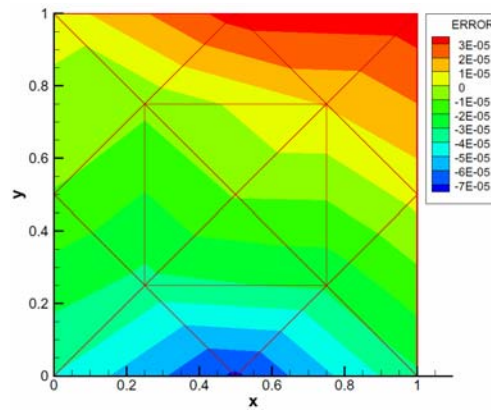
$$\phi^+(\mathbf{r}, \boldsymbol{\Omega}) = x + \sum_{m=0}^{2, \text{even}} Y_{2m}(\boldsymbol{\Omega})x \quad (6.42)$$

The true solution can be characterized exactly by a P_3 linear finite element approximation. Thus, no spatial mesh refinement is expected and solution should converge at the P_3 approximation. The flux profile after P_1 approximation and the estimated angular truncation errors are shown in Figure 6.2. From Figure 6.2(a), we can observe the asymmetric flux distribution. This asymmetry is due to the truncation of the higher-order odd parity source terms, which couples the P_1 and P_3 moments. From Figure 6.2(b), we can observe that the local error estimator computes the angular truncation errors adequately for each element. Figure 6.2(c) shows the difference between true and estimated errors. The estimated and true angular truncation errors of the P_1 approximation were effectively the same for this simple problem.

Table 6.1 gives the estimated and true angular truncation errors for both the P_1 and P_3 approximations. The effective index is found out to be 1.001 when the angular truncation error of the P_1 approximation is estimated by projecting the P_1 solution to the P_3 local finite element problem. The estimated angular truncation error of the P_3 approximation is computed to be 4.006×10^{-8} , which is within the range of the round off errors.



(a) Flux profile after the P_1 approximation (b) Estimated angular truncation error



(c) difference between true and estimated error

Figure 6.2: Flux and estimated angular truncation error in Test Case 2

Table 6.1: Result for Test Case 2

Angular Approximation	Estimated Angular Truncation Error	True Angular Truncation Error	Effective Index
P_1	2.822×10^{-1}	2.820×10^{-1}	1.001
P_3	4.006×10^{-8}	0.0	--

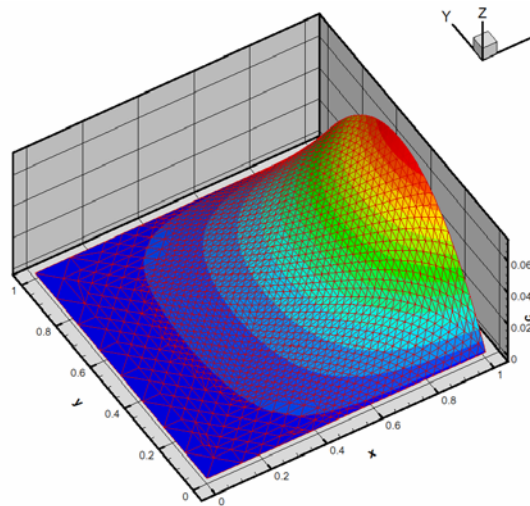
6.2.3 Test Case 3—Measure of Spatial Discretization Error

In the previous subsection, we have demonstrated the validity of the angular error estimator. In this subsection, we investigate spatial adaptivity. The geometry and cross

sections of the problem are identical as the test case 1. Here, we consider the following spatially-dependent solution:

$$\phi^+(\mathbf{r}, \boldsymbol{\Omega}) = x^3(y - y^2) \quad (6.43)$$

The spatial convergence criterion is set to 1.0×10^{-4} . In all example problems presented here, we are considering the absolute errors. The linear basis function can not represent the solution exactly in this case. Figure 6.3 illustrates the flux profile and both estimated and true error distribution at each refinement stage. By comparing the Figure 6.3(b), we can observe very similar error distributions. After five spatial mesh refinement steps, the estimated error has fallen below the prescribed tolerance. The true and estimated error and the effective indices for the each refinement stage are presented in Table 6.2.



(a) Flux profile of the test case 3

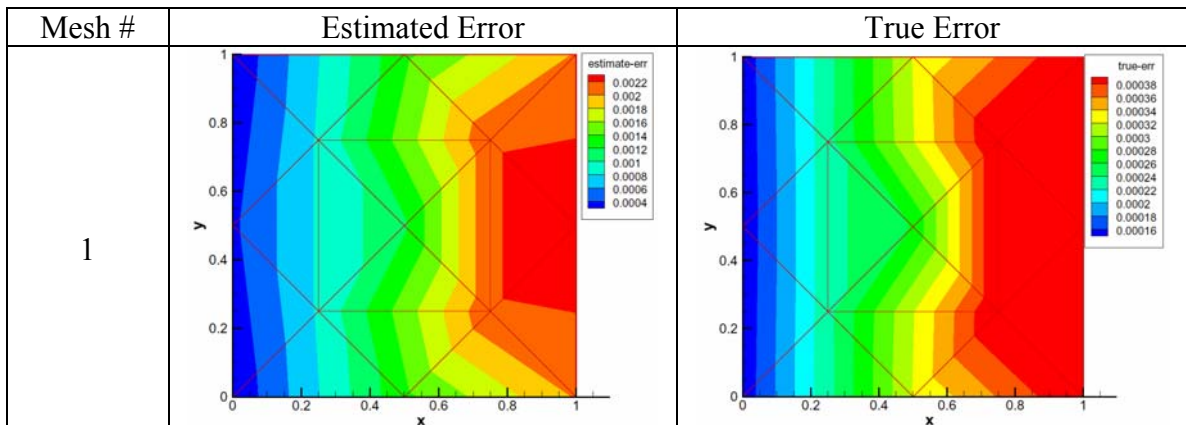
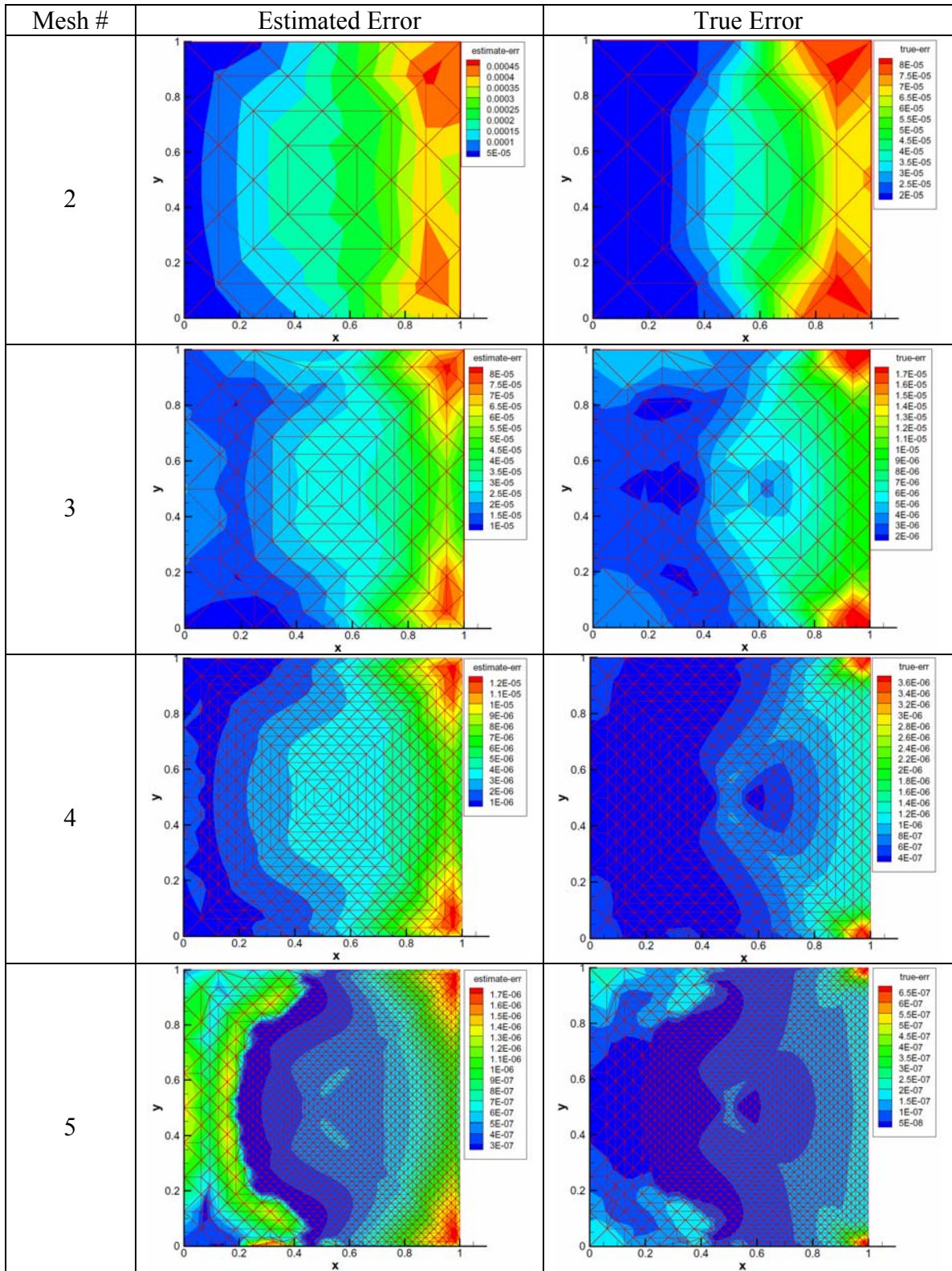


Figure 6.3: Flux profile and the estimated (left) and true (right) errors



(b) Estimated and true errors for each of the spatial refinement steps

Figure6.3: Continued

Table 6.2: Effective index of the spatial mesh refinement

# of Refinements	Estimated Error	True Error	EI
1	1.27×10^{-2}	2.60×10^{-3}	4.91
2	3.78×10^{-3}	7.18×10^{-4}	5.27
3	1.03×10^{-3}	1.88×10^{-4}	5.74
4	2.65×10^{-4}	4.76×10^{-5}	5.56
5	7.32×10^{-5}	1.22×10^{-5}	6.00

As can be seen, the effective indices have values around 4.0-6.0 for this problem, which implies that the explicit error indicator gives the conservative estimates. In fact, the true error has fallen below prescribed tolerance (1.0×10^{-4}) after four refinement steps.

However, the adaptive algorithm performed one extra refinement step. This is a result of the unknown constant introduced for the explicit estimators (Eq. (4.26)) and is one of the drawbacks of the explicit estimator.

Another observation can be made regarding the relation with *a priori* estimates.

The finite element residual $R(\psi_{h,N})$ is defined as:

$$R(\psi_{h,N}) = S^+ - \boldsymbol{\Omega} \cdot \nabla G S^- + \boldsymbol{\Omega} \cdot \nabla G \boldsymbol{\Omega} \cdot \nabla \psi_{h,N} - C \psi_{h,N} \quad (6.44)$$

In the previous section, we have identified the even- and odd-parity source terms for the MMS as:

$$S^+ = C \phi^+ \quad (6.1)$$

$$S^- = \boldsymbol{\Omega} \cdot \nabla \phi^+ \quad (6.2)$$

Thus as $\psi_{h,N}$ approaches the true solution ϕ^+ , the finite element residual does not approach zero but rather a constant value:

$$\begin{aligned} \lim_{\psi_{h,N} \rightarrow \phi^+} R(\psi_{h,N}) &= \lim_{\psi_{h,N} \rightarrow \phi^+} \left(S^+ - \boldsymbol{\Omega} \cdot \nabla G S^- + \boldsymbol{\Omega} \cdot \nabla G \boldsymbol{\Omega} \cdot \nabla \psi_{h,N} - C \psi_{h,N} \right) \\ &= -\boldsymbol{\Omega} \cdot \nabla G S^- \\ &= -\boldsymbol{\Omega} \cdot \nabla G \boldsymbol{\Omega} \cdot \nabla \phi^+ \end{aligned} \quad (6.45)$$

We can relate this term to *a priori* error estimators by using Eq. (6.45). The explicit indicator (4.27) thus becomes:

$$\begin{aligned}
\eta_E^2 &= h_E^4 \left\| R(\psi_{h,N}) \right\|_{L_2(Ex\Omega)} + h_E^3 \left\| R_\gamma(\psi_{h,N}) \right\|_{L_2(\partial Ex\Omega)} \\
&\approx h_E^4 \left\| -\boldsymbol{\Omega} \cdot \nabla G \boldsymbol{\Omega} \cdot \nabla \phi^+ \right\|_{L_2(Ex\Omega)} \\
&= ch_E^4
\end{aligned} \tag{6.46}$$

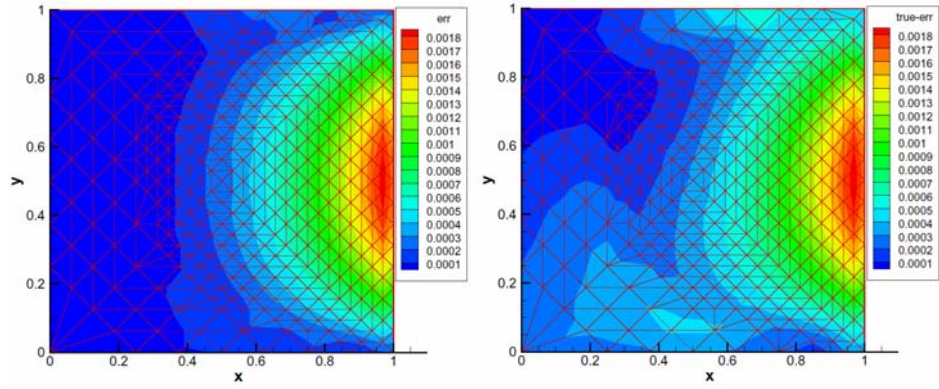
Therefore, we rediscover the expression which is consistent to *a priori* error estimation (Eq. (4.1)).

The next step is to take into account the higher order angular terms such that the effective index of the angular truncation error can also be tested. We seek the following form of the even-parity flux:

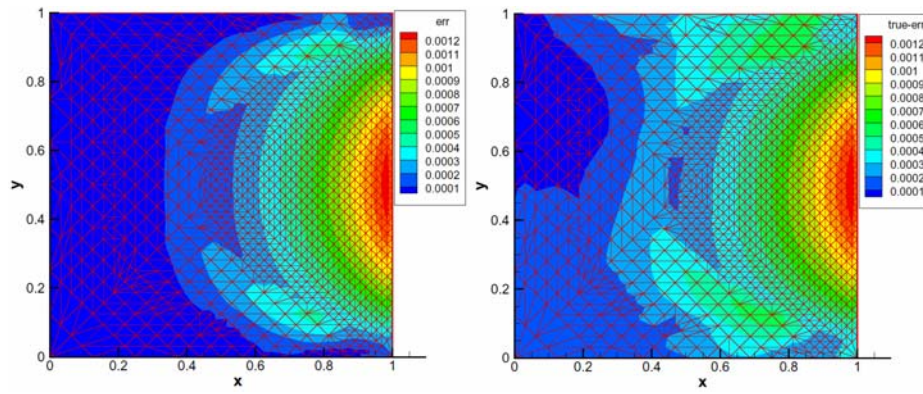
$$\phi^+(\mathbf{r}, \boldsymbol{\Omega}) = x^3(y - y^2) + \sum_{m=0}^{4, \text{even}} Y_{2m}(\boldsymbol{\Omega}) x^3(y - y^2) \tag{6.47}$$

The angular truncation error distributions for both the P₁ and P₃ approximations for this manufactured solution are depicted in Figure 6.3(a) and (b), respectively. The RHS picture illustrates the true error distribution and the LHS illustrates the estimated errors. The asymmetric nature of the error along the *y*-axis again originates from the truncation of the odd-parity source coupling among the different angular moments. Similarly to test case 2, the odd-parity source term produces the asymmetric source distribution for the lower-order calculations.

Figure 6.5 illustrates the distribution of the angular expansion used in this computation. It can be clearly seen that the higher order angular moments are truncated for the region where the flux is relatively low (i.e. $x < 0.2$). The asymmetric flux produced by the odd-parity source truncation causes the non-uniform angular order distributions. Lastly, effective indices of the P₁ and P₃ approximations are listed in Table 6.3. Both effective indices are very close to unity. We conclude that the angular truncation error is estimated sufficiently well using the implicit estimator.



(a) Angular truncation error of the P_1 approximation



(b) Angular truncation error of the P_3 approximation

Figure 6.4: Profile of the angular truncation error for Test Case 3 (right=true error, left=estimated error)

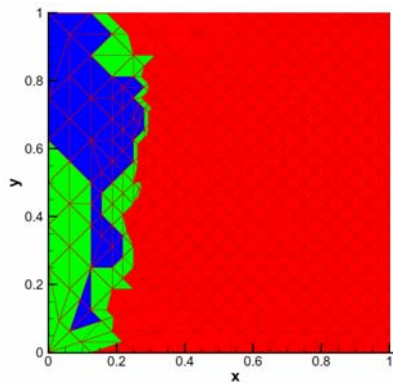


Figure 6.5: Distribution of the angular order used in Test Case 3 (red= P_5 , green= P_3 and blue= P_1)

Table 6.3: Effective index of the angular truncation error for Test Case 3

Angular Approximation	Estimated Angular Truncation Error	True Angular Truncation Error	Effective Index
P ₁	3.38×10^{-2}	3.55×10^{-2}	0.95
P ₃	4.36×10^{-2}	4.64×10^{-2}	0.94
P ₅	1.48×10^{-5}	2.00×10^{-5}	0.74

6.2.4 Test Case 4—Goal-Oriented Adaptivity

In the previous subsections, we have tested the adaptivity algorithm and the error measure based on the global L_2 norm. In this subsection, we assess the goal-oriented adaptivity. The problem objective in this case is to estimate the reaction rate of a deep-penetration problem. The problem consists of the 3.0×4.0 cm rectangular region with an isotropic beam source shining on the left surface (at $x=0.0$ cm). The region consists of a homogeneous purely absorbing medium with cross section of 1.0 cm^{-1} . The quantity of interest is the absorption rate within the region $x \in [0.0, 1.0]$, and $y \in [2.0, 3.0]$. The problem geometry and cross sections are shown in Figure 6.6.

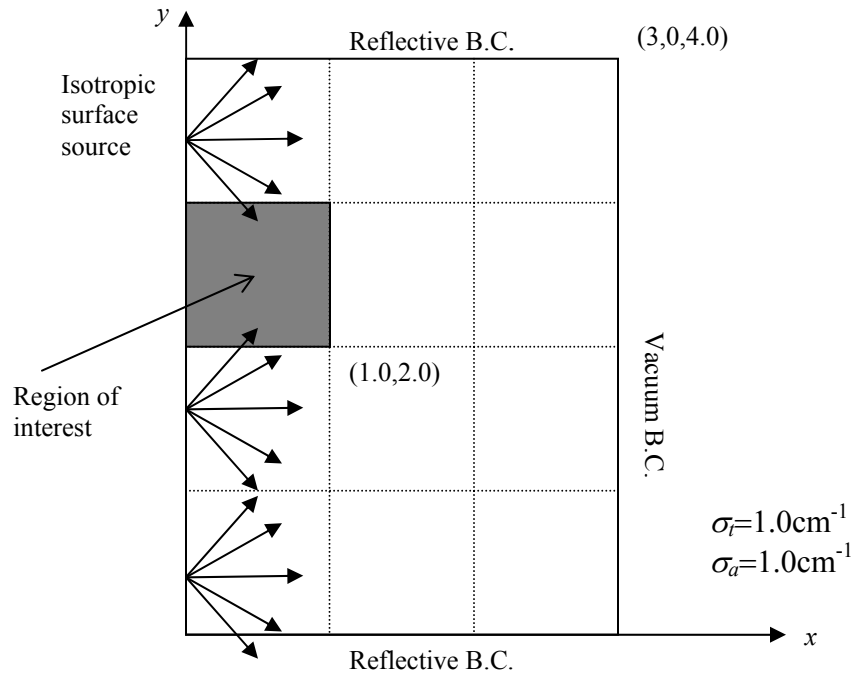


Figure 6.6: Problem description of Test Case 4

Due to the specular reflective boundary condition applied at $y=0.0$ and 4.0cm , this problem can be considered infinite in the y -direction. Therefore, the problem effectively reduces to the following one-dimensional problem:

$$\begin{aligned}\mu' \frac{\partial \psi}{\partial x} + \sigma \psi &= 0 \\ \psi(0, \mu') &= \frac{1}{2\pi} \quad (\mu' \geq 0)\end{aligned}\tag{6.48}$$

where, $\mu' = \Omega \cdot \Omega_x$.

By solving Eq. (6.48), the angular flux of the problem is found out to be:

$$\psi(x, \mu') = \begin{cases} \frac{1}{2\pi} e^{-\frac{\sigma x}{\mu'}} & \mu' > 0 \\ 0 & \mu' \leq 0 \end{cases}\tag{6.49}$$

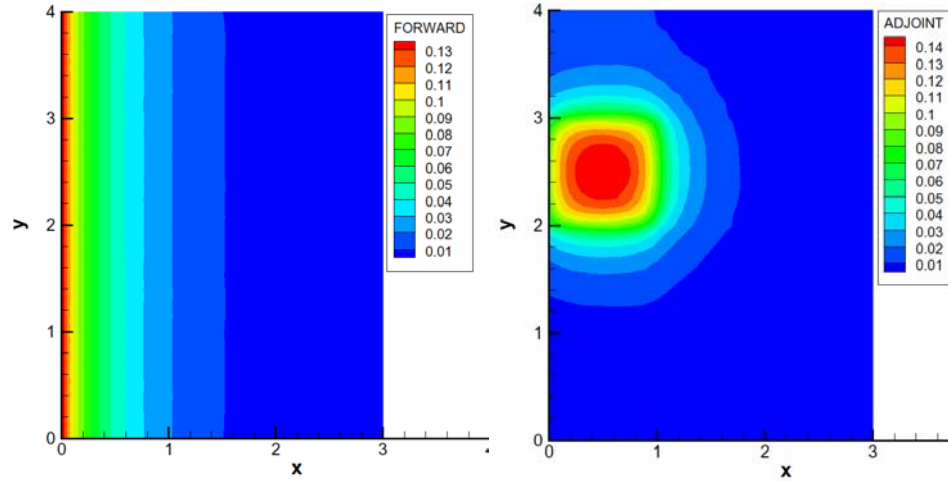
The reaction rate can be computed by integrating Eq. (6.48) over the phase space:

$$\begin{aligned}\int_{2.0}^{3.0} dy \int_{0.0}^{1.0} dx \int_0^1 d\mu' \sigma \psi(x, \mu') &= \frac{1}{2} \int_{0.0}^{1.0} dx \int_0^1 d\mu' e^{-\frac{\sigma x}{\mu'}} \\ &= E_3(0.0) - E_3(1.0)\end{aligned}\tag{6.50}$$

The exact reaction rate of the problem is found out to be 5.5052×10^{-2} . The adjoint problem has the even-parity source of the following form:

$$S^{+*}(x, y) = \begin{cases} \sigma_a & x \in [0.0, 1.0] \text{ and } y \in [2.0, 3.0] \\ 0 & \text{otherwise} \end{cases}\tag{6.51}$$

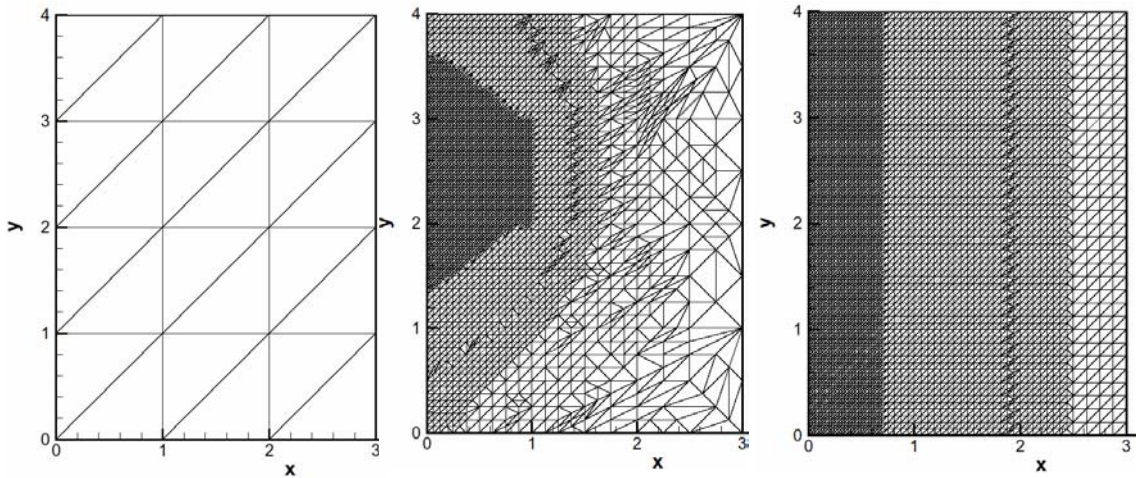
Figure 6.7(a) and (b) illustrates the forward and adjoint solution of the problem. The location of the adjoint source was chosen so that the adjoint problem would have a dependence on the y -direction which reflects on the adaptive mesh generation regardless of the forward problem being effectively one-dimensional. The initial and final adaptive meshes of the problem are shown in Figure 6.8.



(a) Forward scalar flux

(b) Adjoint scalar flux

Figure 6.7: Forward and adjoint scalar flux for Test Case 4



(a) initial mesh

(b) final mesh of the goal-oriented adaptivity (6057 elements)

(c) final mesh of the global L_2 norm adaptivity (9918 elements)

Figure 6.8: Initial and final mesh of Test Case 4

A clear difference in the final meshes between the goal-oriented and the global L_2 adaptivity can be observed from Figure 6.8. As we expected, the adaptivity based on the global L_2 norm has generated the symmetric mesh. On the other hand, it can be clearly

seen that the goal-oriented adaptivity is able to identify the region that influences the target functional output. The total number of elements used in the calculations were 6057 and 9918 for the goal-oriented and the global adaptivity, respectively. Both computations were run up to a P_{15} approximation to obtain the error in the reaction rate of $\sim 1.0 \times 10^{-4}$. About 60% less elements were used in the goal-oriented adaptivity. This difference does not appear to be too significant; however, we expect that efficiency of the goal-oriented adaptivity to increase for more complex and larger problems.

An important advantage of the goal-oriented adaptivity is the availability of an error indicator with respect to the target functional. In fact, in order to obtain the reaction rate error of 1.0×10^{-4} by the global L_2 norm adaptivity, a series of calculations with different error indicators were performed. On the other hand, the goal-oriented adaptivity provides the reliable error bounds which can be used as guidance for the termination of the calculation. A summary of the goal-oriented error estimations is listed in Table 6.4 (without K^+ principle) and Table 6.5 (with K^+ principle). The last column of Table 6.4 and Table 6.5 gives the effective indices calculated with respect to the lower bound. In both cases, we observe that the effective indices have become increasingly small.

As we expected, the inclusion of K^+ principle produces sharper bounds. The effective indices computed with K^+ principles are about 20% smaller than that without K^+ principle. For the higher angular orders (i.e. P_{13} and P_{15}), we observe the effective index has fallen below 1.0. This is a consequence of the upper bound of quadratic functionals $F[e + \varepsilon, e + \varepsilon]$, and $F[e - \varepsilon, e - \varepsilon]$ being computed by the restricted angular basis functions, which appear to underestimate the true upper bound for the higher angular order.

Table 6.4: Error bounds for Test Case 4 without K^+ principle

Angular Order	Lower Bound	Upper Bound	True Error	Effective Index (w.r.t. lower bound)
P ₁	-1.572E-02	1.322E-02	-7.168E-03	2.19
P ₃	-2.830E-03	1.914E-03	-1.878E-03	1.50
P ₅	-1.061E-03	8.483E-03	-6.899E-04	1.54
P ₇	-5.177E-04	4.534E-04	-3.469E-04	1.49
P ₉	-2.955E-04	2.702E-04	-2.206E-04	1.33
P ₁₁	-1.883E-04	1.755E-04	-1.604E-04	1.17
P ₁₃	-1.301E-04	1.224E-04	-1.243E-04	1.05
P ₁₅	-9.508E-05	9.000E-05	-1.007E-04	0.94

Table 6.5: Error bounds for Test Case 4 with K^+ principle

Angular Order	Lower Bound	Upper Bound	True Error	Effective Index (w.r.t. lower bound)
P ₁	-9.353E-03	6.541E-03	-7.168E-03	1.30
P ₃	-2.243E-03	6.061E-04	-1.878E-03	1.19
P ₅	-8.609E-04	4.714E-04	-6.899E-04	1.25
P ₇	-4.287E-04	3.102E-04	-3.469E-04	1.23
P ₉	-2.490E-04	2.020E-04	-2.206E-04	1.13
P ₁₁	-1.617E-04	1.376E-04	-1.604E-04	1.01
P ₁₃	-1.137E-04	9.902E-05	-1.243E-04	0.91
P ₁₅	-8.458E-05	7.463E-05	-1.007E-04	0.84

Table 6.6 and Table 6.7 show the average error and the difference in the reaction rate between the subsequent angular orders. Comparing Table 6.6 and Table 6.7, although the effective indices are relatively small for all the cases, it can be clearly seen that the average errors computed by the bounds with K^+ principles do indeed represent the difference better. Thus, the inclusion of the K^+ bound does not only sharpen the error bounds, but also shifts the error bounds in the right direction.

Table 6.6: Average error computed by the bounds without the K^+ principle

P_N	Average Error	$P_{N+2}-P_N$	EI
1	-1.25E-03	-5.290E-03	0.24
3	-4.58E-04	-1.188E-03	0.39
5	-1.06E-04	-3.430E-04	0.31
7	-3.22E-05	-1.263E-04	0.25
9	-1.27E-05	-6.020E-05	0.21
11	-6.40E-06	-3.610E-05	0.18
13	-3.85E-06	-2.360E-05	0.16
15	-2.54E-06		

Table 6.7: Average error computed by the bounds with the K^+ principle

P_N	Average Error	$P_{N+2}-P_N$	EI
1	-1.41E-03	-5.290E-03	0.27
3	-8.18E-04	-1.188E-03	0.69
5	-1.95E-04	-3.430E-04	0.57
7	-5.93E-05	-1.263E-04	0.47
9	-2.35E-05	-6.020E-05	0.39
11	-1.21E-05	-3.610E-05	0.33
13	-7.34E-06	-2.360E-05	0.31
15	-3.86E-04		

6.3 One-dimensional Examples

In this section, a few one-dimensional, one-group test problems are analyzed in order to assess the potential applicability of a posteriori error estimates and the space-angle adaptivity developed in the previous chapters. We take the angular convergence criteria to be $1/10^{\text{th}}$ of the spatial convergence criteria in order to avoid faulty angular convergence.

6.3.1 Modified Reed's Problem

The first problem is a variation of Reed's problem [52]. The geometry, corresponding cross-sections, and source strength of the problem are listed in Table 6.8. In order to overcome the difficulty of treating the void region in the even-parity formulation, a nominal cross section of 1.0×10^{-6} is assumed for the voided region. Figure 6.9 depicts the scalar flux solution and the angular expansion orders used in the calculation. From Figure 6.9, it can be seen that all regions with the exception of the two left-most slabs (#1 and #2) required the P_{19} angular expansions. The left-most slab only required a P_1 expansion and the slab #2 required a P_{11} angular expansion. In the left-most slab, the isotropic source strength and absorption rate are identical, which creates essentially an isotropic flux. The requirement of smaller angular expansion orders in slab #2 is a result of the magnitude of the flux being small due to the heavily absorbing media. This small magnitude in the flux and hence the error have little effect on the overall accuracy. The angular flux is highly anisotropic in this problem due to the presence of purely absorbing materials. Thus, high-order angular expansion orders are required to solve the problem accurately.

A reference scalar flux solution was obtained by using the converged S_N method developed by Ganapol [53]. Figure 6.10 and Figure 6.11 show the relation between L_∞ error and total number of degrees of freedoms (DoFs) used for both uniform and adaptive refinement calculations of the $P_7 \sim P_{19}$ angular approximations. The maximum L_∞ error occurs at $x=2.0$ cm. At this location, the large material properties and source discontinuity make it difficult to obtain very accurate numerical solution. It can clearly be seen that there are points where the L_∞ error stalls for each angular approximation. At this point, a true spatial convergence is obtained and only the angular truncation error remains. Table 6.9 shows the L_∞ error for the both adaptive and uniform refinement case with up to P_{19} approximation. In order to achieve a similar L_∞ error, the adaptive refinement strategy only requires about $1/8^{\text{th}}$ of total number of DoFs.

Table 6.8: Specification of modified Reed's problem

#	Thickness (cm)	σ_t (cm ⁻¹)	σ_s (cm ⁻¹)	S
1	2.0	50.0	0.0	50.0
2	1.0	5.0	0.0	0.0
3	2.0	10 ⁻⁶	0.0	0.0
4	1.0	1.0	0.9	1.0
5	2.0	1.0	0.9	0.0

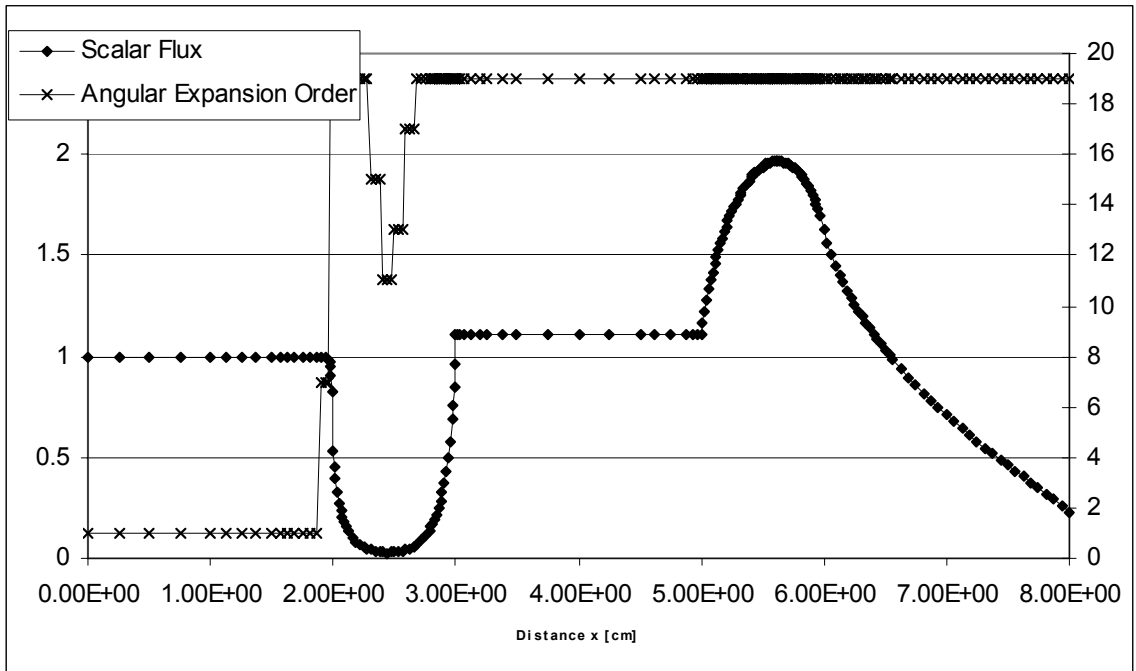


Figure 6.9: Scalar flux solution (left y-axis) and angular expansion used (right y-axis) for the Reed's problem

Table 6.9: Comparison between adaptive and uniform refinement strategies for the modified Reed problem

Angular Order	# of Elements	Total DoFs	Estimated Error	True L_∞ Error
Adaptive Refinement				
P_1	70	70	0.362	0.422
P_3	70	128	0.186	0.127
P_5	114	314	0.114	0.0673
P_7	189	705	0.0797	0.0476
P_9	189	872	0.0606	0.0378
P_{11}	189	1049	0.049	0.0305
P_{13}	265	1754	0.0413	0.0246
P_{15}	265	1997	0.0358	0.0202
Uniform Refinement				
P_1	315	315	0.366	0.426
P_3	800	1115	0.187	0.136
P_5	800	1915	0.114	0.0772
P_7	3200	5115	0.0797	0.0468
P_9	3200	8315	0.0606	0.0369
P_{11}	3200	11515	0.0489	0.0297
P_{13}	3200	14715	0.0411	0.024
P_{15}	3200	17915	0.0356	0.0196

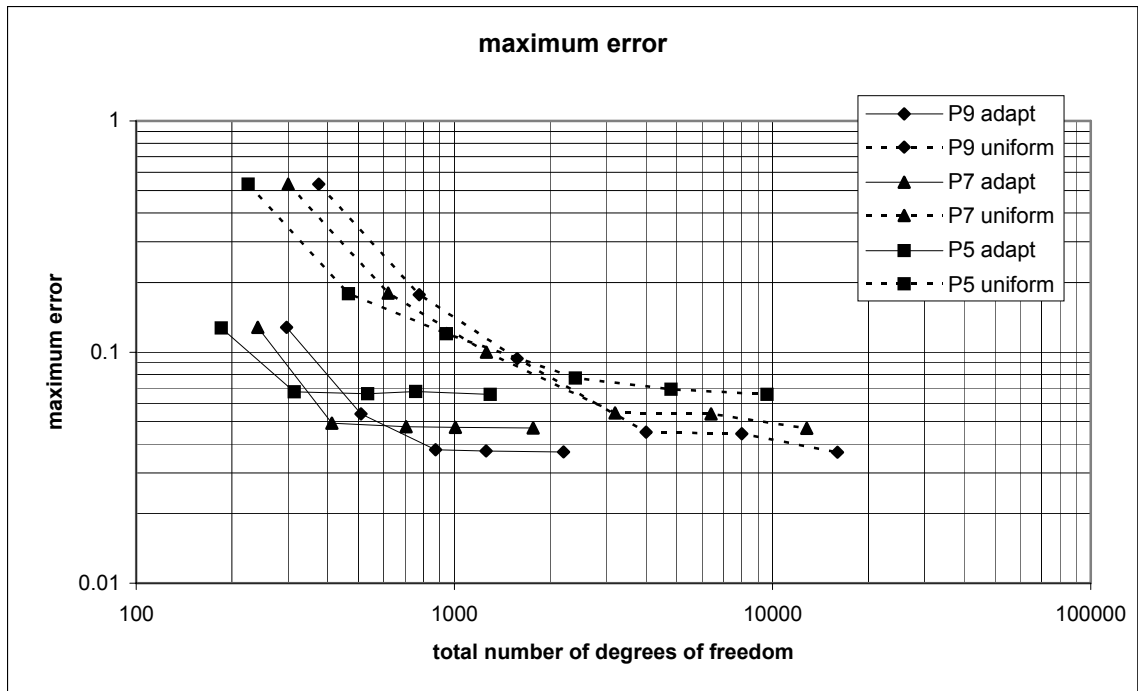


Figure 6.10: Total number of DoFs versus maximum error of P_5 - P_9 approximations

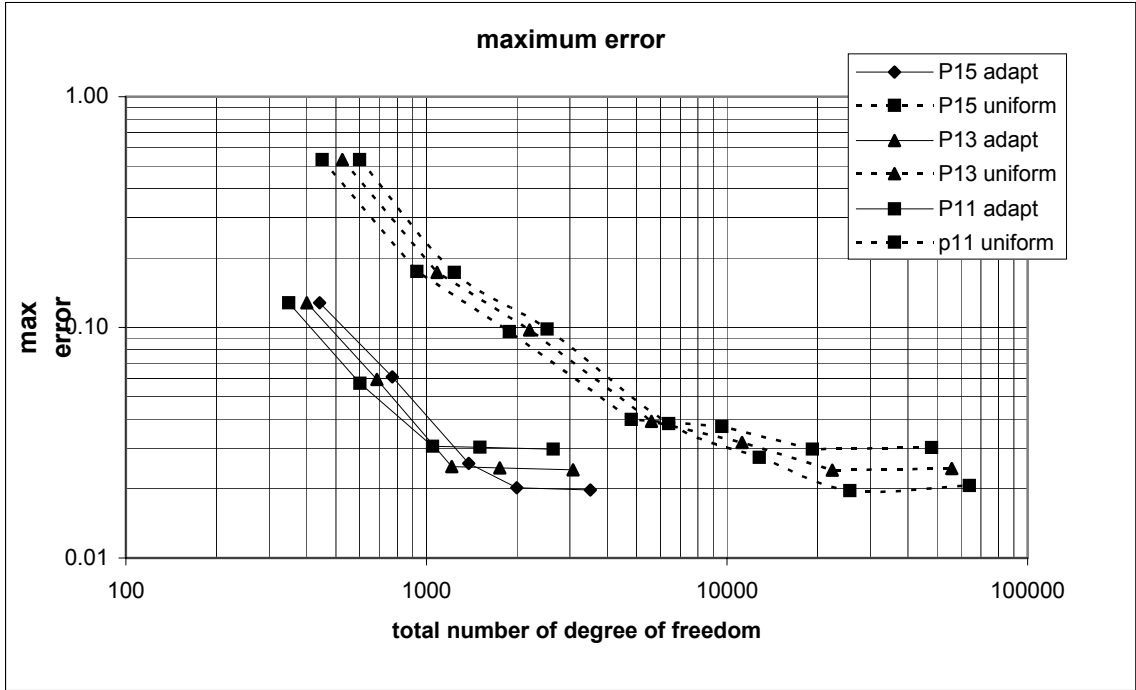


Figure 6.11: Total number of DoFs versus maximum error of P₁₁-P₁₅ approximations

6.3.2 Fission in a Slab Problem

This problem is presented in order to demonstrate a potential applicability of the goal-oriented adaptivity, which is used to estimate the error in the leakage rate. The parameters of the problem are listed on Table 6.10. The isotropic source with unit strength is shining on the left face of the slab. The quantity of interest is the leakage rate at the right face of the slab. The adjoint source term of this problem is defined by:

$$L(w) = \int d\Gamma \int_{\Omega \cdot n < 0} d\Omega (\boldsymbol{\Omega} \cdot \mathbf{n}) w(x, \boldsymbol{\Omega}) \quad (6.52)$$

The leakage rate was again computed by the converged S_N calculation developed by Ganapol [53], and found out to be 0.349509. Table 6.11 shows the comparison between the adaptive mesh and uniform mesh solutions. The uniform mesh case requires twice as many elements as that of adaptive refinements. It appears that the adaptive mesh is not as effective as in the previous examples as indicated by the *EI*. One of the reasons

is that in this case the flux distribution in this problem is relatively linear. Hence, there is no need for the local refinement a particular region.

The finite element solution overestimated the leakage quantity, and the error indicator successfully estimates the error as being a negative quantity. Relatively large values for the effective indices are observed for the low order angular expansion which eventually settles to a value around 1.5. The large values of effective indices in the lower order P_N approximation is due to the treatment of the vacuum boundary condition. It seems to have a difficulty representing the vacuum boundary with the low order P_N approximation. Thus, for the higher order P_N , the error became much smaller and EI approaches close to unity.

Table 6.10: Problem parameters for fission in a slab problem

Thickness	1.853722 cm
σ_T	0.248006986 cm ⁻¹
σ_a	0.022790986 cm ⁻¹
$\nu\sigma_f$	0.010390634 cm ⁻¹

Table 6.11: Summary of fission in a slab problem (True Leakage = 0.34509)

P_N	# ELM	Leakage Computed	Estimated Error	Effective Index
Adaptive Mesh				
1	30	0.360847	-2.70E-01	23.85
5	52	0.350272	-3.52E-03	4.62
9	66	0.349748	-4.51E-04	1.89
13	69	0.349666	-2.10E-04	1.34
17	69	0.349621	-1.75E-04	1.57
21	69	0.349589	-1.12E-04	1.39
Uniform Mesh				
1	137	0.360847	-1.60E-01	14.08
5	137	0.350272	-3.47E-03	4.55
9	137	0.349748	-4.59E-04	1.92
13	137	0.349666	-2.11E-04	1.34
17	137	0.349621	-1.77E-04	1.58
21	137	0.349588	-1.12E-04	1.42

6.4 Two-dimensional Examples

6.4.1 The Azmy Benchmark Problem

This benchmark problem consists of a two-region, one group, deep-penetration problem and was developed by Azmy [54]. The geometry and corresponding cross sections of the problem is shown in Figure 6.12. The dashed lines in Figure 6.12 are located at $x=5.84375$, 7.84375 , and 9.84375 cm, respectively, and we analyze the scalar flux along these lines for the solution convergence. All the calculations for this problem were performed up to the P_{11} approximation since higher-order angular approximations provided little effect in the solution. The reference solution was computed by the EVENT calculation with a very fine mesh (43372 elements and 21885 nodes). The scalar flux of this problem is shown in Figure 6.13. Due to the large absorption cross section in the outer region, the flux exhibits a large gradient along the material interface.

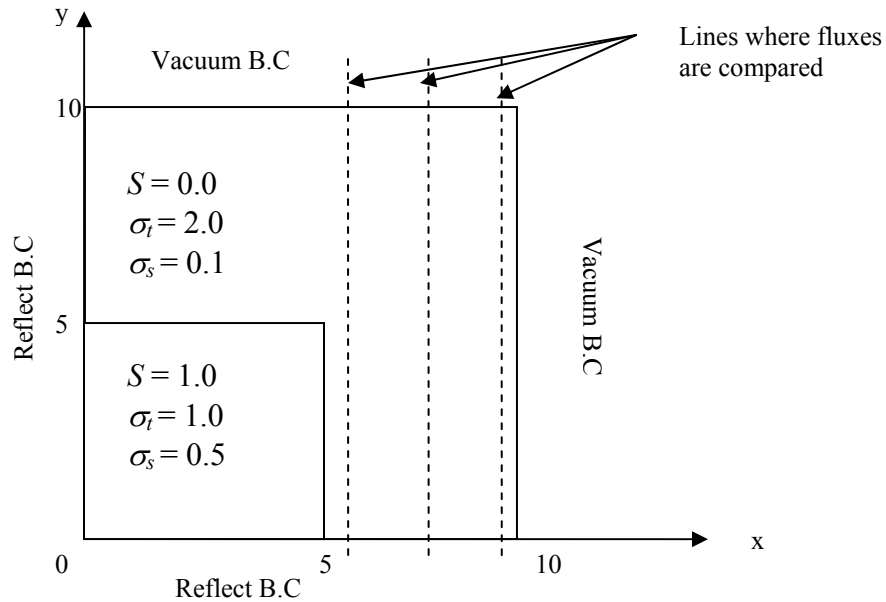


Figure 6.12: Problem schematic of Azmy benchmark problem

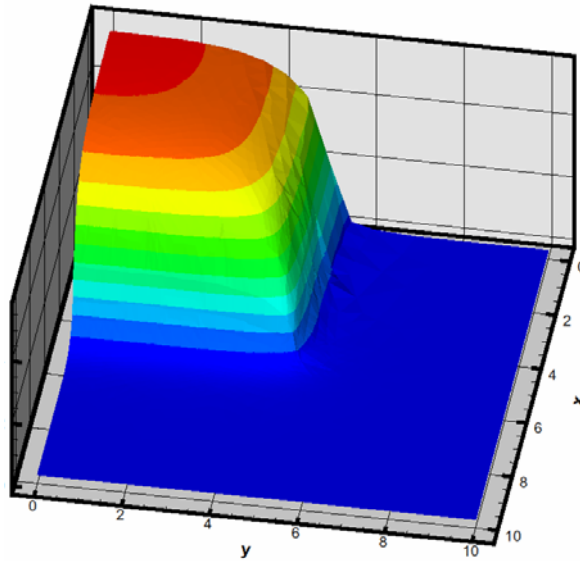


Figure 6.13: Flux profile for Azmy benchmark problem

The scalar flux varies more than 8 orders of magnitude for this problem. This large difference in the gradient produces the difficulty of applying the adaptivity algorithm based on the global norm since the large relative error of the very low flux region has virtually no effect on the overall accuracy. A representative final mesh based on the global L_2 error norm is shown in Figure 6.14. The adaptive strategy successfully refined the mesh along the large flux gradient regions; however, this mesh failed to produce an accurate flux profile along the lines of interest.

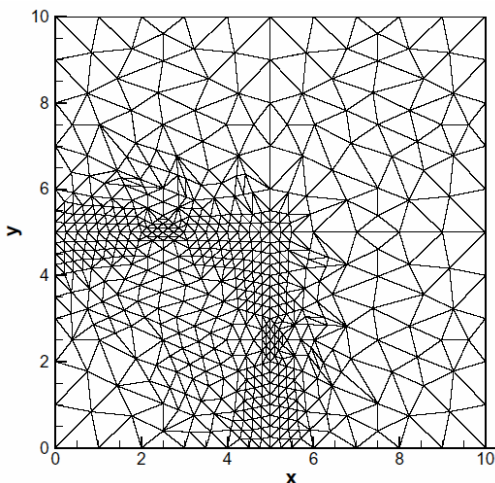


Figure 6.14: Illustration of the adaptively refined mesh based on the global L_2 norm

To remedy this difficulty, we employed the goal-oriented adaptivity with the Gaussian source distributed along the dashed lines in Figure 6.12. The adjoint source term in this case can be expressed by the following formula:

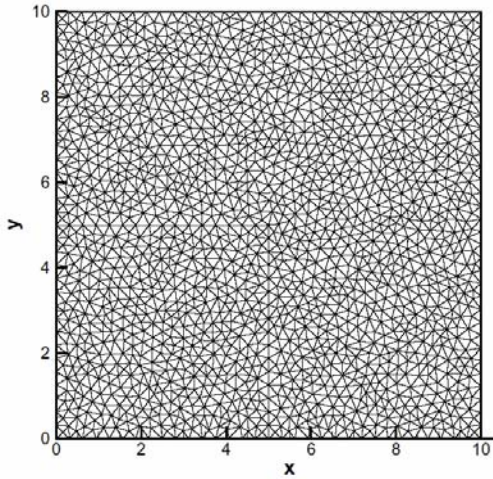
$$S^{+*}(x, y) = \frac{e^{-(x-x_0)^2/2\sigma^2}}{\sigma\sqrt{2\pi}} \quad (6.53)$$

where, x_0 is the source center, σ is the standard deviation of the Gaussian - a value of 0.25 was adopted for the purpose of the calculations.

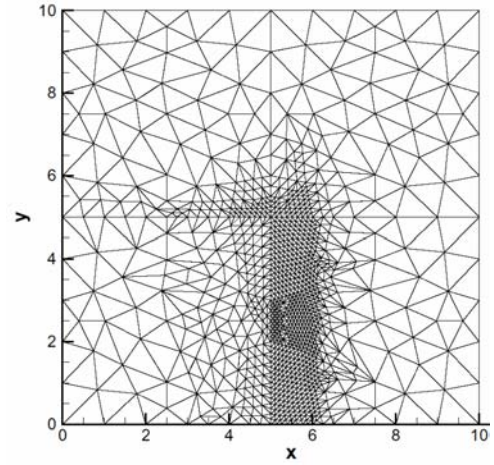
6.4.1.1 Flux Comparison at $x = 5.84375\text{cm}$

The distance between the target location and the source region is the shortest of all three cases considered; therefore we expect the convergence in the solution to be readily obtained. From the series of EVENT calculations, we observe that this is indeed the case. The two meshes shown in Figure 6.15 are the final meshes produced by the goal-oriented adaptivity (right) and uniform refinement (left). As expected, the adaptive refinement mainly produced mesh concentration between the source and target regions and remained relatively coarse elements elsewhere. This had been expected since the goal-oriented adaptivity utilizes the error measure which is a product between the forward and adjoint errors.

We assess the adaptive mesh refinement by comparing the scalar flux against the reference solution. Figure 6.16 depicts the scalar flux plots produced by the different meshes. Large oscillations are observed for the uniform mesh up to 3462 elements, while the solutions of adaptively refined meshes are indistinguishable from the reference solution even with the smallest number of elements (801 elements). The tolerances of the adaptive calculations were chosen to be 0.5 and 0.1, which have produced a total of 801 and 2056 spatial finite elements, respectively.



(a) uniform mesh
(3462 elements, 1764 nodes)



(b) adaptive mesh
(2056 elements, 1045 nodes)

Figure 6.15: Illustrative final mesh produced by goal-oriented adaptivity (3362 elements, 1705 nodes)

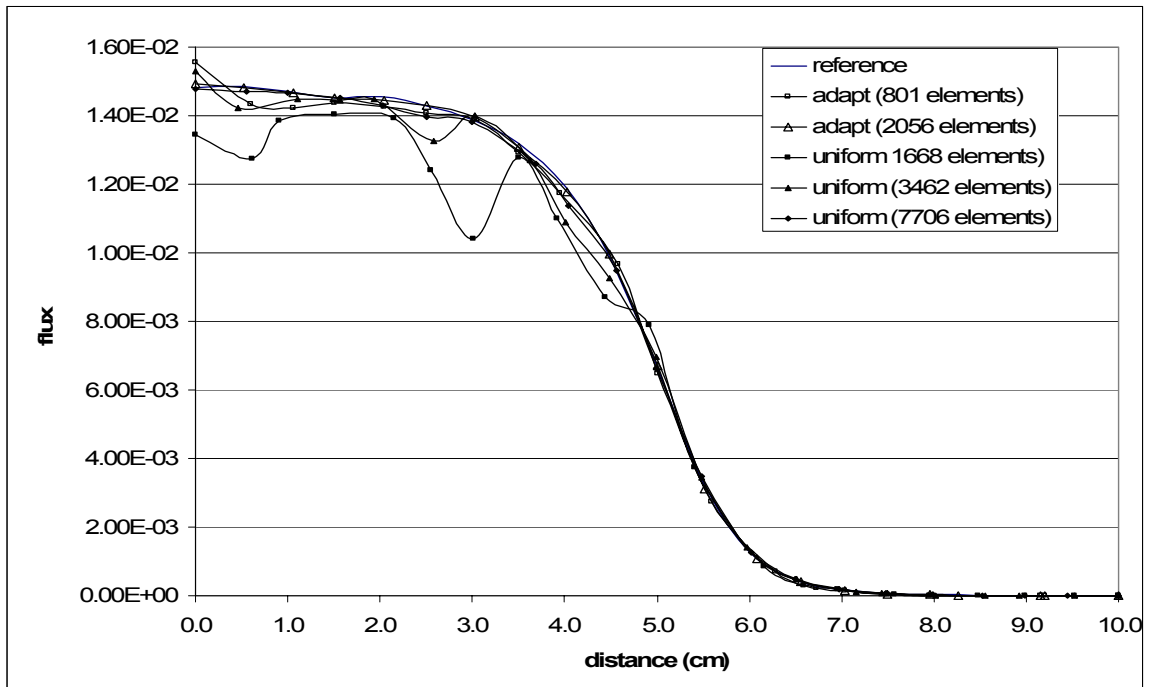


Figure 6.16: Scalar flux plot along $x=5.84375\text{cm}$

Table 6.12 presents the computed L_∞ errors and the total DoFs used in each computation. The L_∞ errors for the adaptive solutions are about a five times smaller than ones for the uniform mesh solutions, and in order to achieve a comparable accuracy, the uniform mesh required three times more nodes. Comparison of the total DoFs used in each case reveals the additional advantage of the adaptive method. The last column of Table 6.12 presents the total number of DoFs used in the each calculation. The numbers in parenthesis in the adaptive refinement cases presents the total number of the DoFs without the angular order truncation. The total DoFs of the converged solution were reduced about a factor of 5 for the adaptive refinement for a similar accuracy.

Finally, the distribution of the angular expansion orders used for the adaptive computation is shown in Figure 6.17. The tolerance in the angular truncation error was set as the $1/100^{\text{th}}$ of the spatial tolerance. As we conducted the experiments with various sets of spatial and angular tolerances, this factor of $1/100^{\text{th}}$ seemed to perform the best for most of the cases. We observe that higher-order angular expansions were required at the material interface, and surrounding regions. The rest of the regions required lower angular expansion orders, especially those further away from the source regions.

Table 6.12: Comparison of total degrees of freedom in uniform and adaptive calculations 1

# of Elements	# of Nodes	L_∞ Error w.r.t. reference	DoFs used
Uniform mesh			
1668	867	3.94×10^{-3}	31212
3462	1764	1.06×10^{-3}	63504
7706	3902	5.49×10^{-4}	140472
Adaptive Mesh			
801	414	7.46×10^{-4}	5375(14904)
2056	1045	2.76×10^{-4}	25091(37620)

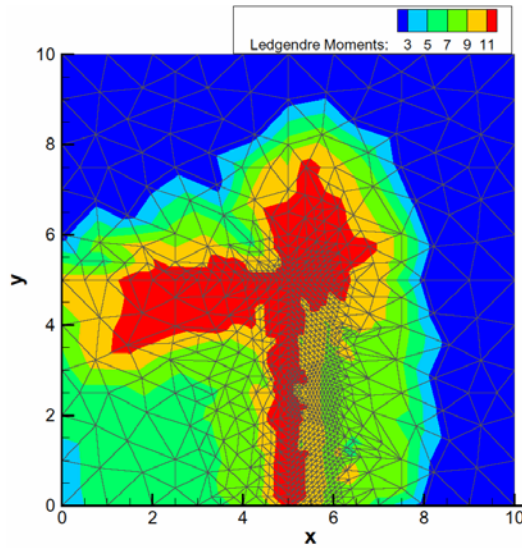


Figure 6.17: Distribution of the angular moments used for the goal-oriented adaptivity applied at $x = 5.84375$ cm

6.4.1.2 Flux Comparison at $x = 7.84375$ cm

The scalar flux along this line is depicted in Figure 6.18. The spatial tolerances adopted were 5.0×10^{-3} and 1.0×10^{-4} for the presented adaptive results, resulting in a total of 1511 and 4517 elements, respectively. Again, the oscillations are observed in the uniform mesh (1668 and 7706 spatial elements) case, and this time the adaptive mesh (1511 elements) case also exhibits smaller, but noticeable oscillations. Caused by the further distance from the source region, the effectiveness of the adaptive refinement is not as efficient as the previous case. Elements with smaller sizes were assigned to a large fraction of the system, and relatively uniform spatial meshes were required to solve this problem (see Figure 6.19).

Table 6.13 lists the computed L_∞ errors for each calculation. We can observe slightly more accurate results for the adaptive calculations compared to the uniform mesh calculation for a similar number of spatial elements. On the other hand, the effectiveness of the adaptive algorithm is still prominent (a factor of 3~5) if the total DoFs, listed in the

last column of Table 6.13, are compared. The spatial distribution of the angular order used in the adaptive calculation and a representative final adaptive mesh is shown in Figure 6.19. Again, higher-order angular expansions were required for the region between source and detector locations.

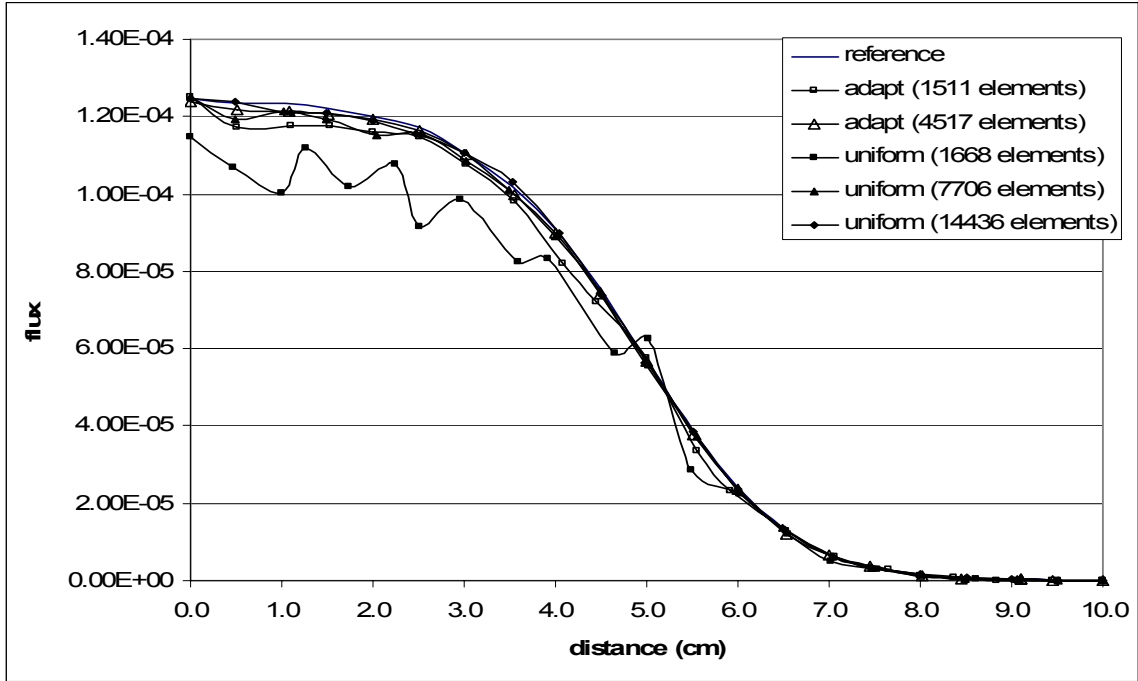


Figure 6.18: Scalar flux profiles along $x=7.84375\text{cm}$

Table 6.13: Comparison of total degrees of freedom in uniform and adaptive calculations 2

# of Elements	# of Nodes	L_∞ Error w.r.t. reference	DoFs used
Uniform mesh			
1668	867	2.53×10^{-5}	60048
7706	3092	4.95×10^{-6}	14072
14436	7351	2.00×10^{-6}	26436
Adaptive Mesh			
1511	772	8.23×10^{-6}	14377(27792)
4517	2283	3.54×10^{-6}	49425 (82188)

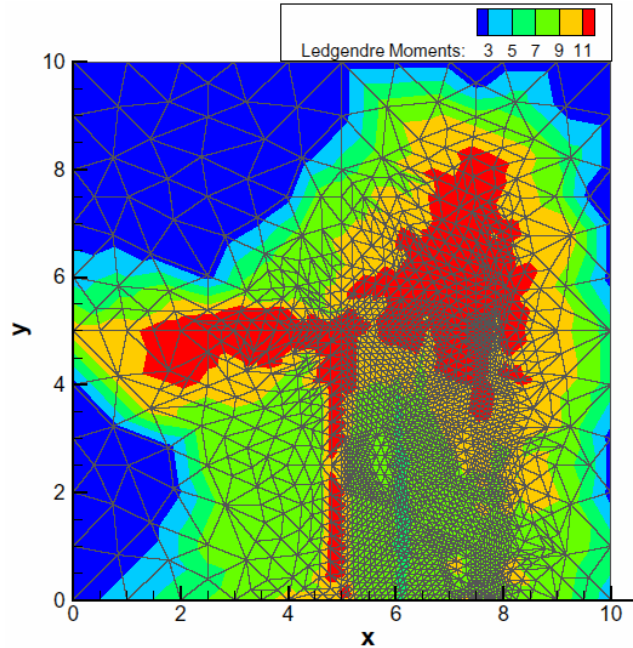


Figure 6.19: Final Adaptive mesh and the distribution of the angular orders used in the adaptive mesh refinement for the comparison at $x = 7.84375$ cm

6.4.1.3 Flux Comparison at $x = 9.84375$ cm

This location is at the edge of the system and the magnitude of the scalar flux has dropped by a rather large factor; therefore it is difficult to obtain the accurate solutions. Since the source and target regions are located at opposite ends of the system, we expect further degrading in the effectiveness of the goal-oriented adaptive. Figure 6.20 depicts the flux profile of the calculations. The tolerances of the adaptive algorithm were prescribed as 1.0×10^{-4} and 2.0×10^{-5} , which resulted in a total of 1870 and 13570 spatial elements, respectively. As expected, a similar accuracy was obtained by the solutions with the uniform meshes compared to ones with the adaptive meshes. The representative final meshes for both uniform and adaptive calculations are depicted in Figure 6.21. We can observe that around 3/4 of the system was covered by the adaptively refined elements.

Table 6.14 summarizes the results for this test case, and the distribution of the angular expansion orders is shown in Figure 6.22. The boundary of the higher-order angular expansions is located along the shortest line that connects the source to the corner points (i.e. (5.0, 5.0) to (10.0, 10.0) cm). The reason is clear: the product of the adjoint and forward solution produces the region of higher importance in the lower portion of this line. The overall DoFs difference between the uniform and adaptive mesh is still about a factor of 2, which continues to indicate the advantage of the adaptive angular refinement.

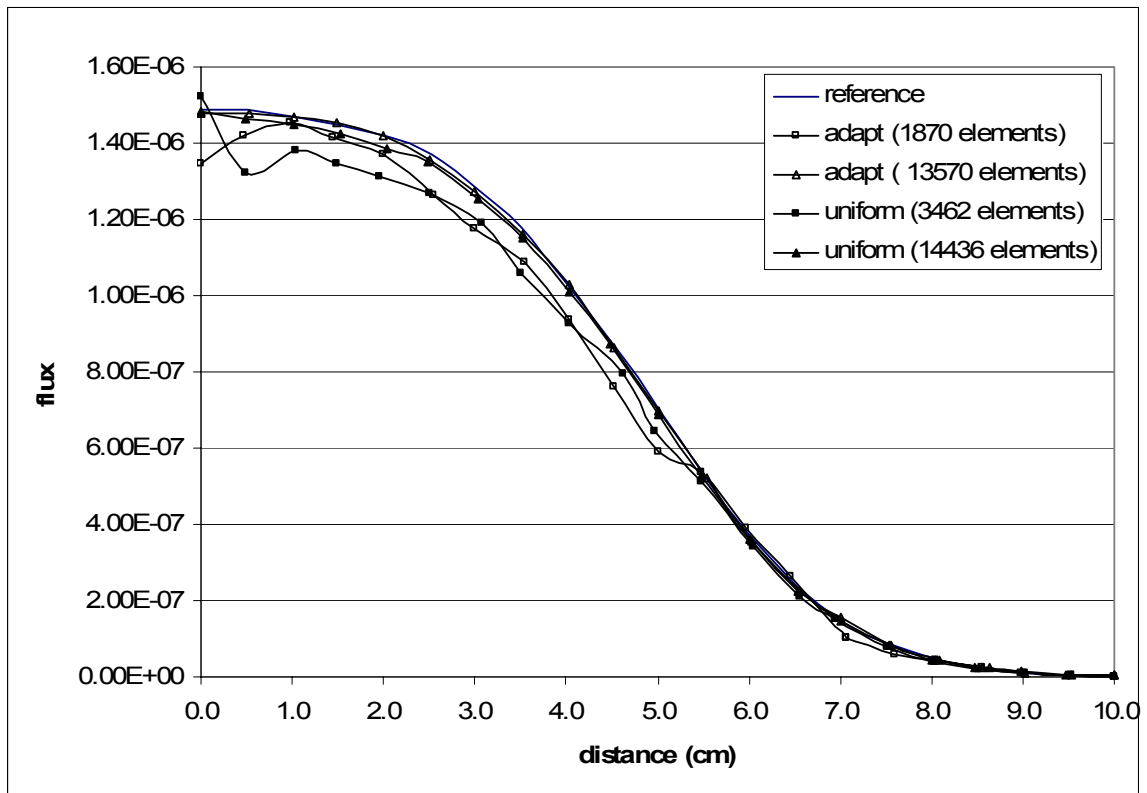
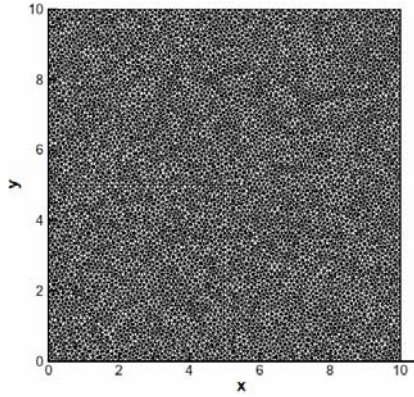
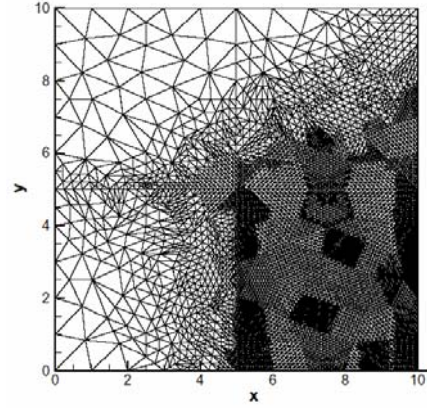


Figure 6.20: Scalar flux profile along $x = 9.84375$ cm



(a) uniform mesh (14568 elements)



(b) adaptive mesh (13570 elements)

Figure 6.21: Final uniform and adaptive mesh

Table 6.14: Comparison of total degrees of freedom in uniform and adaptive calculations 3

# of Elements	# of Nodes	L_∞ Error w.r.t. reference	DoFs used
Uniform mesh			
3462	1764	1.65×10^{-7}	63504
14436	7351	3.52×10^{-8}	264636
Adaptive mesh			
1870	954	1.47×10^{-7}	20133(34344)
13570	6827	1.73×10^{-8}	196717(245772)

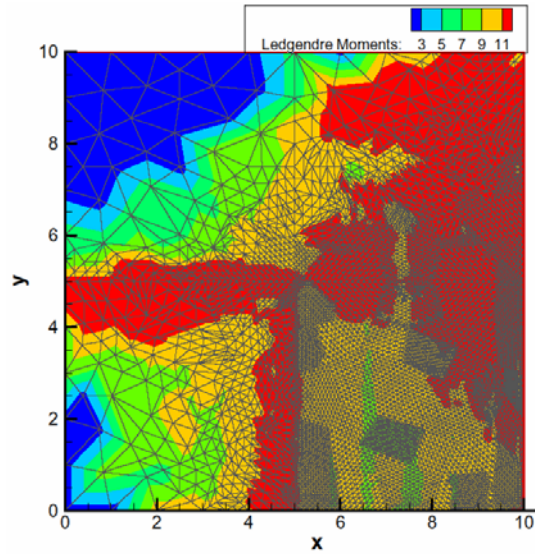


Figure 6.22: Adaptive mesh and distribution of angular moments for the comparison at $x = 9.84375$ cm

6.4.2 Simple 2-Group Eigenvalue Problem

Our next two dimensional example is a multigroup eigenvalue problem. This is a two-group problem and consists of two homogeneous core regions surrounded by a reflector [55]. The geometrical configuration for this problem is shown in Figure 6.23, and corresponding two group cross sections are listed in the Table 6.15. The purpose of this problem is to illustrate how the adaptive mesh differs between groups and how it affects overall solution.

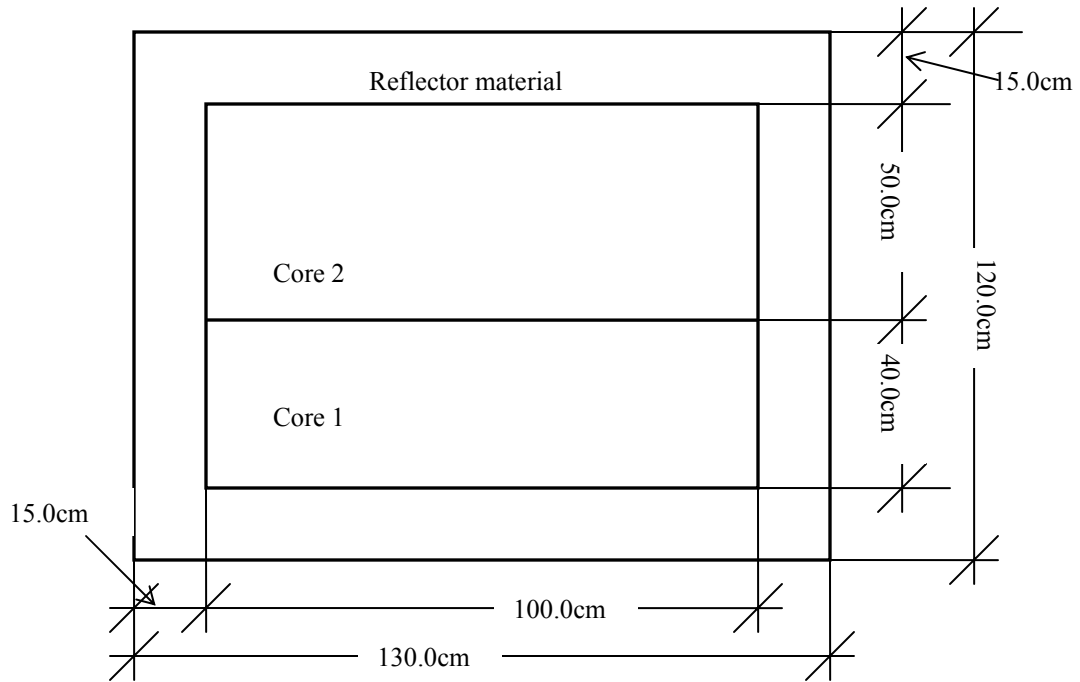


Figure 6.23: Schematics of the two-group eigenvalue problem

Table 6.15: Material cross sections of the two group eigenvalue problem (in cm^{-1})

	Core1		Core2		Reflector	
	Group1	Group2	Group1	Group2	Group1	Group2
σ_t	0.2631	0.9416	0.2604	0.8333	0.2950	2.0080
σ_a	0.0121	0.1210	0.0100	0.1000	0.0004	0.0200
$\nu\sigma_f$	0.0085	0.1851	0.0060	0.1500	0.0000	0.0000
χ	1.0000	0.0000	1.0000	0.0000	--	--
σ_s	σ_{s11}		σ_{s11}		σ_{s11}	
	0.2269		0.2344		0.2453	
	σ_{s12}	σ_{s22}	σ_{s12}	σ_{s22}	σ_{s12}	σ_{s22}
	0.0241	0.8206	0.0160	0.7333	0.0493	1.9880

The physics that drives this problem is the fission source in the core regions and the down scatter source in the reflector region. This produces significantly different flux profiles between the two groups. Figure 6.24 illustrates the flux profiles for this problem.

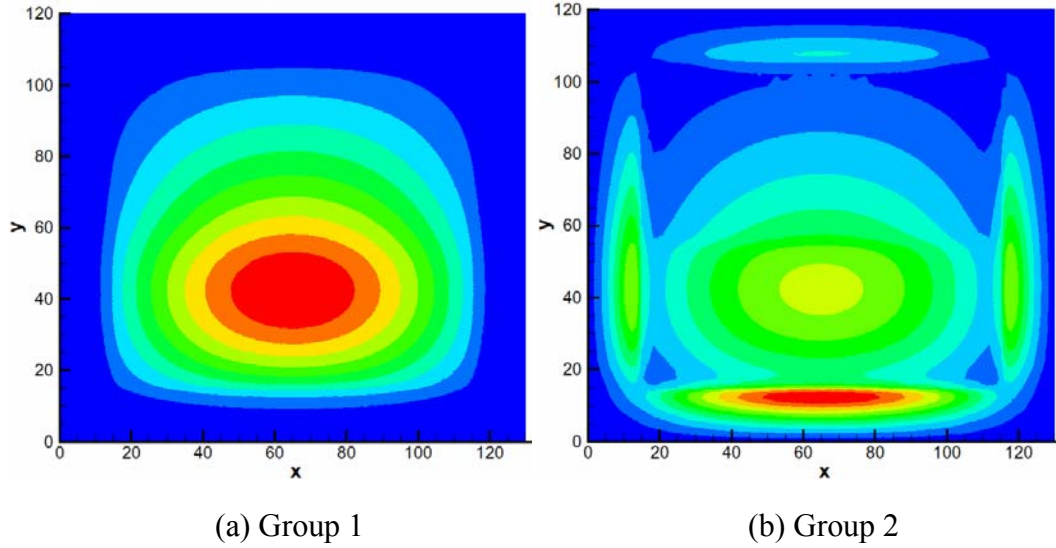
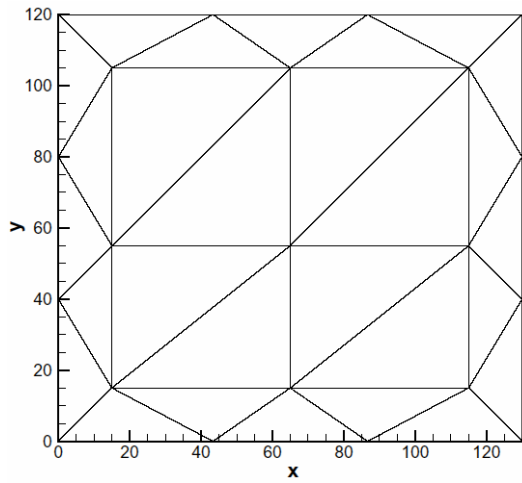


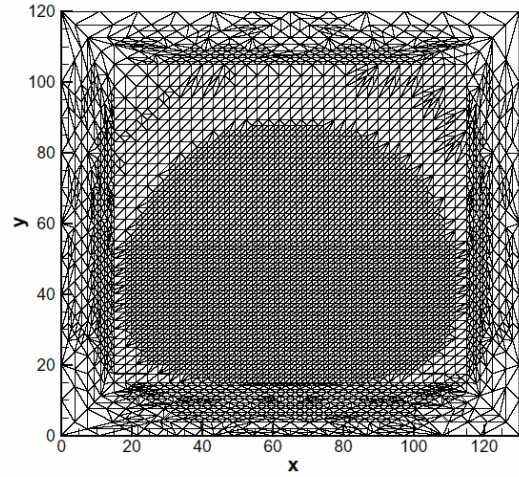
Figure 6.24: Flux profile of the two-group eigenvalue problem

Because of the difference in the flux profiles, we expect the adaptive mesh refinement to produce the different results in each group. Figure 6.25 shows the initial and final meshes of the diffusion approximation created using different error indicators. The adaptive mesh reflects the difference in physics of the groups. Figure 6.25(b) shows the adaptive meshes based on the error in the both groups, which somewhat shows the combination of Figure 6.25(c) and (d) as we expected.

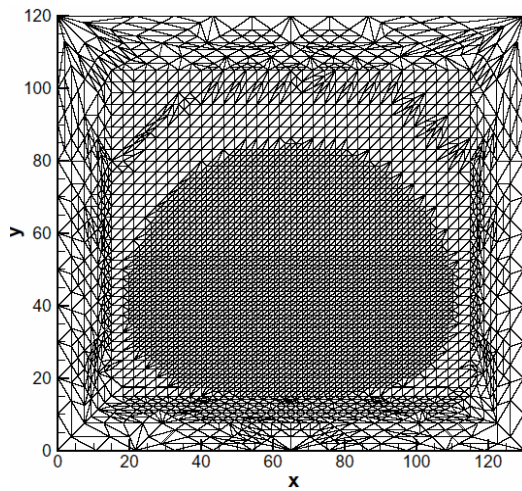
In order to see the effect in the solution due to the different adaptive meshes, the number of nodes used for the diffusion approximation solution was compared. The number of the nodes required to converge the effective multiplication constant (k_{eff}) within the 0.01% of converged value ($k_{eff} = 1.1422$) were 2250, 1778 and 1538 for the error measure based on the first group, second group and both groups, respectively. The differences in the number of nodes are not significant; a relatively large number of nodes required for the first group originates from the failure of approximating accurate thermal sources around the reflector regions. In order to ensure that all the physics is covered with one error measure, we employ an error measure which is a sum of all groups.



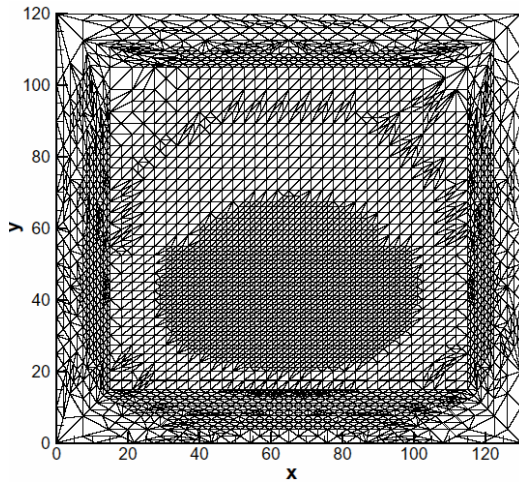
(a) initial mesh



(b) final mesh of adaptivity based on both groups



(c) final mesh based on group 1 error



(d) final mesh based on group 2 error

Figure 6.25: Initial and final mesh for the two-group eigenvalue problem

Secondly, we have assessed the convergence behavior of the k_{eff} in terms of number of nodes used in both uniform and adaptive meshes. Figure 6.26 depicts the percent difference in k_{eff} from the converged values. In order for k_{eff} to converge within 0.01%, the uniform refinement case has required about a factor of 6 more nodes than the adaptive meshes (8717, and 1538 nodes, respectively). This problem is relative large in

size, and the important region is somewhat localized; thus, the adaptive strategy shows a greater effect in the mesh refinement.

The difference in the total number of nodes between uniform and adaptive mesh produces a considerable gain in computational time. For example, the k_{eff} converges to the 1.1435 in for a P_9 approximation. To obtain the k_{eff} within 0.01% of this converged value, the adaptive method took 33.5 seconds, while the uniform mesh case took 185.7 seconds. As we see here, the reduction in the number of nodes directly reflects the computational time.

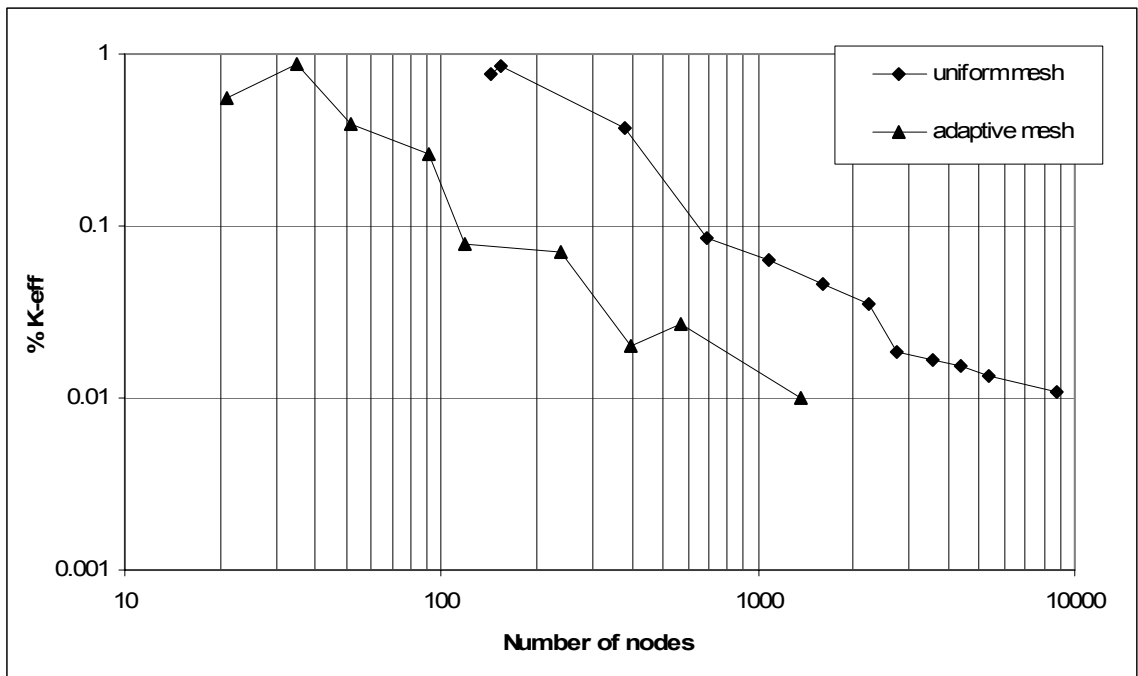


Figure 6.26: The % k_{eff} difference versus number of nodes

6.4.3 Gamma Transport in the Simple Fuel Cask Problem

The last test problem is a 2D, x-y geometry deep-penetration problem with 20 gamma energy groups. The problem consists of a circular quadrant with 80cm radius and three distinct materials (fuel, water and steel) creating a total of five regions. The problem geometry is shown in the Figure 6.27. The cross section library used was the BUGLE library which has been used extensively for light water reactor shielding and reactor pressure vessel dosimetry studies[56]. The detailed cross section used in this problem is listed in Appendix. An isotropic source of strength 0.1 was defined for all the groups.

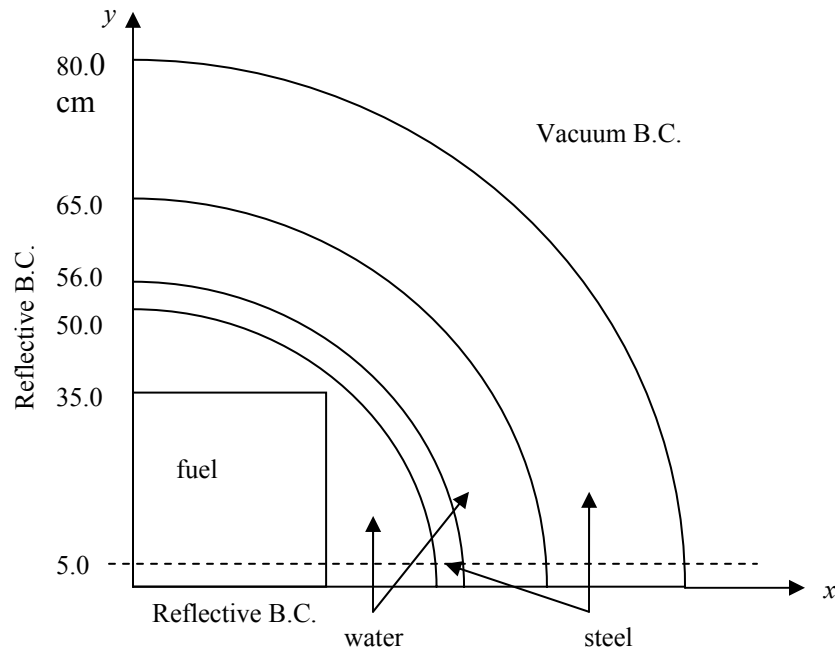


Figure 6.27: Geometry of the gamma transport problem

The relatively wide range of the energy spectrum (14MeV for group 1 and 2keV for group 20) provides significantly different radiation flux profiles for the energy groups. Our analysis concentrated on assessing the accuracy of groups 1, 17 and 20 since those three groups exhibit the distinct flux distributions. The flux profiles are depicted in Figure 6.28(a), (b) and (c).

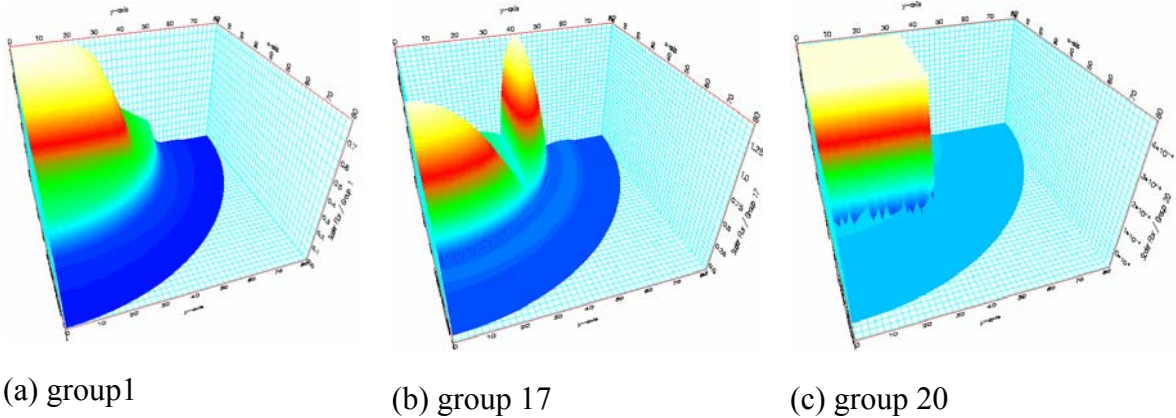


Figure 6.28: Flux profile for the gamma transport problem

We limited the order of the expansion to the P_5 approximation in all the calculations since higher-order angular expansions showed a negligible effect on the accuracy of the solution. The reference solution was again obtained by a fine mesh EVENT calculation (41762 elements and 21060 nodes). In order to confirm the accuracy of the solutions, we compared the scalar flux along $y = 5.0\text{cm}$. Figure 6.29 shows the scalar flux profile of group 1 computed by the reference, adaptive and uniform mesh resolutions. It is clear that the relatively small number of elements (986 and 950 elements for the adaptive and uniform mesh, respectively) can reproduce fairly accurate results. Since the solution is relatively smooth throughout the domain, large spatial elements can successfully produce acceptable results. The spatial tolerances adopted were 1.0×10^{-3} for the presented adaptive computations, which resulted in a total of 986 elements.

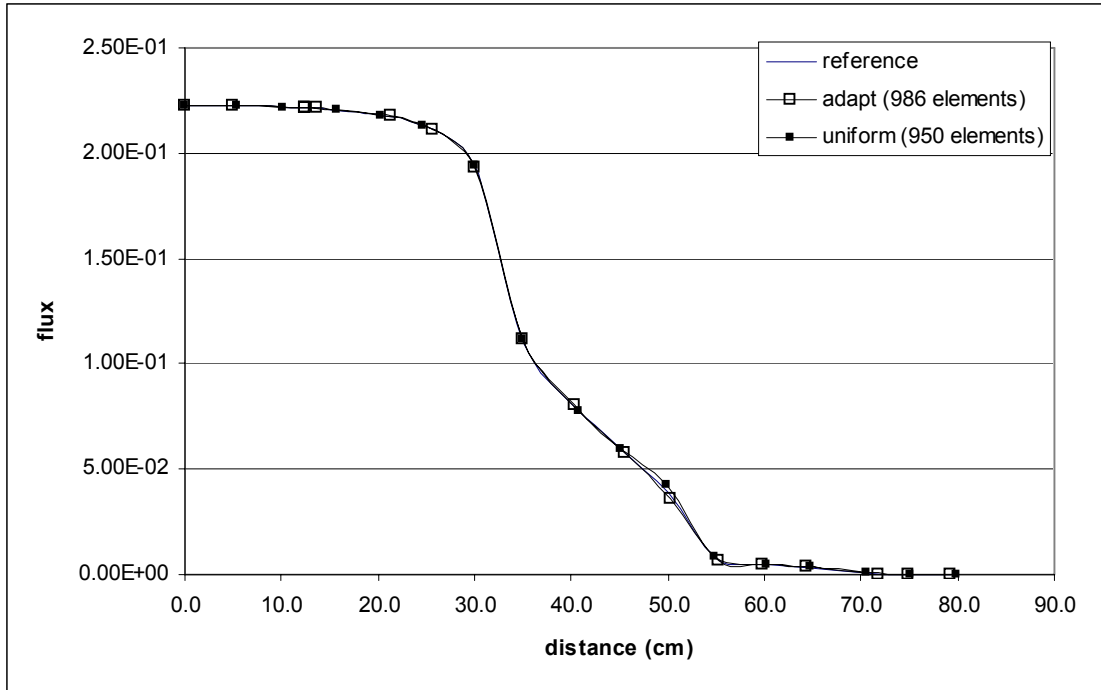


Figure 6.29: Group 1 scalar flux profile of the gamma transport problem at $y = 5.0\text{cm}$

The group 17 scalar flux is depicted in Figure 6.30. This group has a sharp flux gradient and a peak flux near $x = 40.0\text{ cm}$. Considering this type of flux shape, we expect the adaptive mesh refinement to have a great advantage since a highly resolved solution is required to accurately model a narrow, sharp flux peak. The peak flux of 4.56009×10^{-1} was obtained by the reference calculation. The computed peak flux values for the uniform and adaptive mesh cases are summarized in Table 6.16. The last column of Table 6.16 presents percent differences in the peak flux with respect to the reference solution. A considerable improvement in the peak flux accuracy was obtained by the adaptive computations, especially in the finer mesh case. For the coarser mesh cases, the accuracy is improved by a factor of 2. A total of 8584 elements were required to achieve a 1.0% difference in the peak flux for the adaptive calculations, while the uniform mesh solution with 217712 elements still gave a 2.34% error. The spatial tolerances of 1.0×10^{-5} and 1.0×10^{-6} were used to produce 3746 and 8584 adaptive elements.

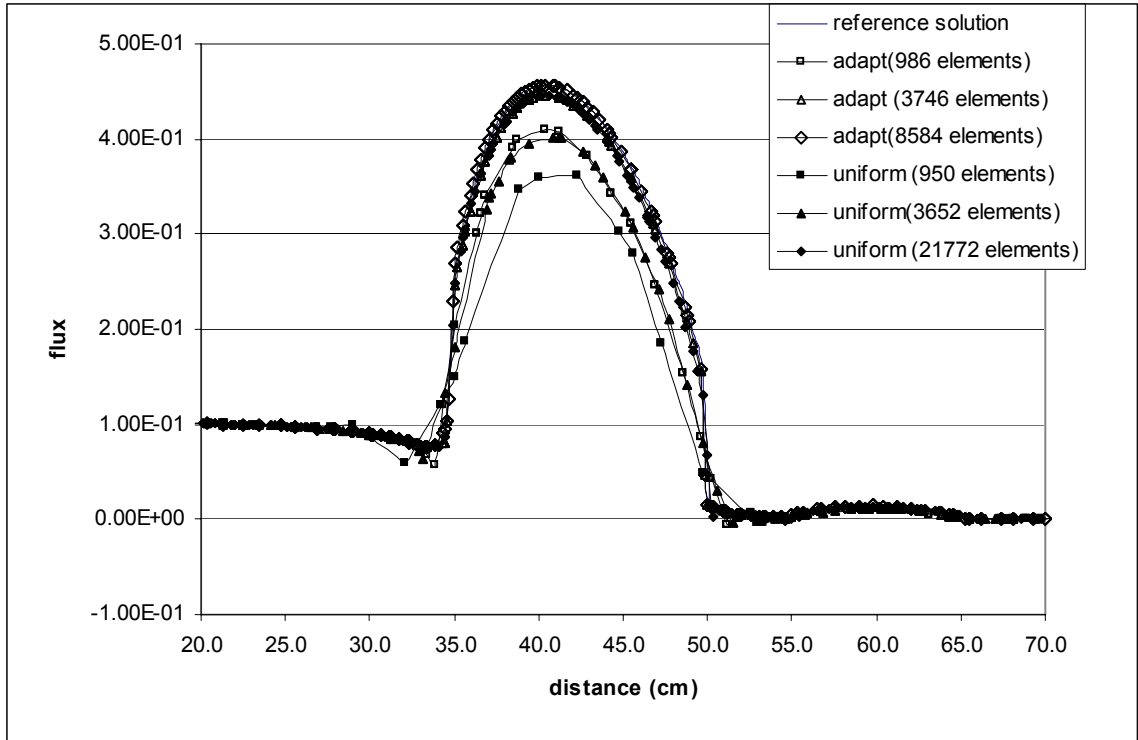


Figure 6.30: Group 17 scalar flux profile of the gamma transport problem at $y = 5.0\text{cm}$

**Table 6.16: Comparison of the peak flux values for group 17
(Reference peak flux = 4.56009×10^{-1})**

Number of Elements	Peak Flux	% Difference w.r.t reference.
Uniform Mesh		
950	3.613×10^{-1}	26.2%
3652	4.021×10^{-1}	13.4%
21772	4.456×10^{-1}	2.34%
Adaptive Mesh		
986	4.103×10^{-1}	11.16%
3746	4.379×10^{-1}	4.15%
8584	4.565×10^{-1}	0.10%

The last comparison discussed is that for group 20. In this group, the magnitude of the cross section is relatively larger and therefore a steep gradient in the flux is observed along the interface between the fuel and water regions. The flux profile of this

group is shown in Figure 6.31. Unphysical oscillations and negative fluxes are produced across the material interface when the relatively coarser mesh sizes are employed. A total of 3746 elements were required to eliminate the oscillations by the adaptive algorithm, while the uniform mesh calculation with 12270 elements still produced a small, but distinguishable negative flux.

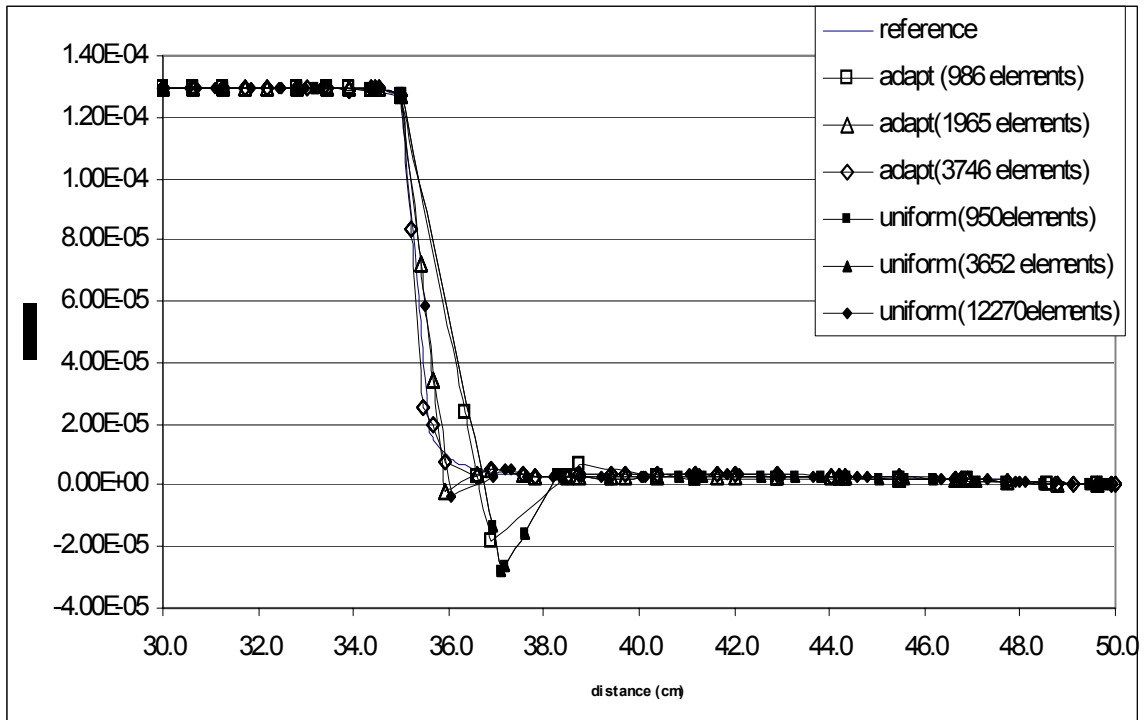


Figure 6.31: Group 20 scalar flux profile of the gamma transport problem at $y = 5.0\text{cm}$

The angular expansion orders used for each group differ drastically due to the wide range of the energy spectrum (~ 4 orders of magnitude). We expect that groups at the higher energy range to produce an anisotropic forward-peaked angular flux, while the groups in the keV range to produce an relatively isotropic flux. Therefore, higher-order angular expansion orders are expected for the group 1 throughout the system, while the required angular orders are reduced gradually with decreasing energy range. Examining the angular distributions presented in Figure 6.32, we can see that this is indeed the case. Group 1 required the P_5 approximations in almost all regions while group 20 required

higher order approximations only at the material interface between the fuel and water regions.

Lastly, the total number of DoFs used for the each uniform and adaptive calculation are summarized in Table 6.17. The last column in Table 6.17 presents the total CPU time required for each run. Clearly, the adaptive computation requires a longer CPU time for similar number of elements; however, since a similar accuracy can be obtained by the much smaller number of DoFs, the computational time is effectively reduced by more than a factor of two.

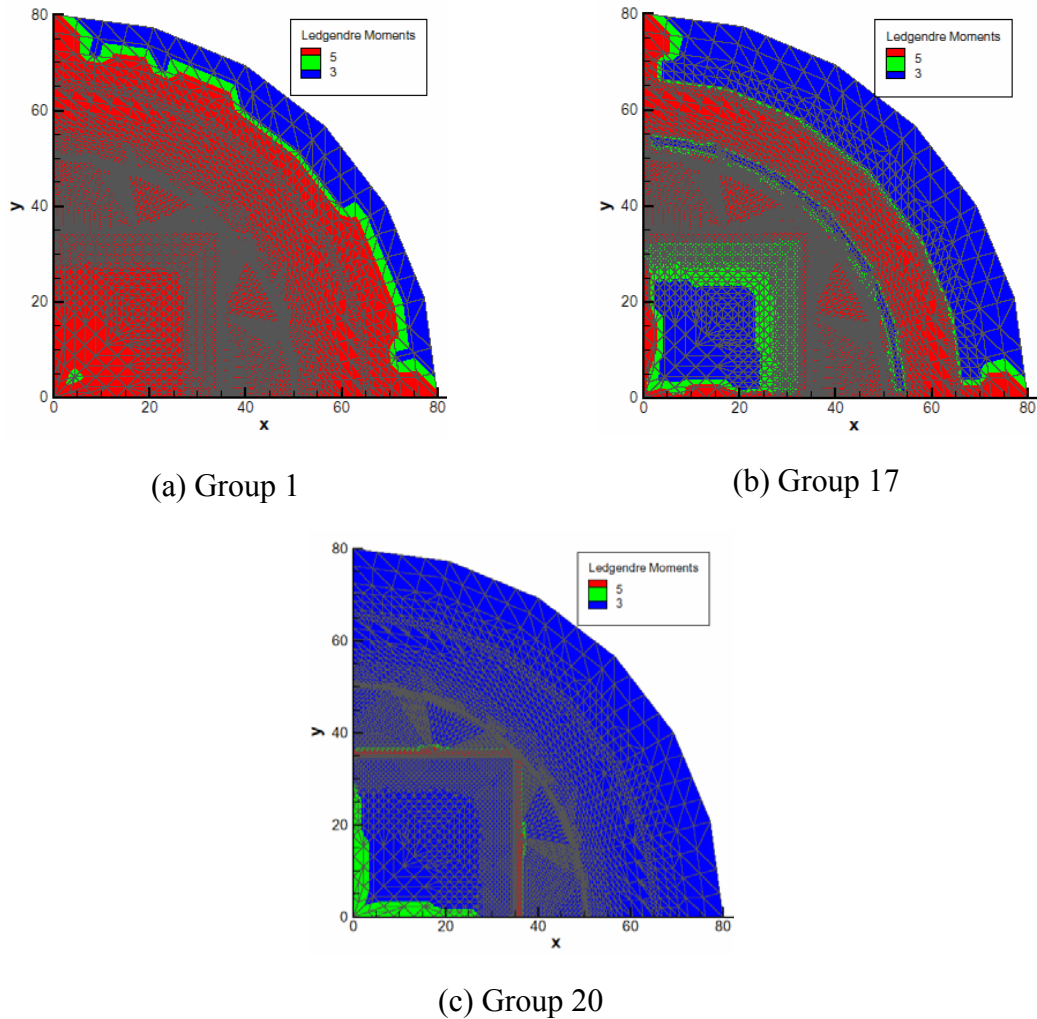


Figure 6.32: Angular expansion orders distribution for the gamma transport problem for group 1, 17 and 20

Table 6.17: Summary of the gamma transport problem

Number of Elements	Number of Nodes	Total DoFs Used	CPU time (sec)
Uniform Mesh			
950	504	90720	2.0
3652	1883	338940	10.5
21722	11065	1991700	135.2
41762	21060	3790800	318.6
Adaptive Mesh			
968	505	55729 (90900)	7.4
3746	1913	277952 (344340)	18.1
8584	4354	684334 (783360)	138.5

CHAPTER 7

CONCLUSIONS

“Efficiency” and “accuracy” are the two key aspects for successful computational simulations. These two aspects must go hand in hand; however, at a first glance, the simultaneous fulfillment of these conditions is not attainable since they appear to have opposite requirements. The strong theoretical and mathematical framework developed over a last few decades together with the rapid advancements in computer hardware technologies has bridged the two aspects by means of adaptive mesh refinement strategy. Furthermore, it has demonstrated great successes in modeling large, complex problems.

In this thesis, a self-adaptive numerical framework for the neutral particle radiation transport problem was developed based on the residual *a posteriori* error analysis. The spatial and angular discretization errors were successfully separated by initially seeking the spatial convergence for a given angular resolution, and subsequently employing a higher-order projection of the spatially converged solution to evaluate the angular truncation error. By utilizing an arbitrary adjoint source, (near) optimal discretization, tuned to minimizing the error in the target engineering output, was accomplished. The simple verification step via the Method of Manufactured Solution has demonstrated the accuracy of the developed error estimators. The extra computational overhead, which stems from an iterative mesh refinement process, is rewarded by the (near) optimum mesh generation. Consequently, the methodology has provided the speed-up in the total computational time for most of the example problems presented.

7.1. Recommendations for Future Work

A number of improvements can lead to more practical application of the developed methodology. The following is a list of possible steps for accomplishing this.

(i) Extension to three-dimensional and curvilinear geometry

Adapting the methodology to the more general three dimensional framework is considered as the immediate next step. The mathematical framework developed in this thesis is based on the general Cartesian geometry; therefore, it should extend naturally to x - y - z geometry. Refinement procedure in three dimensions is still an active area of research, and efficient mesh refinement algorithms must be considered for successful implementations. *A posteriori* error analysis for curvilinear geometry such as r - z geometry also needs to be developed. However, the basic adaptive strategy should be applicable even in this case.

(ii) Rigorous mathematical development for the non-selfadjoint problem

In this thesis, transport problems were treated as the series of one-group problems; the group couplings through the scattering source were assumed to give a negligible contribution to the error. This somewhat ad-hoc assumption seemed to work well for the examples presented here. Nonetheless, more rigorous mathematical support should bring the developed adaptive methodology to the next stage. This can be achieved by means of the full phase-space adaptivity, which includes space, angle and energy variables.

The theoretical analysis of the non-selfadjoint problem also becomes guidance for developing the adaptive framework for the first-order transport equation. The extension of adaptivity to non-hierarchical angular discretizations such as the method of discrete ordinates should also be considered.

(iii) Parallel implementation of the goal-oriented adaptivity

The goal-oriented adaptivity utilizes the adjoint problem, which successfully produced the optimum mesh tuned to the desired output. The drawback is that the methodology has simply doubled the computational cost due to the requirement of the adjoint problem. This extra computation may hold back the practical application of the method. However,

the forward and adjoint problem are essentially two separate problems; thus, the problems can be solved by employing parallel computations practically with zero cost of the extra complexity and communication time.

(iv) Hierarchical self-adaptive multilevel framework

For real-life engineering problems, problem size and complexity can become prohibitively large regardless of optimal discretizations. Thus, the solution procedure at the finest level is clearly demanding, and obtaining the converged solution at this level is not feasible without efficient solution algorithms. The hierarchical self-adaptive multilevel framework is the only way forward to accomplish this difficult task. Over the years, multi-level methods have gained the recognition as the most efficient scalable solution algorithms. We can take advantage of the hierarchical structure of the adaptive mesh to develop the general multi-level solution framework.

APPENDIX A

CROSS SECTIONS USED IN GAMMA TRANSPORT PROBLEM

Table A.1: 20 group cross sections of the fuel material

Group 1	σ_{t1}	σ_{a1}		
	1.2856436E-01	4.3248954E-05		
	$\sigma_{sg \rightarrow g'} \quad g'=g, 20$			
	2.2837829E-03	5.6071030E-03	2.9095791E-03	3.0620040E-03
	3.3177622E-03	3.7471522E-03	4.5031784E-03	5.9969765E-03
	4.1288515E-03	5.7492843E-03	3.1569758E-03	1.8927923E-03
	2.1917925E-03	1.4023727E-01	6.9466843E-03	0.0000000E+00
	0.0000000E+00	0.0000000E+00	0.0000000E+00	0.0000000E+00
Group 2	σ_{t2}	σ_{a2}		
	1.2888166E-01	5.4084019E-05		
	$\sigma_{sg \rightarrow g'} \quad g'=g, 20$			
	3.6522681E-03	4.1208514E-03	4.2224494E-03	4.4465577E-03
	4.8766779E-03	5.6946524E-03	7.3904363E-03	5.0106659E-03
	6.9243545E-03	3.7902410E-03	2.2712543E-03	2.6302999E-03
	1.2363637E-01	8.4808599E-03	0.0000000E+00	0.0000000E+00
	0.0000000E+00	0.0000000E+00	0.0000000E+00	
Group 3	σ_{t3}	σ_{a3}		
	1.2971906E-01	6.5101674E-05		
	$\sigma_{sg \rightarrow g'} \quad g'=g, 20$			
	3.3515934E-03	5.6319521E-03	5.7833781E-03	6.1708027E-03
	7.0037660E-03	8.8460753E-03	5.8971862E-03	8.0781011E-03
	4.4044689E-03	2.6371044E-03	3.0536975E-03	1.0945316E-01
	1.0003947E-02	0.0000000E+00	0.0000000E+00	0.0000000E+00
	0.0000000E+00	0.0000000E+00		
Group 4	σ_{t4}	σ_{a4}		
	1.3267206E-01	8.1294333E-05		
	$\sigma_{sg \rightarrow g'} \quad g'=g, 20$			
	2.6106711E-03	8.1065213E-03	8.3453190E-03	9.1025606E-03
	1.1038194E-02	7.1625458E-03	9.6683037E-03	5.2347453E-03
	3.1286515E-03	3.6211477E-03	9.5254652E-02	1.2116414E-02
	0.0000000E+00	0.0000000E+00	0.0000000E+00	0.0000000E+00
	0.0000000E+00			

Table A.1: Continued

Group 5	σ_{t5}	σ_{a5}		
	1.3615146E-01	9.6551987E-05		
	$\sigma_{sg \rightarrow g'} \quad g'=g, 20$			
	5.2581262E-03	1.0821348E-02	1.1402715E-02	1.3309040E-02
	8.4035266E-03	1.1167203E-02	5.9983828E-03	3.5772941E-03
	4.1370704E-03	8.4730454E-02	1.4096111E-02	0.0000000E+00
	0.0000000E+00	0.0000000E+00	0.0000000E+00	0.0000000E+00
Group 6	σ_{t6}	σ_{a6}		
	1.4208996E-01	1.2382923E-04		
	$\sigma_{sg \rightarrow g'} \quad g'=g, 20$			
	8.1866561E-03	1.5948793E-02	1.7511148E-02	1.0540984E-02
	1.3598319E-02	7.1890415E-03	4.2668656E-03	4.9245730E-03
	7.1969517E-02	1.7248239E-02	0.0000000E+00	0.0000000E+00
	0.0000000E+00	0.0000000E+00	0.0000000E+00	
Group 7	σ_{t7}	σ_{a7}		
	1.5285659E-01	1.7249379E-04		
	$\sigma_{sg \rightarrow g'} \quad g'=g, 20$			
	1.3402980E-02	2.6396859E-02	1.4675783E-02	1.7907035E-02
	9.1604628E-03	5.3775245E-03	6.1724600E-03	5.7807356E-02
	2.2476153E-02	0.0000000E+00	0.0000000E+00	0.0000000E+00
	0.0000000E+00	0.0000000E+00		
Group 8	σ_{t8}	σ_{a8}		
	1.7902899E-01	3.0938667E-04		
	$\sigma_{sg \rightarrow g'} \quad g'=g, 20$			
	1.9868108E-02	2.8838146E-02	3.0718928E-02	1.4247693E-02
	8.0482531E-03	9.0390667E-03	4.2465165E-02	3.4951247E-02
	0.0000000E+00	0.0000000E+00	0.0000000E+00	0.0000000E+00
	0.0000000E+00			
Group 9	σ_{t9}	σ_{a9}		
	2.0611700E-01	5.0584361E-04		
	$\sigma_{sg \rightarrow g'} \quad g'=g, 20$			
	2.4376355E-02	5.1891696E-02	2.1513708E-02	1.1516063E-02
	1.2488812E-02	3.7899755E-02	4.9281884E-02	0.0000000E+00
	0.0000000E+00	0.0000000E+00	0.0000000E+00	0.0000000E+00

Table A.1:Continued

Group 10	σ_{t10}	σ_{a10}		
	2.4530230E-01	9.5612730E-04		
	$\sigma_{sg \rightarrow g'} \quad g'=g,20$			
	4.3373935E-02	4.1086107E-02	2.0046156E-02	2.0225944E-02
	4.5919865E-02	7.4082389E-02	0.0000000E+00	0.0000000E+00
	0.0000000E+00	0.0000000E+00		
Group 11	σ_{t11}	σ_{a11}		
	2.8729516E-01	1.7829406E-03		
	$\sigma_{sg \rightarrow g'} \quad g'=g,20$			
	3.6689885E-02	3.7547190E-02	3.5407890E-02	6.8590090E-02
	1.0526291E-01	2.0164663E-03	0.0000000E+00	0.0000000E+00
	0.0000000E+00			
Group 12	σ_{t12}	σ_{a12}		
	3.1463978E-01	2.6248128E-03		
	$\sigma_{sg \rightarrow g'} \quad g'=g,20$			
	2.8837714E-02	5.3320464E-02	9.4649322E-02	1.2408095E-01
	1.1125814E-02	0.0000000E+00	0.0000000E+00	0.0000000E+00
	0.0000000E+00			
Group 13	σ_{t13}	σ_{a13}		
	3.3558810E-01	3.6883431E-03		
	$\sigma_{sg \rightarrow g'} \quad g'=g,20$			
	3.7664603E-02	1.2955016E-01	1.4214627E-01	2.2538897E-02
	0.0000000E+00	0.0000000E+00	0.0000000E+00	0.0000000E+00
Group 14	σ_{t14}	σ_{a14}		
	3.8497263E-01	7.7467887E-03		
	$\sigma_{sg \rightarrow g'} \quad g'=g,20$			
	1.0680378E-01	2.1192509E-01	5.8493722E-02	0.0000000E+00
	0.0000000E+00	0.0000000E+00	0.0000000E+00	
Group 15	σ_{t15}	σ_{a15}		
	5.2359432E-01	4.2819150E-02		
	$\sigma_{sg \rightarrow g'} \quad g'=g,20$			
	2.3935764E-01	2.4142663E-01	0.0000000E+00	0.0000000E+00
	0.0000000E+00	0.0000000E+00		

Table A.1: Continued

Group 16	σ_{t16}	σ_{a16}		
	9.8399532E-01	3.4020263E-01		
	$\sigma_{sg \rightarrow g'} \quad g'=g, 20$			
	4.7075158E-01	1.7304881E-01	0.0000000E+00	0.0000000E+00
	0.0000000E+00			
Group 17	σ_{t17}	σ_{a17}		
	2.5197797E+00	1.6785032E+00		
	$\sigma_{sg \rightarrow g'} \quad g'=g, 20$			
	7.4346620E-01	9.7807549E-02	0.0000000E+00	0.0000000E+00
Group 18	σ_{t18}	σ_{a18}		
	7.6898208E+00	6.5476918E+00		
	$\sigma_{sg \rightarrow g'} \quad g'=g, 20$			
	1.1393229E+00	2.6754218E-03	0.0000000E+00	
Group 19	σ_{t19}	σ_{a19}		
	5.4149189E+01	5.1901657E+01		
	$\sigma_{sg \rightarrow g'} \quad g'=g, 20$			
	2.2113309E+00	3.3278834E-02		
Group 20	σ_{t20}	σ_{a20}		
	2.2216533E+02	2.1841698E+02		
	$\sigma_{sg \rightarrow g'} \quad g'=g, 20$			
	3.7436314E+00			

Table A.2: 20 group cross sections of the water material

Group 1	σ_{t1}	σ_{a1}		
	2.1497976E-02	1.2740952E-07		
	$\sigma_{sg \rightarrow g'} \quad g'=g, 20$			
	5.9476047E-04	1.4748238E-03	7.6532090E-04	8.0540759E-04
	8.7268185E-04	9.8562730E-04	1.1844708E-03	1.5773884E-03
	1.0860143E-03	1.5122450E-03	8.3038409E-04	4.9785373E-04
	5.7651068E-04	1.2283050E-02	1.8271270E-03	0.0000000E+00
	0.0000000E+00	0.0000000E+00	0.0000000E+00	0.0000000E+00
Group 2	σ_{t2}	σ_{a2}		
	2.3159359E-02	1.5823230E-07		
	$\sigma_{sg \rightarrow g'} \quad g'=g, 20$			
	9.5149252E-04	1.0840170E-03	1.1107037E-03	1.1696679E-03
	1.2828005E-03	1.4980233E-03	1.9441004E-03	1.3180909E-03
	1.8215023E-03	9.9704345E-04	5.9745251E-04	6.9190765E-04
	1.1081919E-02	2.2308729E-03	0.0000000E+00	0.0000000E+00
	0.0000000E+00	0.0000000E+00	0.0000000E+00	
Group 3	σ_{t3}	σ_{a3}		
	2.4749333E-02	1.8934900E-07		
	$\sigma_{sg \rightarrow g'} \quad g'=g, 20$			
	8.7423826E-04	1.4812433E-03	1.5210294E-03	1.6229392E-03
	1.8420032E-03	2.3265504E-03	1.5509223E-03	2.1246006E-03
	1.1583854E-03	6.9355103E-04	8.0313638E-04	1.0099825E-02
	2.6311115E-03	0.0000000E+00	0.0000000E+00	0.0000000E+00
	0.0000000E+00	0.0000000E+00		
Group 4	σ_{t4}	σ_{a4}		
	2.6929952E-02	2.3450758E-07		
	$\sigma_{sg \rightarrow g'} \quad g'=g, 20$			
	6.7615625E-04	2.1322225E-03	2.1948542E-03	2.3940050E-03
	2.9031211E-03	1.8837666E-03	2.5428154E-03	1.3767413E-03
	8.2286913E-04	9.5238758E-04	9.1889407E-03	3.1867004E-03
	0.0000000E+00	0.0000000E+00	0.0000000E+00	0.0000000E+00
	0.0000000E+00			

Table A.2: Continued

Group 5	σ_{t5}	σ_{a5}		
	2.8915983E-02	2.7659996E-07		
	$\sigma_{sg \rightarrow g'} \quad g'=g,20$			
	1.3691930E-03	2.8462077E-03	2.9991062E-03	3.5005203E-03
	2.2102850E-03	2.9371090E-03	1.5776557E-03	9.4088464E-04
	1.0881119E-03	8.5748481E-03	3.7075668E-03	0.0000000E+00
	0.0000000E+00	0.0000000E+00	0.0000000E+00	0.0000000E+00
Group 6	σ_{t6}	σ_{a6}		
	3.1814769E-02	3.5098131E-07		
	$\sigma_{sg \rightarrow g'} \quad g'=g,20$			
	2.1329573E-03	4.1950396E-03	4.6059266E-03	2.7725741E-03
	3.5767057E-03	1.8909342E-03	1.1223134E-03	1.2952586E-03
	7.9169357E-03	4.5366553E-03	0.0000000E+00	0.0000000E+00
	0.0000000E+00	0.0000000E+00	0.0000000E+00	
Group 7	σ_{t7}	σ_{a7}		
	3.6223304E-02	4.8144682E-07		
	$\sigma_{sg \rightarrow g'} \quad g'=g,20$			
	3.4923707E-03	6.9438596E-03	3.8604722E-03	4.7103353E-03
	2.4096763E-03	1.4145101E-03	1.6237075E-03	7.3927562E-03
	5.9124678E-03	0.0000000E+00	0.0000000E+00	0.0000000E+00
	0.0000000E+00	0.0000000E+00		
Group 8	σ_{t8}	σ_{a8}		
	4.5136757E-02	8.3980910E-07		
	$\sigma_{sg \rightarrow g'} \quad g'=g,20$			
	5.1532192E-03	7.5876783E-03	8.0821319E-03	3.7485154E-03
	2.1175197E-03	2.3781869E-03	7.5481995E-03	9.1953538E-03
	0.0000000E+00	0.0000000E+00	0.0000000E+00	0.0000000E+00
	0.0000000E+00			
Group 9	σ_{t9}	σ_{a9}		
	5.3327106E-02	1.3441349E-06		
	$\sigma_{sg \rightarrow g'} \quad g'=g,20$			
	6.2921592E-03	1.3653586E-02	5.6601642E-03	3.0297739E-03
	3.2857116E-03	8.6727105E-03	1.2965478E-02	0.0000000E+00
	0.0000000E+00	0.0000000E+00	0.0000000E+00	0.0000000E+00

Table A.2: Continued

Group 10	σ_{t10}	σ_{a10}		
	6.3996404E-02	2.4803778E-06		
	$\sigma_{sg \rightarrow g'} \quad g'=g, 20$			
	1.1165620E-02	1.0818527E-02	5.2767992E-03	5.3240936E-03
	1.1933018E-02	1.9500056E-02	0.0000000E+00	0.0000000E+00
	0.0000000E+00	0.0000000E+00	0.0000000E+00	
Group 11	σ_{t11}	σ_{a11}		
	7.4697092E-02	4.7312783E-06		
	$\sigma_{sg \rightarrow g'} \quad g'=g, 20$			
	9.2196688E-03	9.8888045E-03	9.3151927E-03	1.8045219E-02
	2.7694944E-02	5.2965718E-04	0.0000000E+00	0.0000000E+00
	0.0000000E+00	0.0000000E+00		
Group 12	σ_{t12}	σ_{a12}		
	8.1347033E-02	6.9748330E-06		
	$\sigma_{sg \rightarrow g'} \quad g'=g, 20$			
	6.9715818E-03	1.4024726E-02	2.4848463E-02	3.2575086E-02
	2.9205226E-03	0.0000000E+00	0.0000000E+00	0.0000000E+00
	0.0000000E+00			
Group 13	σ_{t13}	σ_{a13}		
	8.6584151E-02	9.8202809E-06		
	$\sigma_{sg \rightarrow g'} \quad g'=g, 20$			
	9.0942858E-03	3.4136470E-02	3.7409335E-02	5.9335767E-03
	0.0000000E+00	0.0000000E+00	0.0000000E+00	0.0000000E+00
Group 14	σ_{t14}	σ_{a14}		
	9.7972885E-02	2.1053767E-05		
	$\sigma_{sg \rightarrow g'} \quad g'=g, 20$			
	2.6762819E-02	5.5795368E-02	1.5393058E-02	0.0000000E+00
	0.0000000E+00	0.0000000E+00	0.0000000E+00	
Group 15	σ_{t15}	σ_{a15}		
	1.2221460E-01	1.2488382E-04		
	$\sigma_{sg \rightarrow g'} \quad g'=g, 20$			
	5.8539510E-02	6.3551515E-02	0.0000000E+00	0.0000000E+00
	0.0000000E+00	0.0000000E+00		

Table A.2: Continued

Group 16	σ_{t16}	σ_{a16}		
	1.5419310E-01	1.1179080E-03		
	$\sigma_{sg \rightarrow g'} \quad g'=g, 20$			
	1.0692208E-01	4.6151448E-02	0.0000000E+00	0.0000000E+00
	0.0000000E+00			
Group 17	σ_{t17}	σ_{a17}		
	1.8344615E-01	6.1398405E-03		
	$\sigma_{sg \rightarrow g'} \quad g'=g, 20$			
	1.5055718E-01	2.6752196E-02	0.0000000E+00	0.0000000E+00
Group 18	σ_{t18}	σ_{a18}		
	2.2449476E-01	2.6944624E-02		
	$\sigma_{sg \rightarrow g'} \quad g'=g, 20$			
	1.9677544E-01	7.7425875E-04	0.0000000E+00	
Group 19	σ_{t19}	σ_{a19}		
	5.0921637E-01	2.6562995E-01		
	$\sigma_{sg \rightarrow g'} \quad g'=g, 20$			
	2.3337848E-01	1.0215724E-02		
Group 20	σ_{t20}	σ_{a20}		
	1.6839091E+00	1.3833390E+00		
	$\sigma_{sg \rightarrow g'} \quad g'=g, 20$			
	2.9902685E-01			

Table A.3: 20 group cross sections of the steel material

Group 1	σ_{t1}	σ_{a1}		
	2.2685638E-01	8.3154257E-05		
	$\sigma_{sg \rightarrow g'} \quad g'=g, 20$			
	3.8248671E-03	9.3767093E-03	4.8656436E-03	5.1205475E-03
	5.5482467E-03	6.2663085E-03	7.5306157E-03	1.0028674E-02
	6.9046305E-03	9.6144555E-03	5.2793720E-03	3.1653030E-03
	3.6653071E-03	2.5820467E-01	1.1616922E-02	0.0000000E+00
	0.0000000E+00	0.0000000E+00	0.0000000E+00	0.0000000E+00
Group 2	σ_{t2}	σ_{a2}		
	2.2586782E-01	1.0398776E-04		
	$\sigma_{sg \rightarrow g'} \quad g'=g, 20$			
	6.1164703E-03	6.8911500E-03	7.0610861E-03	7.4358433E-03
	8.1551298E-03	9.5229512E-03	1.2358759E-02	8.3791520E-03
	1.1579340E-02	6.3382857E-03	3.7981512E-03	4.3985643E-03
	2.2739559E-01	1.4182303E-02	0.0000000E+00	0.0000000E+00
	0.0000000E+00	0.0000000E+00	0.0000000E+00	
Group 3	σ_{t3}	σ_{a3}		
	2.2594951E-01	1.2517256E-04		
	$\sigma_{sg \rightarrow g'} \quad g'=g, 20$			
	5.6118914E-03	9.4183758E-03	9.6716462E-03	1.0319527E-02
	1.1712512E-02	1.4793418E-02	9.8620066E-03	1.3509095E-02
	7.3656631E-03	4.4100839E-03	5.1067397E-03	2.0103100E-01
	1.6729709E-02	0.0000000E+00	0.0000000E+00	0.0000000E+00
	0.0000000E+00	0.0000000E+00		
Group 4	σ_{t4}	σ_{a4}		
	2.2953615E-01	1.5630844E-04		
	$\sigma_{sg \rightarrow g'} \quad g'=g, 20$			
	4.3759332E-03	1.3556480E-02	1.3955994E-02	1.5222344E-02
	1.8459298E-02	1.1978037E-02	1.6168429E-02	8.7541547E-03
	5.2320678E-03	6.0556852E-03	1.7456837E-01	2.0262416E-02
	0.0000000E+00	0.0000000E+00	0.0000000E+00	0.0000000E+00
	0.0000000E+00			

Table A.3: Continued

Group 5	σ_{t5}	σ_{a5}		
	2.3432375E-01	1.8564690E-04		
	$\sigma_{sg \rightarrow g'} \quad g'=g, 20$			
	8.8064428E-03	1.8096549E-02	1.9068779E-02	2.2256711E-02
	1.4053217E-02	1.8674985E-02	1.0031126E-02	5.9823189E-03
	6.9184373E-03	1.5489502E-01	2.3572899E-02	0.0000000E+00
	0.0000000E+00	0.0000000E+00	0.0000000E+00	0.0000000E+00
Group 6	σ_{t6}	σ_{a6}		
	2.4296764E-01	2.3809829E-04		
	$\sigma_{sg \rightarrow g'} \quad g'=g, 20$			
	1.3710076E-02	2.6670963E-02	2.9283730E-02	1.7627591E-02
	2.2740379E-02	1.2022154E-02	7.1354327E-03	8.2353596E-03
	1.3095693E-01	2.8844183E-02	0.0000000E+00	0.0000000E+00
	0.0000000E+00	0.0000000E+00	0.0000000E+00	
Group 7	σ_{t7}	σ_{a7}		
	2.5945467E-01	3.3167747E-04		
	$\sigma_{sg \rightarrow g'} \quad g'=g, 20$			
	2.2445440E-02	4.4142511E-02	2.4541862E-02	2.9945500E-02
	1.5318749E-02	8.9927185E-03	1.0321978E-02	1.0419201E-01
	3.7586082E-02	0.0000000E+00	0.0000000E+00	0.0000000E+00
	0.0000000E+00	0.0000000E+00		
Group 8	σ_{t8}	σ_{a8}		
	3.0126873E-01	5.9492304E-04		
	$\sigma_{sg \rightarrow g'} \quad g'=g, 20$			
	3.3295199E-02	4.8223425E-02	5.1368874E-02	2.3825351E-02
	1.3458440E-02	1.5115317E-02	7.4500598E-02	5.8446545E-02
	0.0000000E+00	0.0000000E+00	0.0000000E+00	0.0000000E+00
	0.0000000E+00			
Group 9	σ_{t9}	σ_{a9}		
	3.4554198E-01	9.7272015E-04		
	$\sigma_{sg \rightarrow g'} \quad g'=g, 20$			
	4.0879410E-02	8.6773574E-02	3.5975777E-02	1.9257506E-02
	2.0884154E-02	6.4627148E-02	8.2410790E-02	0.0000000E+00
	0.0000000E+00	0.0000000E+00	0.0000000E+00	0.0000000E+00

Table A.3: Continued

Group 10	σ_{t10}	σ_{a10}		
	4.1072226E-01	1.8386585E-03		
	$\sigma_{sg \rightarrow g'} \quad g'=g, 20$			
	7.2767735E-02	6.8696626E-02	3.3519059E-02	3.3819713E-02
	7.6931171E-02	1.2387353E-01	0.0000000E+00	0.0000000E+00
	0.0000000E+00	0.0000000E+00	0.0000000E+00	
Group 11	σ_{t11}	σ_{a11}		
	4.8127833E-01	3.4285404E-03		
	$\sigma_{sg \rightarrow g'} \quad g'=g, 20$			
	6.1770920E-02	6.2777460E-02	5.9210442E-02	1.1469863E-01
	1.7602265E-01	3.3728210E-03	0.0000000E+00	0.0000000E+00
	0.0000000E+00	0.0000000E+00		
Group 12	σ_{t12}	σ_{a12}		
	5.2752870E-01	5.0474256E-03		
	$\sigma_{sg \rightarrow g'} \quad g'=g, 20$			
	4.8815750E-02	8.9167379E-02	1.5832642E-01	2.0755884E-01
	1.8611260E-02	0.0000000E+00	0.0000000E+00	0.0000000E+00
	0.0000000E+00			
Group 13	σ_{t13}	σ_{a13}		
	5.6282312E-01	7.0925397E-03		
	$\sigma_{sg \rightarrow g'} \quad g'=g, 20$			
	6.3768484E-02	2.1658669E-01	2.3768981E-01	3.7686575E-02
	0.0000000E+00	0.0000000E+00	0.0000000E+00	0.0000000E+00
Group 14	σ_{t14}	σ_{a14}		
	6.4694959E-01	1.4896360E-02		
	$\sigma_{sg \rightarrow g'} \quad g'=g, 20$			
	1.7988706E-01	3.5434926E-01	9.7811230E-02	0.0000000E+00
	0.0000000E+00	0.0000000E+00	0.0000000E+00	
Group 15	σ_{t15}	σ_{a15}		
	8.9052993E-01	8.2329087E-02		
	$\sigma_{sg \rightarrow g'} \quad g'=g, 20$			
	4.0452936E-01	4.0368786E-01	0.0000000E+00	0.0000000E+00
	0.0000000E+00	0.0000000E+00		

Table A.3: Continued

Group 16	σ_{t16}	σ_{a16}		
	1.7462558E+00	6.5399212E-01		
	$\sigma_{sg \rightarrow g'} \quad g'=g, 20$			
	8.0350310E-01	2.8877681E-01	0.0000000E+00	0.0000000E+00
	0.0000000E+00			
Group 17	σ_{t17}	σ_{a17}		
	4.6752820E+00	3.2260878E+00		
	$\sigma_{sg \rightarrow g'} \quad g'=g, 20$			
	1.2866116E+00	1.6257483E-01	0.0000000E+00	0.0000000E+00
Group 18	σ_{t18}	σ_{a18}		
	1.4590802E+01	1.2581800E+01		
	$\sigma_{sg \rightarrow g'} \quad g'=g, 20$			
	2.0043461E+00	4.4061625E-03		
Group 19	σ_{t19}	σ_{a19}		
	1.0377533E+02	9.9682167E+01	0.0000000E+00	
	$\sigma_{sg \rightarrow g'} \quad g'=g, 20$			
	4.0332837E+00	5.4243896E-02		
Group 20	σ_{t20}	σ_{a20}		
	4.2616354E+02	4.1923535E+02	0.0000000E+00	
	$\sigma_{sg \rightarrow g'} \quad g'=g, 20$			
	6.9205618E+00			

REFERENCES

1. E. E. Lewis and W. F. Miller, *Computational methods of neutron transport*, American Nuclear Society, 1993.
2. I. Babuska and R. W. C., *A posteriori error estimates for the finite element method*, International Journal for Numerical Methods in Engineering **12** (1978), 1597-1615.
3. I. Babuska and W. C. Rheinboldt, *Error estimates for the adaptive finite element computations*, SIAM Journal on Numerical Analysis **18** (1978), 736-754.
4. ---, *Analysis of optimal finite element meshes in r^l* , Mathematics of Computation **33** (1979), 435-463.
5. ---, *A posteriori error analysis of finite element solutions for one dimensional problems*, SIAM Journal on Numerical Analysis **18** (1981), 565-589.
6. L. Demkowicz, J. T. Oden and T. Strouboulis, *Adaptive finite elements for flow problems with moving boundaries. Part 1: Variational principles and a posteriori error estimates*, Computer Methods in Applied Mechanics and Engineering **46** (1984), 217-251.
7. R. E. Bank and A. Weiser, *Some a posteriori error estimators for elliptic partial differential equations*, Mathematics of Computation **44** (1985), 283-301.
8. ---, *Analysis of a local a posteriori error estimate for elliptic equations*, Wiley, New York, 1986.
9. O. C. Zienkiewicz and J. Z. Zhu, *The superconvergent patch recovery and a posteriori error estimates. Part 1: The recovery technique*, International Journal for Numerical Methods in Engineering **33** (1992), 1331-1364.
10. ---, *The superconvergent patch recovery and a posteriori error estimates. Part 2: Error estimates and adaptivity*, International Journal for Numerical Methods in Engineering **33** (1992), 1365-1382.
11. M. Ainsworth and J. T. Oden, *A posteriori error estimation in finite element analysis*, Computer Methods in Applied Mechanics and Engineering **142** (1997), 3771-3796.
12. S. Prudhomme and J. T. Oden, *On goal-oriented error estimation for elliptic problems: Application to the control of pointwise errors*, Computer Methods in Applied Mechanics and Engineering **176** (1999), 313-331.

13. E. Stein, *Error-controlled finite elements in solid mechanics*, John Wiley and Sons, 2002.
14. J. T. Oden and S. Prudhomme, *New approaches to error estimation and adaptivity for the stokes and oseen equations*, International Journal for Numerical Methods in Fluids **190** (1999), 3-15.
15. P. Solin and L. Demkowicz, *Goal-oriented hp-adaptivity for elliptic problems*, Computer Methods in Applied Mechanics and Engineering **193** (2004), no. 4-6, 449-468.
16. M. B. Giles, N. A. Pierce and E. Suli, *Progress in ajoint error correction for integral functionals*, Computational Visual Science **6** (2004), 113-121.
17. N. A. Pierce and M. B. Giles, *Ajoint and defect error bounding and correction for functional estimates*, Journal of Computational Physics **200** (2004), 769-794.
18. W. M. Stacey, *Variational methods in nuclear reactor physics*, Academic Press, New York, 1974.
19. V. S. Vladimirov, "Mathematical problems in the one-velocity theory of particle transport," A. E. o. C. Ltd. (Editor), 1963.
20. S. Kaplan and J. A. Davis, *Canonical and incolutory transformations of the variational problems of transport theory*, Nuclear Science and Engineering **28** (1967), 166-176.
21. J. A. Davis, *Transport error bounds via p_n approximations*, Nuclear Science and Engineering **31** (1968), 127-146.
22. A. J. Buslik, *Extremum variational principles for the monoenergetic neutron transport equation with arbitrary adjoint source*, Nuclear Science and Engineering **35** (1969), 303-318.
23. R. T. Ackroyd and B. A. Splawski, *A finite element method for neutron transprot vi. Upper and lower bounds for local characteristics of solutions*, Annals of Nuclear Energy **9** (1982), 315-330.
24. H. Zhang and E. E. Lewis, *Spatial adaptivity applied to the variational nodal p_n equations*, Nuclear Science and Engineering **142** (2001), 57-63.
25. ---, *An adaptive approach to variational nodal diffusion problems*, Nuclear Science and Engineering **137** (2001), 14-22.
26. J. C. Ragusa, *3-d adaptive solution for the multigroup diffusion equation on irregular structured grids using a non-conforming finite element method formulation*, the PHSOR 2004 International Conference, 2004, p.^pp.

27. Y. Wang and J. C. Ragusa, *Adaptive hp-mesh refinement applied to 1-d, one-group diffusion problems*, Transactions of the American Nuclear Society, Winter 2005 ANS meeting, 2005, p.^pp. 585-587.
28. C. Fuhrer and R. Rannacher, *Error analysis for the finite element approximation of a radiative transfer model*, RAIRO Mathematical Modeling and Numerical Analysis **30** (1996), 743-762.
29. J. Warsa and A. Prinja, *P-adaptive numerical methods for particle transport*, Transport Theory and Statistical Physics **28** (1999), 229-270.
30. C. Ausourd, *Styx: A multidimensional amr s_n scheme*, Nuclear Science and Engineering **143** (2003), 281-290.
31. R. T. Ackroyd and W. E. Wilson, *Discontinuous finite elements for neutron transport analysis*, Progress in Nuclear Energy **18** (1986), 39-44.
32. ---, *Composite finite element solutions for neutron transport*, Annals of Nuclear Energy **15** (1988), 397-419.
33. J. C. Stone and M. L. Adams, *Adaptive discrete-ordinates algorithms and strategies*, Mathematics and Computation, Supercomputing, Reactor Physics and Nuclear and Biological Applications, 2005, p.^pp.
34. H. Park and C. R. E. de Oliveira, *Adaptive angular resolution for the finite element-spherical harmonics method*, Transaction of American Nuclear Society: Winter 2005 ANS Meeting, 2005, p.^pp. 517-519.
35. C. R. E. de Oliveira and A. J. H. Goddard, *Event - a multidimensional finite element-spherical harmonics radiation transport code*, the OECD International Seminar on 3D Deterministic Radiation Transport Codes, 1996, p.^pp.
36. C. R. E. de Oliveira, C. C. Pain and M. Eaton, *Hierarchical angular preconditioning for the finite element-spherical harmonics radiation transport method*, the PHYSOR 2000 - ANS International Topical Meeting on Advances in Reactor Physics and Mathematics and Computation into the Next Millennium, 2000, p.^pp.
37. R. T. Ackroyd, *Finite element methods for particle transport*, John Wiley and Sons, 1997.
38. C. R. E. de Oliveira, M. Eaton, A. P. Umpleby and C. C. Pain, *Finite element-spherical harmonics solutions of the 3d kobayashi benchmarks with ray-tracing void treatment*, Progress in Nuclear Energy **39** (2001), no. 2, 243-261.
39. G. C. Pomraning, *A derivation of variational principles for inhomogeneous equations*, Nuclear Science and Engineering **29** (1967), 220.

40. J. Lewins, *Time-dependent variational theory*, Nuclear Science and Engineering **31** (1968), 160.
41. A. Ern and J.-L. Guermond, *Theory and practice of finite elements*, vol. 159, Springer, 2004.
42. C. R. E. de Oliveira, "Finite element techniques for multigroup neutron transport calculations with anisotropic scattering," *Nuclear Engineering*, vol. Doctor of Philosophy, Queen Mary College, University of London, London, 1987.
43. ---, *An arbitrary geometry finite element method for multigroup neutron transport with anisotropic scattering*, Progress in Nuclear Energy **18** (1986), 227.
44. H. A. van der Vorst, *Iterative krylov methods for large linear systems*, Cambridge University Press, Cambridge, 2003.
45. J. N. Reddy, *An introduction to the finite element method*, McGraw-Hill, 1993.
46. P. Clement, *Approximation by finite element functions using local regularization*, RAIRO Analyse numerique. **2** (1975), 77-84.
47. R. E. Bank and R. K. Simith, *A posteriori error estimates based on hierarchical bases*, SIAM Journal on Numerical Analysis **30** (1993), no. 4, 921-935.
48. P. Ladeveze and D. Leguillon, *Error estimate procedure in the finite element method and applications*, SIAM Journal on Numerical Analysis **20** (1983), no. 3, 485-509.
49. G. Palmiotti, E. E. Lewis and C. B. Carrico, "Variant: Variational anisotropic nodal transport for multidimensional cartesian and hexagonal geometry calculation," Argonne National Laboratory, 1995.
50. M. A. Smith, E. E. Lewis and B.-C. Na, *Benchmark on deterministic 2-d mox fuel assembly transport calculations without spatial homogenization*, Progress in Nuclear Energy **45** (2004), no. 2-4, 107-118.
51. S. D. Pautz and C. Drumm, *Manufactured solution verification of the ceptre code*, M&C 2005 On Mathematics and Computation, Supercomputing, Reactor Physics and Nuclear and Biological Applications, 2005, p.^pp. 234.
52. W. Reed, *New difference schemes for the neutron transport equation*, Nuclear Science and Engineering **46** (1971), 31.
53. B. D. Ganapol and D. E. Kornreich, *Mining the multigroup-discrete ordinate algorithm for high quality solutions*, Mathematics and Computation, Supercomputing, Reactor Physics and Nuclear and Biological Applications, 2005, p.^pp.

54. Y. Y. Azmy, *The weighted diamond-difference form of nodal transport methods.*, Nuclear Science and Engineering **98** (1988), 29.
55. W. M. Stacey, *Nuclear reactor physics*, Wiley, New York, 2001.
56. J. E. White and e. al., *Bugle-96: A revised multigroup cross section library for lwr applications based on endf/b-vi release3*, American Nuclear Society Radiation Protection and Shielding Topical Meeting, 1996, p.^pp.

VITA

HyeongKae Park was born in Japan in the city of Chichibu, Saitama in 1978. He graduated from Kumagaya High School, Saitama in March 1997. After high school, he attended University of Oregon, Eugene, Oregon, from January 1998 to June 2001 to obtain B.S. in Chemistry and Physics. Upon graduation, he moved to Baton Rouge, Louisiana. He attended Louisiana State University from August 2001 to August 2003 to obtain M.S. in Health Physics. After graduating from Louisiana State University, he attended Georgia Institute of Technology to pursue his Ph.D. in Nuclear Engineering.